REPORT DOCUMENTATION PAGE

Form Approved
OMB No. 0704-0188

1. AGENCY USE ONLY (Leave blank)	2. REPORT DATE	3. REPORT TYPE AND DATES COVERED
	1 August, 1996	Final Technical, 6/15/93-6/14/96

4. TITLE AND SUBTITLE	5. FUNDING NUMBERS
New Approaches for Modeling Liquid Jet Atomization	F49620-93-1-0363 3484/MAS

6. AUTHOR(S)

Stephen D. Heister

7. PERFORMING ORGANIZATION NAME(S) AND ADDRESS(ES)	8. PERFORMING ORGANIZATION REPORT NUMBER
PURDUE UNIVERSITY 1282 GRISSOM HALL W. LAFAYETTE, IN 47907	

9. SPONSORING/MONITORING AGENCY NAME(S) AND ADDRESS(ES)	10. SPONSORING/MONITORING AGENCY REPORT NUMBER
AFOSR/NA Bolling AFB DC 20332-6448 NA	F49620-93-1-0363

11. SUPPLEMENTARY NOTES

AFOSR-TR-96

0472

12a. DISTRIBUTION/AVAILABILITY STATEMENT

Approved for Public Release; Distribution is unlimited

19961015 042

13. ABSTRACT (Maximum 200 words)

This report summarizes atomization simulations performed to investigate the role of this process in liquid rocket engine combustion instabilities. The research involves the development and application of a series of nonlinear free-surface models based on boundary element methods (BEMs). Models have been developed to study the effects of unsteady injection, transverse acoustic wave interactions (such as those experienced in the F-1 engine), longitudinal acoustic wave interactions, and the dynamics of droplets in the presence of an acoustic wave. Results for each of these four models is presented in this document.

DTIC QUALITY INSPECTED 2

14. SUBJECT TERMS			15. NUMBER OF PAGES
atomization, free surfaces, liquid rocket, engine injectors, combustion instability			95
			16. PRICE CODE

17. SECURITY CLASSIFICATION OF REPORT	18. SECURITY CLASSIFICATION OF THIS PAGE	19. SECURITY CLASSIFICATION OF ABSTRACT	20. LIMITATION OF ABSTRACT
Unclassified	Unclassified	Unclassified	UL

NSN 7540-01-280-5500

Standard Form 298 (Rev. 2-89)
Prescribed by ANSI Std. Z39-18

DISCLAIMER NOTICE
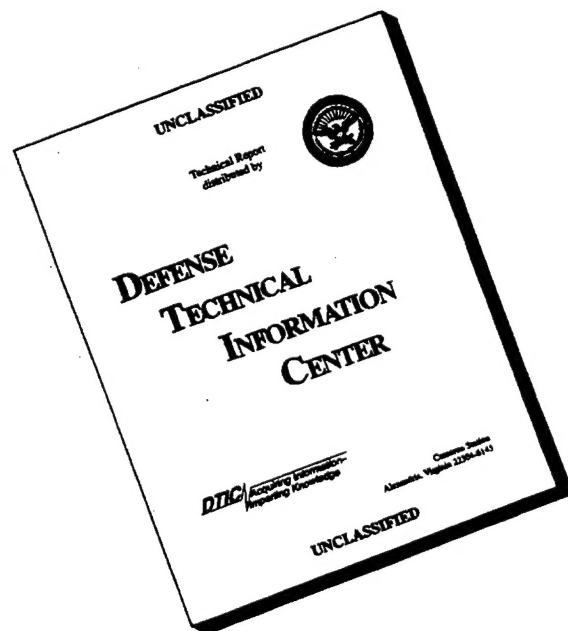
THIS DOCUMENT IS BEST QUALITY AVAILABLE. THE COPY FURNISHED TO DTIC CONTAINED A SIGNIFICANT NUMBER OF PAGES WHICH DO NOT REPRODUCE LEGIBLY.

AFOSR Contract F49620-94-1-0151

MODELING OF LIQUID JET ATOMIZATION PROCESSES

Stephen D. Heister, Associate Professor
School of Aeronautics and Astronautics
Purdue University
1282 Grissom Hall
West Lafayette, IN 47907

1 August 1996

Final Technical Report for Period 1 July 1994 - 30 June 1996

Approved for Public Release,
Distribution is Unlimited

Contents

1 Summary

This research program has focused on enhancing the understanding of jet atomization processes and their contribution to combustion instabilities in liquid rocket engines. During the past two years, progress has been made in understanding the role of the atomization process in tangential-mode instabilities in the F-1 engine. Boundary element simulations developed in this research have been compared with experimental results, showing excellent agreement. Three new models have been developed during the effort. The first model involves a fully-coupled gas/liquid simulation of an injection process under unsteady chamber conditions. The second model involves a zonal approach to a fully viscous simulation, wherein boundary layers are treated via an integral formulation and boundary elements are used at the viscous/inviscid interface. The third model addresses the nonlinear response of a droplet to an imposed acoustic perturbation has been studied. Results from all models are described in this report.

2 Research Objectives

The understanding of the complex combustion phenomena present in liquid rocket engines begins with the fundamental process of fuel and oxidizer jet atomization. Since the atomization process can be greatly effected by acoustic disturbances[1], it appears as a primary focus[2] in studies involving combusiton stability. For this reason, a focused research effort has been conducted to develop models capable of providing *quantitative* information regarding atomization processes (in both steady and unsteady chamber environments).

The objective of this research has been to develop a series of models, incorporating increasingly complex physics, to assess the role of atomization in the combustion instability process. The models have centered on the use of Boundary Element Methods (BEMs) as a means to provide accurate description of these complex, nonlinear processes under arbitrary unsteady conditions. The models have demonstrated a capability to have calculations proceed *beyond atomization events*. While the basic BEM techniques are inviscid, recent development of a zonal model using an integral method for boundary layer modeling, permits a full viscous capability. This model, described in Section 3.6 of this report, is the first primary atomization model to provide accurate, fully nonlinear treatment of atomization processes under full-scale Reynolds numbers consistent with actual engine conditions. While other viscous models exist[3,4], they can only provide simulations for low Reynolds numbers (of the order of a few hundred), while real jets are typically in the $Re \approx 10^5 - 10^6$ range.

With these capabilities, we have sought to address the sizes of droplets produced under various steady and unsteady injection conditions. In addition, the response of droplets to acoustic processes is another objective of this work. The following section details the status of these developments. Section 4 provides a description of professional activities (including publications and student theses) associated with this project.

3 Status of the Research

Seven major tasks have been accomplished during the two year research program. Collaboration with Dr. Steven Collicott (also in the School of Aeronautics and Astronautics) has enabled the generation of high-quality experimental data with which to compare atomization models (See Section 3.1). The effect of unsteady injection processes on the atomization of a liquid jet is addressed in Section 3.2. Section 3.3 provides a description of the role of the atomization process in tangential-mode combustion instabilities observed during the development of the F-1 engine. In Section 3.4, the response of a droplet to an acoustic perturbation is quantified, while Section 3.5 describes the fully-viscous model discussed above. Finally, results from a fully-coupled gas/liquid model are described in Section 3.6 and the fully viscous model highlighted in Section 2 is described in Section 3.7.

3.1 Comparison with Experimental Images of Jet Profiles

Under the direction of Professor's Heister and Collicott, Mike Moses developed an experimental setup capable of providing high-resolution imaging of low-speed liquid jets during the atomization process. The imaging system magnifies and records a shadow image of the water jet. A pair of achromatic lenses of focal length
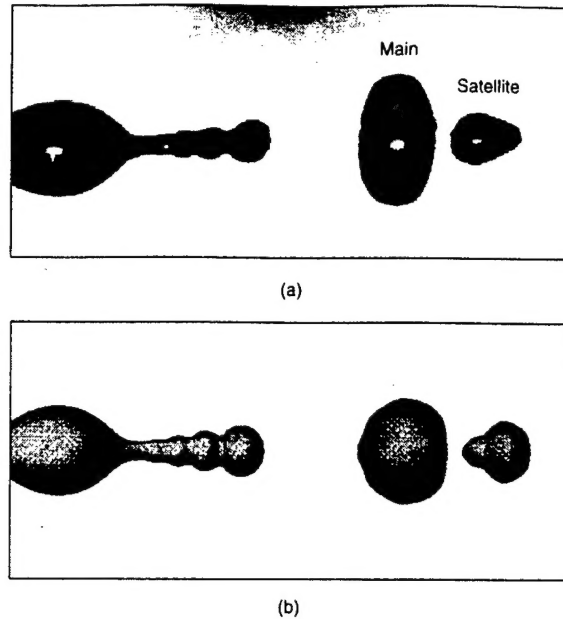
(a)

(b)

Figure 1: Jet Profile Comparison Near the Pinch Location, (a) Experiment of Moses, (b) BEM Result, We=17.6, Bo=0.0109, $k = 0.447$.

20 cm and diameter 4 cm are used to form a 1:1 image of the jet in the intermediate image plane, which is then imaged onto the CCD detector at the desired magnification. A variable-diameter circular iris is located between the achromats and controls the effective F-number of the imaging system. The short-pulsed spark source assures an instantaneous sample of the jet and drop shapes.

The edge detection scheme used in this project is an improvement of the method of Collicott, et al.[5], which was applied to an anamorphic imaging system to measure growth rates of waves on liquid jets. The additional purpose of the improved method is to investigate droplet sizes. Therefore, the edge detection procedure is applied to the image in both directions. Programming effort is required to sort edges in droplets, and to assemble the data from horizontal and vertical scans. The fundamental operation performed in these methods is to convolve the image greyscale data with the theoretical edge-response of the imaging system. In the present work, the combined effects of diffraction and aberrations are approximated by assuming a circular Gaussian impulse response. More details regarding the experimental apparatus can be found in the paper attached in Appendix A.

A simulation using our finite-length jet code[6] was run to assess the accuracy of the BEM in reproducing experimental results. Figure 1 provides a comparison of the calculation with the observation. The agreement between the BEM simulation and the experimental measurements are excellent; "recoil" waves generated as a result of the pinching process are resolved within the calculation, as is the size and relative spacing of main and satellite droplets. This comparison confirms the high-accuracy of the BEM in problems of this nature.

3.2 Effects of Unsteady Injection on Atomization

One of the consequences of unsteadiness in the combustion chamber is the possibility of inducing unsteady massflow through injector orifice passages. To address this issue, our finite-length jet simulation[6] was applied to a range of unsteady flows in which the frequency and amplitude of the unsteady component of injection velocity was varied. The effect of oscillation magnitude on the jet breakup is investigated by six simulations with unsteady velocity component (q') varying between 2 and 7% of the mean. Figure 2 shows jet profiles for three of these disturbance magnitudes. Each pair of profiles shows the jet at times just before a main droplet and a satellite droplet are shed from the calculation. As this figure shows, increasing the size of the

perturbation decreases the breakup length, and changes the shape of the droplets.

At larger disturbance magnitudes, the main droplets take on a "squashed" shape as a result of the high velocity fluid encountering lower velocity fluid which has already exited the nozzle. This phenomena, known as the "Klystron" effect, has been documented qualitatively by numerous researchers[7,8] in the case where forcing perturbations are very large amplitude.

Figure 3 shows the effect of dimensionless frequency (k) on the character of the jet for $q' = 2\%$. Each of the first four pairs of profiles show the jet at times just before a main droplet and just before a satellite droplet are shed from the calculation. Increasing the frequency from $k = 0.5$ to $k = 1.1$ tends to decrease the breakup length even beyond the most unstable wave number, $k_{max} = 0.7$; a trend not predicted by linear theory. In addition, the size of satellite drops tends to decrease with increasing frequency in this range. At a wave number of $k = 1.1$, satellite drops have nearly vanished indicating that a wave number near this value can produce monodisperse atomization.

Quantitative predictions of droplet sizes are shown in Fig. 4. Here, the solid lines are results for infinitesimal disturbances and experimental results are a composite of data from Lafrance[9] and Rutland and Jameson[10]. The finite-amplitude results are for $q' = 2\%$, and they show a tendency to drive conditions toward a monodisperse result by increasing satellite drop size and decreasing main drop size over the entire range of wave numbers investigated. Once again, the peak-sharpening and trough broadening which occur with increased disturbance magnitude provide an explanation for the observed results. At higher disturbance amplitudes, local curvature in the transition region between peaks and troughs can be driven to large enough values to promote nonlinear instability at wavelengths predicted to be stable using linear analysis.

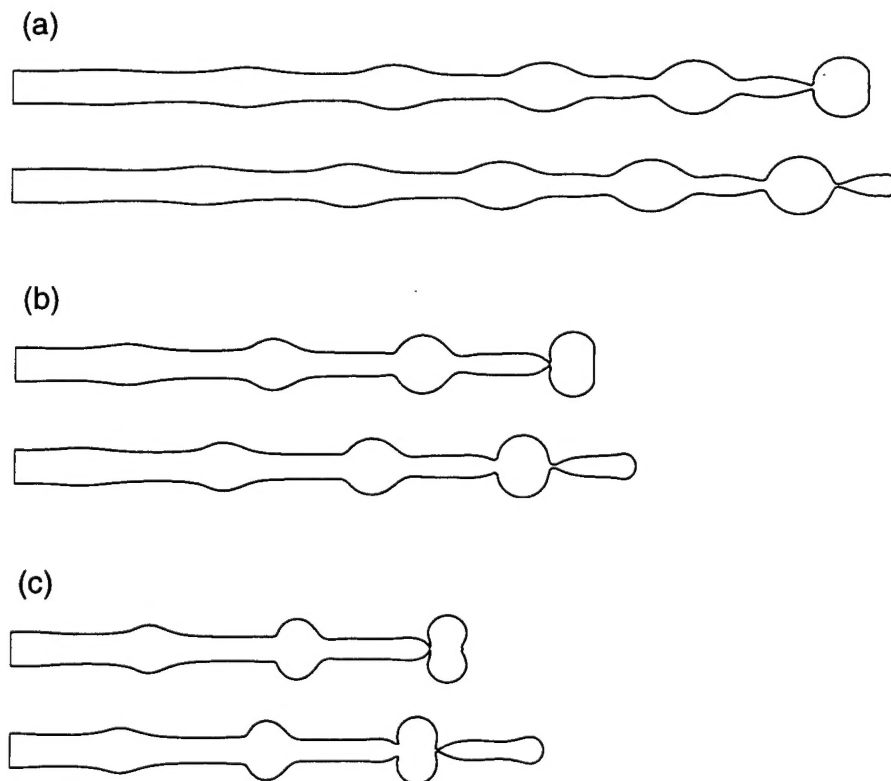A complete description of these simulations is provided in the *Physics of Fluids* article attached in Appendix B.

(a)

(b)

(c)

Figure 2: Effect of Longitudinal Disturbance Amplitude on Behavior of Liquid Jet at $We = 100$, $\omega_g = \omega = 0.7$. (a) $q' = 2\%$, (b) $q' = 4\%$, (c) $q' = 6\%$
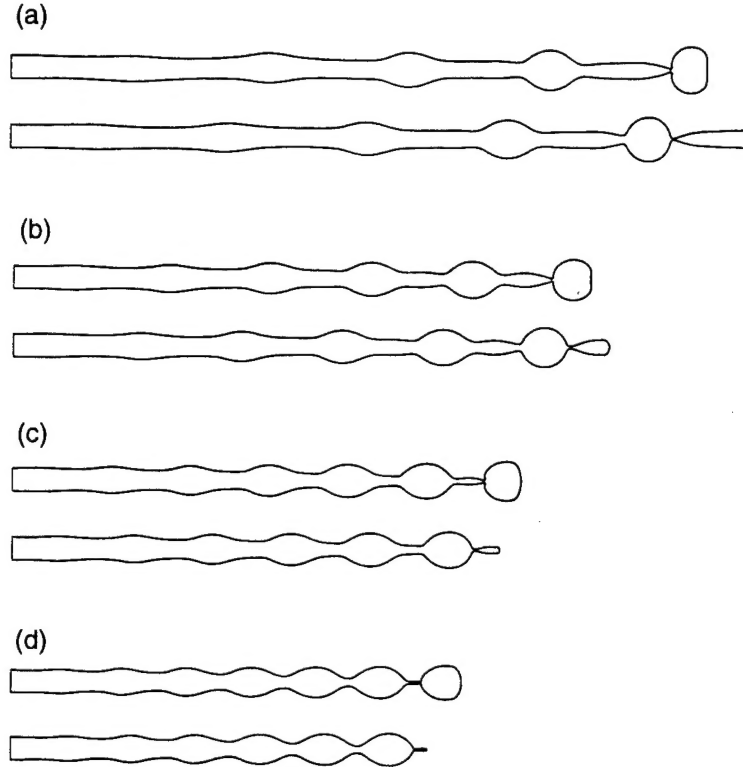
Figure 3: Effect of Longitudinal Disturbance Frequency on Behavior of Liquid Jet at $We = 100$, $q' = 2\%$. (a) $\omega/\omega_g = 0.71$, (b) $\omega/\omega_g = 1.0$, (c) $\omega/\omega_g = 1.29$, (d) $\omega/\omega_g = 1.57$

3.3 Simulation of F-1 Engine Tangential-Mode Instability

Through the recent development of a 2-D simulation of a liquid column responding to an imposed crossflow, we have been able to construct simulations pertinent to tangential-mode acoustic instabilities in liquid rocket engines. As a result, efforts have been focused to analyze both stable and unstable injector designs from the F-1 engine test program[11]. As one might expect, the response of the column grows dramatically when the acoustic frequency (ω_g) is near that of the column natural frequency (ω).

Using the model, a simulation was conducted of a highly-unstable F-1 injector configuration (the Double Row Cluster, DRC), as well as the final, stable configuration demonstrated in Flight Rating Tests (FRT). The DRC design exhibited a 1T instability at 454 Hz which led to chamber pressure oscillations of the order of 400% of the mean. The most prominent difference between these two injectors is the fuel orifice size (3.57 mm radius on FRT vs. 1.4 mm radius on DRC). The combination of the acoustic frequency in the chamber and the natural frequency of the DRC fuel colum leads to conditions very near the resonant frequency. In fact, we calculate that $\omega_g/\omega = 1.7$ for the DRC, while the FRT design has $\omega_g/\omega = 7.0$, a value far from the high response region.

To assess the impact of the fuel orifice design differences between the two injectors, we have completed a simulation for both designs at a fixed Weber number of 0.1. Results of the column shapes at various times are shown in Fig. 5 for both designs. This figure shows that the unstable DRC design undergoes violent oscillations, whereas the stable FRT design is relatively unaffected by the imposed oscillation. Clearly, the large deformations of the DRC design will have substantial effect on the jet impingement region - a critical design feature for this impinging element injector. For this reason, **we believe that the sensitivity of the DRC design to transverse acoustic energy may be a major contributer to the instability of this injector design.**

Further description of this analysis can be found in the *Journal of Propulsion and Power* article attached as Appendix C. In addition, a new manuscript, which will explore this problem in more depth is currently in preparation.
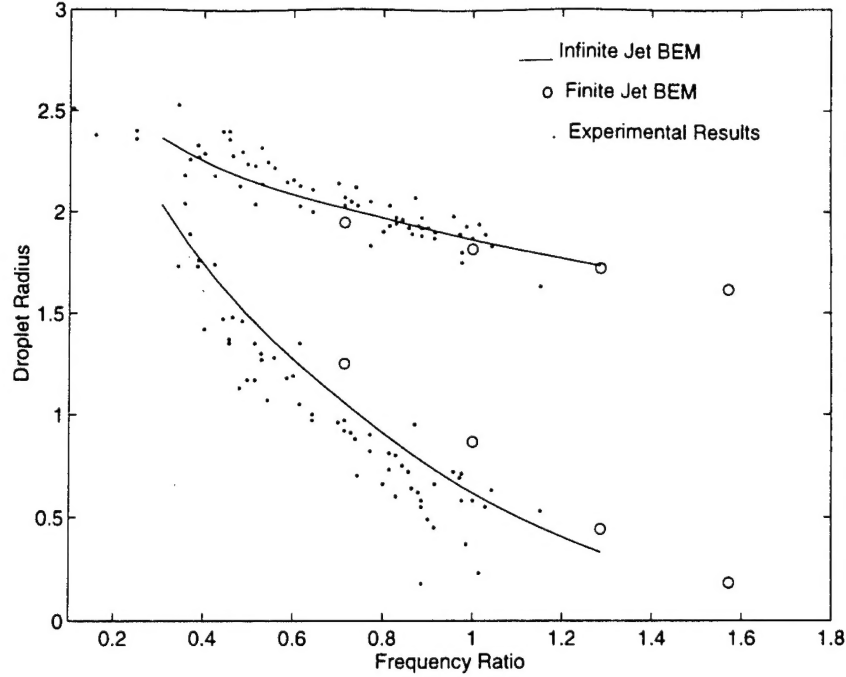
Figure 4: Effect of Longitudinal Disturbance Frequency on Drop Size for Liquid Jet at $We = 100$, $q' = 2\%$. Solid Lines are for $q' \approx 0$.

3.4 Nonlinear Droplet Response to Acoustic Excitation

A model was developed to investigate the deformation (and possible breakup) of a droplet exposed to an acoustic wave. A series of simulations at a constant gas/liquid density ratio of 0.001, and at a Weber number (We) of 0.58. These conditions are roughly equivalent to a 100 micron water droplet excited by a 160 decibel sound wave. Figure 6 shows the nonlinear frequency response of the droplet under these conditions. Here, the overall level of response is inferred from the aspect ratio (in either prolate or oblate form) of the droplet under maximum deformation conditons. The droplet response is much more complex than that of the liquid column in that 4th-mode coupling is present in many cases. Sharp peaks are realized at several higher-order harmonics. The region $0.9 < \omega_g/\omega < 1$ is characterized by actual fragmentations of the droplet.

Figure 7 highlights the droplet breakup modes identified using this model. At lower We values, small "nipples" are pinched from the main body of fluid. As We grows, dumbell-shaped structures are encountered, followed by "doughnut-shaped" structures. At the very high We values, the droplet flattens to a disk, and small rings are shed from the periphery. This behavior has been noted by several experimentalists by exposing droplets to shock waves, thereby causing a large dynamic pressure about the drop. Breakup times decrease dramatically as We is increased.

A complete description of this model, which includes many more results, is provided in Appendix D. This manuscript is currently in review in *International Journal for Multiphase Flows*.

3.5 Coupled Gas/Liquid BEM Simulations

During the past year, we have developed a fully-coupled, nonlinear simulation of a liquid jet issuing into a quiescent gas. This model has been developed to assess unsteady chamber effects on the atomization process. Researchers have speculated that the unsteady chamber conditions existing during combustion instabilities could impact the atomization process, thereby amplifying (or damping) the instability. While several calculations have been made using our model, a single highlight will be discussed here. Figure 8 illustrates the influence of chamber gas density on the behavior of the jet at fixed inflow (i.e. Weber number) conditions. The gas density effect is measured through the input gas/liquid density ratio, ϵ. Mushroom-capped structures appear at high ϵ values due to the substantial momentum required to displace the "heavy"

6

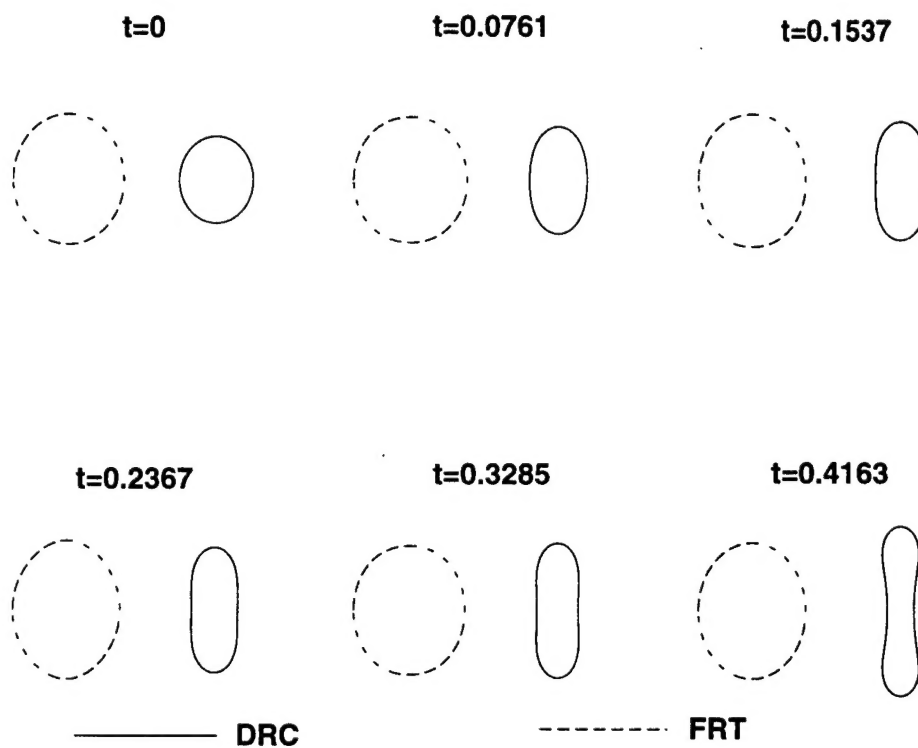Figure 5: Simulation of Fuel-Jet Response in the Unstable Double-Row Cluster (DRC) and Stable Flight Rating Tests (FRT) F-1 Engine Injectors (times are measured in seconds from start of disturbance)

We = 1.25   **We = 2.25**   **We = 2.50**
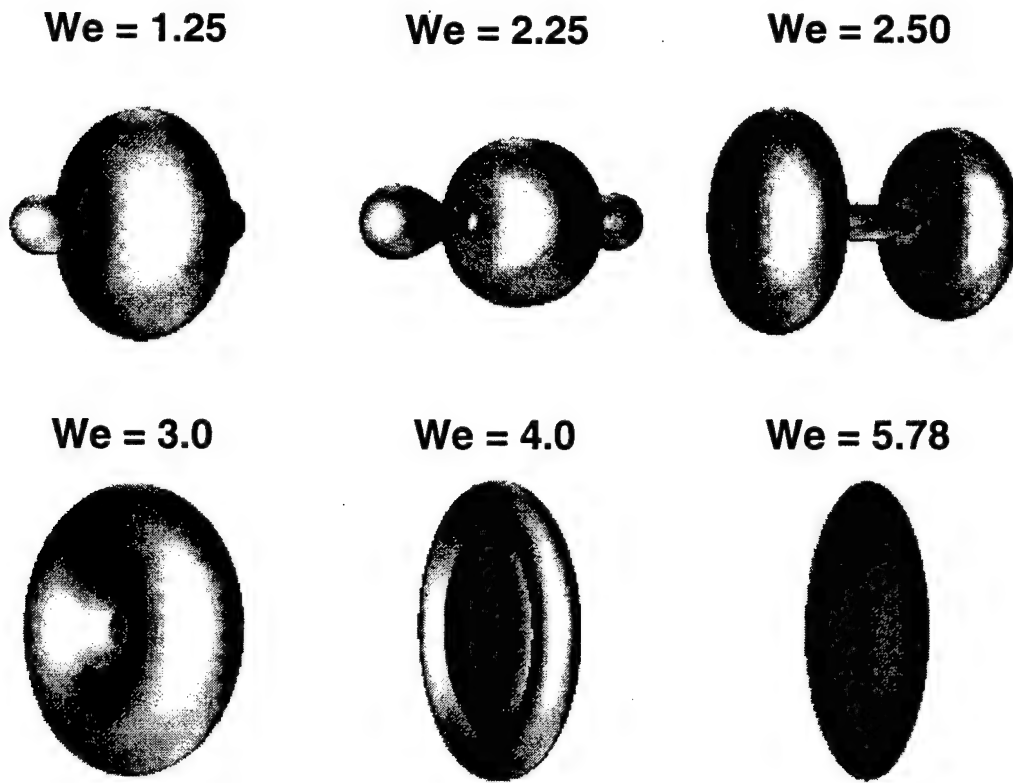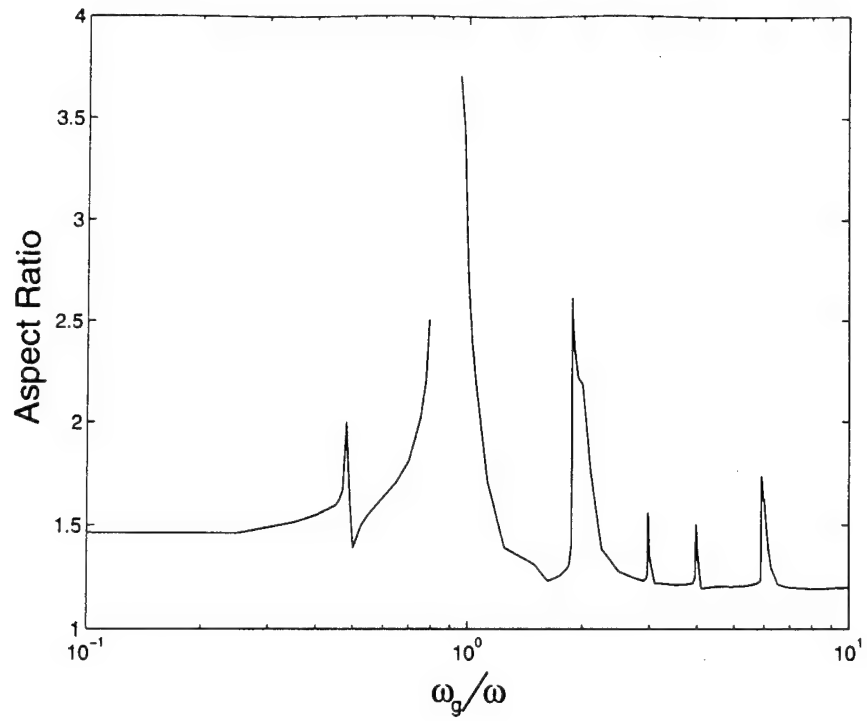
We = 3.0   **We = 4.0**   **We = 5.78**

Figure 7: Droplet Breakup Modes Encountered Under Acoustic Excitation at the Drop's Natural Frequency
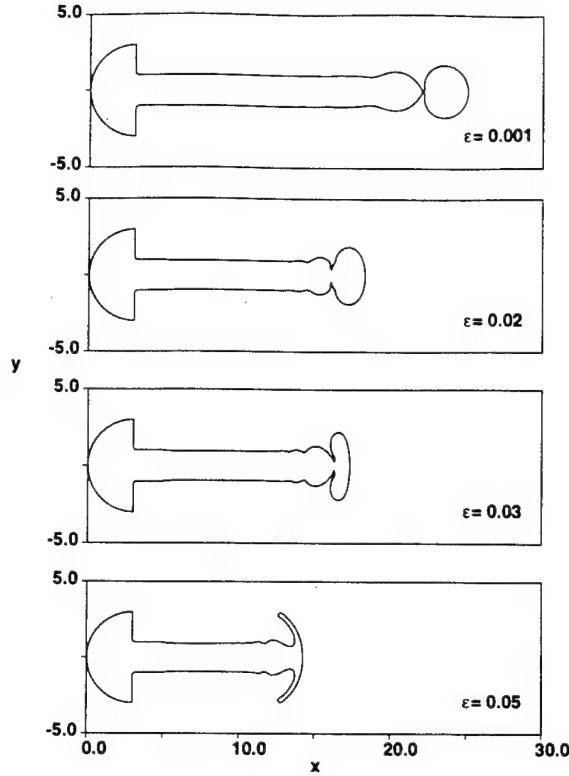
Figure 8: Effect of Gas Density on Initial Liquid Jet Behavior, $We = 17.6$

gas in the chamber. Such conditions exist in high pressure combustion devices such as LREs.

Presently, we are investigating the injector frequency response (both amplitude and phase shift) under a variety of unsteady chamber pressure conditions. Appendix E provides some information in this regard, while additional results will be presented in an upcoming manuscript.

3.6 BEM for Viscous Flows

Substantial progress has also been made in the development of a model capable of addressing liquid-phase viscous contributions to the atomization process. Unfortunately, we were forced to abandon the Dual Reciprocity Method for which we presented some preliminary results last year[12]. This method gave fine solutions for steady flows, but for unsteady flows the resulting matrices turn out to be ill-conditioned, making numerical inversion processes inaccurate. For this reason, we have adopted a zonal scheme in which the viscous region is treated separately via an integral method formulation. Full unsteady simulations are possible using this methodology within the framework of the BEM code which is used to solve for properties within the inner, inviscid region.

A schematic representation of the zonal approach is outlined in Fig. 9. Our original BEM is used to solve for conditions (nodal velocities q and of the boundary layer. Using 4th-order velocity profiles with appropriate solid wall or free surface conditions at the outer edge, the integral method provides an ordinary differential equation of the local thickness, δ. Continuity and conservation of momentum (applied at the outer boundary) provide relationships for the surface velocities, u_s and q_s.

Results from a typical calculation are shown in Fig. 10. The evolution of the boundary layer and free surface is depicted for a case where $We = 10,000$, $Re = 10,000$ and the initial boundary layer thickness (one radii upstream of injection point) is 5% of the orifice radius. These are typical injection conditions for *actual* rocket injector elements. The calculations are initiated by "ramping up" viscosity to the desired level over a period of 2 time units. The growth of the boundary layer during this transient generates a surface wave which convects downstream. At long times, a steady solution exists even under these high-speed injection

Figure 9: Schematic Representation of Zonal BEM/Integral Method for Addressing High-Speed, Viscous Jet Atomization Processes

conditions. Obviously, the presence of the gas and turbulence effects (which are not presently modeled) can be important in this case. Future efforts will be aimed at quantifying interactions due to these physical processes.

4   Professional Activities

The efforts outlined in the previous section of this report were made possible by two grants from AFOSR. A single student, Mr. James H. Hilbing, was supported under the base grant (F49620-94-1-0151). In addition, an AASERT grant (F49620-93-1-0363) was utilized to support Chris A. Spangler, Mark W. Rutz, Michael P. Moses, Ian F. Murray, and Kurt Rump (all U.S. citizens). The following theses were written as a result of these two grants:

Ph.D. Dissertation

Hilbing, J. H., "Nonlinear Modeling of Atomization Processes", August, 1996.

M.S. Theses

Spangler, C. A., "Nonlinear Modeling of Jet Breakup in the Wind-Induced Regime", August, 1994.

Rutz, M. W., "Effect of Transverse Acoustic Oscillation on the Behavior of a Liquid Jet", December, 1995.

Moses, M. P., "Visualization of Liquid Jet Breakup and Droplet Formation", May, 1995.

Murray, I. F., "Nonlinear Modeling of the Acoustically-Induced Oscillations of Droplets", August, 1996.

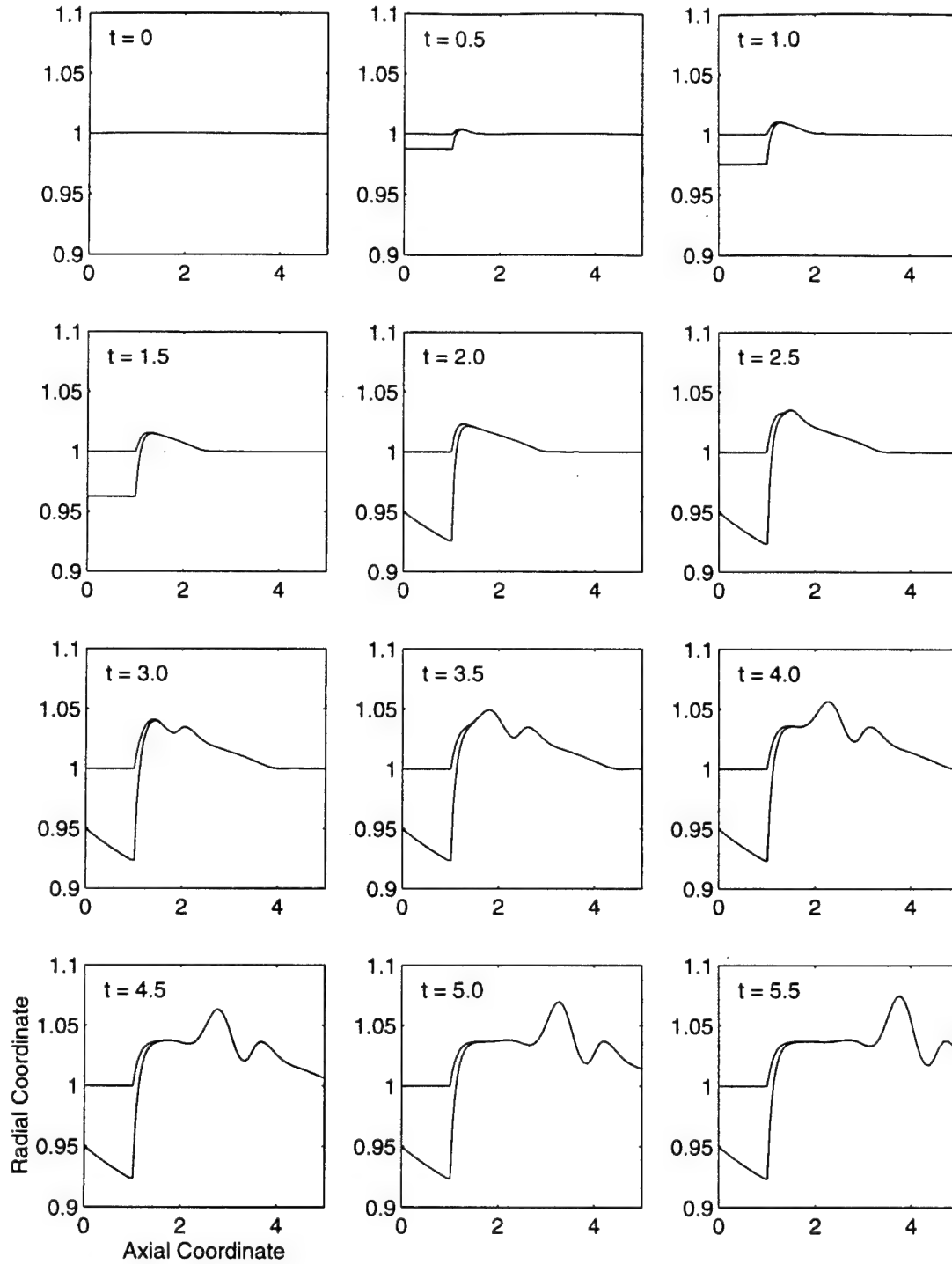Rump, K. M., "Nonlinear Model for a Liquid Jet Injected into a Quiescient Gas", December, 1996.

Figure 10: Unsteady Boundary Layer Development Near Orifice Exit Plane During Transient "Start-Up" Process, $We = 10,000$, $Re = 10,000$

A list of journal publications (and submissions) associated with these efforts are provided in the following list. Highlighted items (*) have been attached in the Appendices of this report.

Refereed Journal Publications and Submissions

1. Spangler, C. A., Hilbing, J. H., and Heister, S. D., "Nonlinear Modeling of Jet Atomization in the Wind-Induced Regime", *Physics of Fluids*, V 7, No. 5, pp 964-971, 1995.
2. Hilbing, J. H., Heister, S. D., and Spangler, C. A., "A Boundary Element Method for Atomization of a Finite Liquid Jet", *Atomization and Sprays*, V 5, No. 6, pp 621-638, 1995.
3. *Hilbing, J.H., and Heister,, S.D., "Droplet Size Control in Liquid Jet Breakup," *Physics of Fluids*, V 8, No. 6, pp. 1574-1581, 1996.
4. *Heister, S. D., Rutz, M., and Hilbing, J., "Effect of Acoustic Perturbations on Liquid Jet Atomization", To Appear, *Journal of Propulsion and Power*, 1995.
5. *Heister, S. D., "Boundary Element Methods for Two-Fluid Free Surface Flows", In Review, *Engineering Analysis with Boundary Elements*, 1996.
6. *Murray, I. F., and Heister, S. D., "On the Response of a Droplet to Acoustic Excitation", In Review, *International Journal of Multiphase Flow*, 1996.
7. Hilbing, J. H., and Heister, S. D., "Coupled Boundary Element/Integral Method for High-Speed Free-Surface Flows", In Preparation, *Engineering Analysis with Boundary Elements*, 1996.
8. Rump, K. M., and Heister, S. D., "Transient Response of Liquid Jet under Unsteady Chamber Conditions", In Preparation, *Atomization and Sprays*, 1996.

A list of the conference papers presented in association with work under these grants is provided in the list below. The starred item is included in Appendix A of this report.

Conference Papers and Presentations

1. Hilbing, J.H., and Heister,, S.D., "A Boundary Element Method for Liquid Jet Atomization Processes", ILASS-94 Conference Proceedings, 5 pages, June 1994.
2. Spangler, C. A., and Heister, S. D., "Nonlinear Modeling of Jet Atomization in the Wind-Induced Regime", ILASS-94 Conference Proceedings, 5 pages, June, 1994.
3. Heister, S. D., Rutz, M., and Hilbing, J., "Effect of Acoustic Perturbations on Liquid Jet Atomization", AIAA 95-2425, 31st AIAA Joint Propulsion Conference, San Diego, CA, 1995.
4. Hilbing, J.H., and Heister,, S.D., "Developments in Nonlinear Modeling of Atomization Processes", ILASS-95 Conference Proceedings, 1995.
5. *Moses, M. P., Collicott, S. H., and Heister, S. D., "Visualization of Liquid Jet Breakup and Droplet Formation", 7th International Symposium on Flow Visualization, Seattle, WA,
6. Hilbing, J.H., Heister,, S.D., and Rump, K., "Recent Advances in Nonlinear Modeling of Atomization Processes", ILASS-96 Conference Proceedings, 1996.
7. Murray, I. F., and Heister,, S.D., "Modeling Acoustically-Induced Oscillations of Droplets", ILASS-96 Conference Proceedings, 1996.

4.1 Technology Transfer/Coupling Activities

Numerous technology transfers have occurred during the period associated with these grants. These items are summarized the the table provided above. Models currently under development should be of great interest to the liquid rocket engine community, since we soon plan to have a fully 3-D capability for high-speed jets. Current models are also applicable to impinging element injectors and blanching problems associated with oxidizer deposition on chamber/injector surfaces.

Table 1: Atomization Modeling: Technology Transfer and Transition

Customer	Result	Application
Lockheed/Martin J. Chrusciel (408) 756-3890	Jet Model for Projectile Control Application	High-Speed Interceptors
Thiokol D. Hawkins/T. Boardman (801) 863-3177	Provided **Hybrid Rocket** Ballistic Computer Code	HYBAL1D Ballistics Code Hybrid Propulsion Demonstration Program
Lockheed/Martin Jim Tegart (303) 977-9740	Boundary Element Modeling of Fluid Slosh Dynamics	Propellant Tank Slosh Analysis
Hewlett Packard Dr. Graham Ross (619) 487-4100	Modeling Liquid Jet under Excitation	Ink Jet Printers
Rockwell Space Systems Mark Ventura (310) 922-0075	Boundary Element Modeling of Fluid Slosh Dynamics	Propellant Tank Slosh Analysis

5   References

1. Reba, I. and Brosilow, C., "Combustion Instability: Liquid Stream and Droplet Behavior," WADC TR 59-720, 1960.

2. Jensen, R., (Ed.), "JANNAF Subcommittee on Combustion Stability - Annual Report," 27th JANNAF Combustion Meeting, Cheyenne, Wyoming, 1990.

3. Unverdi, S.O. and Tryggvason, G., "A Front-Tracking Method for Viscous, Incompressible, Multi-fluid Flows, *J. Computational Physics*, 100, pp. 25-37, 1992.

4. Osher, S., and Sethian, J.A., "Fronts Propagating with Curvature-Dependent Speed: Algorithms Based on Hamilton-Jacobi Formulations", *J. Computatational Physics*, 79, pp. 12-49, 1988.

5. Collicott, S. H., Zhang, S., and Schneider, S. P., "Quantitative Liquid Jet Instability Measurement System Using Asymmetric Magnification and Digital Image Processing", *Experiments in Fluids*, V15, pp345-347, 1994.

6. Hilbing, J. H., Heister, S. D., and Spangler, C. A., "A Boundary Element Method for Atomization of a Finite Liquid Jet", *Atomization and Sprays*, V 5, No. 6, pp 621-638, 1995.

7. D. T. Harrje and F. H. Reardon, "Liquid Propellant Rocket Combustion Instability," NASA SP-194 (1972).

8. B. Dunne and B. Cassen, "Velocity Discontinuity Instability of a Liquid Jet," Journal of Applied Physics, **27**, 577-582 (1956).

9. Pierre Lafrance, "Nonlinear Breakup of a Laminar Liquid Jet," Physics of Fluids, **18**, 428-432 (1975).

10. D. F. Rutland and G. J. Jameson, "Theoretical Prediction of the Sizes of Drops Formed in the Breakup of Capillary Jets," Chemical Engineering Science, **25**, 1689-1698 (1970).

11. Oefelein, J. C. and Yang, V., "Comprehensive Review of Liquid-Propellant Combustion Instabilities in F-1 Engines," *Journal of Propulsion and Power*, Vol. 9, No. 5, 1993, pp. 657-677.

12. Heister, S. D., "Modeling Liquid Jet Atomization Processes", AFOSR Propulsion Contractors Meeting, pp. 34-37, University of Illinois at Chicago, 1995.

6 Appendix A - Liquid Jet Visualization

Moses, M. P., Collicott, S. H., and Heister, S. D., "Visualization of Liquid Jet Breakup and Droplet Formation", 7th International Symposium on Flow Visualization, Seattle, WA, 1995.

Visualization of Liquid Jet Breakup and Droplet Formation

Michael P. Moses, Steven H. Collicott, and Stephen D. Heister
School of Aeronautics and Astronautics
Purdue University
West Lafayette, IN 47907-1282

Introduction

Liquid atomization systems are commonplace in today's industry. Some of the many applications include fuel injection systems, paint application, and spray drying. Even for relatively low speed jets, numerous applications exist. Among these are ink jet printers, droplet generators, and manufacturing processes involving the formation of monodisperse droplets from a column of molten metal. Due to the large number of practical applications, the literature available on this subject is quite substantial. Theoretical treatments of this problem date back to the late 1800's and the fundamental linear analysis of the capillary instability due to Rayleigh[1]. Linear analyses have since increased in sophistication to include the presence of the gas phase[2], viscosity[3], and three-dimensionality[4]. Unfortunately, these models can not address important physical processes which occur at finite surface deformations.

Experiments[5-8] have revealed that a given wave on the surface of the jet breaks into two droplets rather than a single drop as postulated by the linear theory. Rutland and Jameson[6,7] examined the size of "main" and "satellite" droplets formed during this nonlinear process. These data were collected by manually measuring the size of the drop images on photographic plates. Lafrance[8] conducted similar experiments on drop size, using electrostatic separation of main and satellite droplets and subsequent monitoring of fluid volumes collected. While this process is more automated than that used by Rutland and Jameson, it does not permit the recombination of main and satellite drops (due to collisions subsequent to the pinch-off process) which may occur[9].

Theoretical efforts in recent history have also focused on the nonlinearities and the formation of main and satellite droplets from a single instability wave. Weak nonlinearities were considered by including higher-order corrections to the linear theory[5,10]. Recently, full nonlinear simulations of the entire breakup process have been developed through the use of Boundary Element Methods (BEMs). Complete nonlinear simulations have been developed for an infinite inviscid jet. Models have been developed which neglect[11] and include[12] the presence of the gas phase. Hilbing, et al.[13] included the orifice geometry; a simulation for a finite liquid jet.

At present, additional measurements of droplet sizes are required for comparison with the fully-nonlinear models. In the past, measurements of droplet sizes from images has been performed manually, limiting the data available on drop sizes. With digital image processing applied to the data collection process, a large amount of drop size data can be processed efficiently and accurately. Additionally, measurements on the influence of the gas-phase pressure, in the "first wind-induced regime" of break-up are sparse. Previous observations[7,8] did not attempt to address this effect, which is difficult to discern at low jet velocities. Only with accurate resolution of droplet sizes and wave shapes does the potential exist to assess aerodynamic effects in the low-speed region. For these reasons, research was initiated to

expand the drop size database and to address aerodynamic effects within the low speed regime.

Experimental Apparatus

The experimental apparatus is a water tank with acoustic perturber, an orifice, and the optical system. The water tank is a low pressure thin-walled steel tank 56 cm long with a 12.5 cm inner diameter and spherical end caps. The head height of water is fixed to be 30.2 cm. The tank is mounted on a vertical traverse with a range of approximately 115 cm, allowing the optical setup to remain at a fixed height on the table. The traverse is mounted to an optics table with vibration-isolation legs, isolating the experiment from vibrations in the floor. This is found to be important to the success of the experiment. The low pressure tank is used with an orifice of diameter 0.0566 cm and $L/D = 5.11$. The upper chamber of this orifice produces a contraction ratio of approximately 120:1. Distilled water is used for all experiments, with water temperature measured during each run (fairly constant near 20° C throughout). Perturbations are introduced into the liquid jet with a piezoelectric speaker mounted inside the top of the tank.

The optical system is shown in Fig. 1 and consists of the illumination and imaging systems. Collimated white light from a short-pulsed (20 nsec) spark source is used to illuminate the water jet. The center post of the spark source casts a shadow in the center of the beam. Therefore, the centerline of the imaging system is offset from the centerline of the illumination system, as indicated in Fig. 1.

The imaging system magnifies and records a shadow image of the water jet. Because of the magnification required, the object-to-camera distance is small, placing the lens too close to the jet and subjecting it to wetting. Therefore, a pair of achromatic lenses of focal length 20 cm and diameter 4 cm are used to form a 1:1 image of the jet in the intermediate image plane, which is then imaged onto the CCD detector at the desired magnification. A variable-diameter circular iris is located between the achromats and controls the effective F-number of the imaging system.

A Super-VHS format CCD camera is used with the 35 mm lens and extension tubes to image the jet break-up process. The camera has a 0.64×0.48 cm chip with a resolution of 768 streamwise×494 transverse pixels. The short-pulsed spark source assures an instantaneous sample of the jet and drop shapes. A typical image is shown in Fig. 2a.

The magnifications of the complete imaging system, i.e., from object space to pixels in computer memory, are determined for each test run by acquiring images of a target ruler marked in 0.5 mm increments. Magnifications parallel with and perpendicular to the jet axis must be measured separately for the CCD camera in use. Magnifications are determined from spectral analysis (1-D power spectra) of numerous lines within these calibration images. The standard deviation of the magnification measurements is found to be approximately 0.5% in all cases. Without the spectral method, magnification measurement was found to give 3-5% error, and was the largest error source in the experiment.

Digital Image Processing

The edge detection scheme used in this project is an improvement of the method of Collicott, et al.[14], which was applied to an anamorphic imaging system to measure growth rates of waves on liquid jets. The additional purpose of the improved method is to investigate
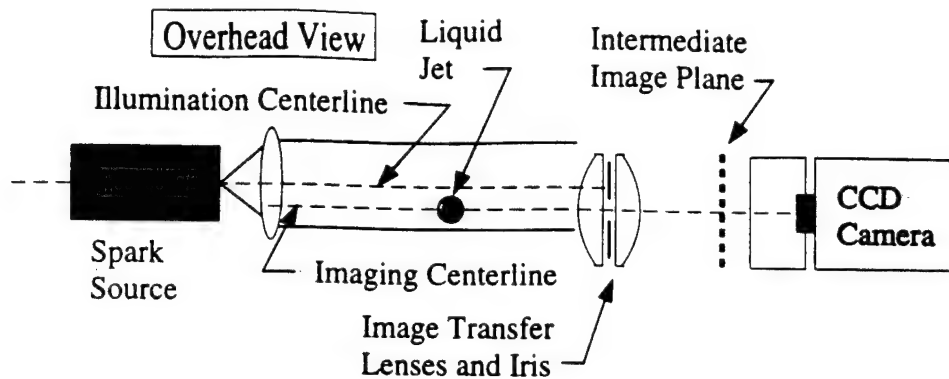
16

Figure 1: Optical Alignment Offset

droplet sizes. Therefore, the edge detection procedure is applied to the image in both directions. Programming effort is required to sort edges in droplets, and to assemble the data from horizontal and vertical scans.

The fundamental operation performed in these methods is to correlate the image greyscale data with the theoretical edge-response of the imaging system. In the present work, the combined effects of diffraction and aberrations are approximated by assuming a circular Gaussian impulse response. This impulse response is analytically integrated in one direction to determine the edge response. The width of the Gaussian is found empirically in the present work. With complete specifications of the lenses, the width could be computed. Empiricism is found to suffice for the present work, in that the basic functions of the correlation: peak formation, noise reduction, and process automation, are not highly sensitive to the choice of the width. For the present work, the speed of direct computation in the spatial domain is sufficient, and is simpler to implement in sub-regions of an image than an FFT-based computation. Each 1-D correlation is scanned for peaks caused by sharp greyscale ramps occurring at edges. The upper plot in Fig. 3 shows the raw intensity levels along the scan line. The black portions ($I(x) = 0$) are the drops while the white area ($I(x) \sim 250$) is the background. The lower plot in Fig. 3 is the result of the correlation of the scan line with the edge response.

Only peaks with intensity greater than a threshold value are considered valid edge locations. In this manner, gradual greyscale shifts (such as the dark region at the top of Fig. 2) are discarded. Edge detection at pixel resolution is obtained by noting the pixel location of the correlation peak. However, edges don't necessarily lie at integral pixel locations, so a "center of mass" calculation yields a sub-pixel edge location. The correlation method reduces the effects of image noise, as seen in Fig. 3 where the correlation is smoother than the image intensity.

A trapezoidal integration is used to compute the area of the droplet image assuming that the calculated area represents the maximum cross-sectional area of an axisymmetric object. Note that multiple views would be required to resolve 3-D effects; assumption of axisymmetry is deemed to be adequate for this study.

Data Reduction Validation

Three validation tests assess the accuracy of the image processing and drop sizing techniques.
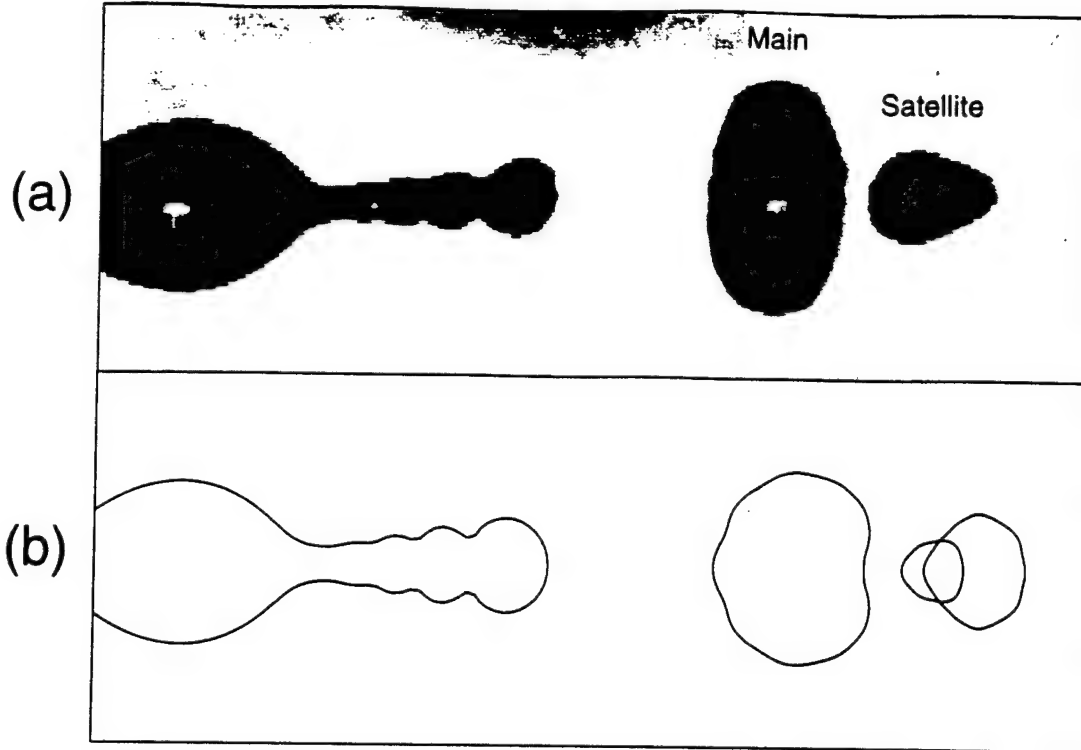
17

Figure 2: (a) Greyscale Image of Typical Droplet Formation. (b) BEM Simulation of Experiment.

The first work compared measured and theoretical wave growth rates in the Rayleigh breakup regime[14], and showed that the concept of correlating the image with the theoretical edge response is an accurate method of edge location. That demonstration was actually an anamorphic imaging system, with a streamwise magnification equal to 1/40 of the transverse magnification.

The error introduced into the digital image processing by the discretization of the edge of a circle into N points was also considered as a validation exercise. Results indicate that this error is rapidly reduced as the number of points is increased, and that for $N > 75$, the error is less than 0.1%. Therefore, to eliminate numerical integration error, images need to be magnified such that the small satellite drops will have at least 75 pixels on the perimeter.

The third verification test examines the accuracy of the entire data acquisition and reduction process in determining the size of droplets. A drill gauge plate is placed in the object plane, and images of the holes are acquired. Error analysis shows that there is a $\pm0.7\%$ error in drop size.

Results

Experiments are performed at two Weber numbers in order to keep jet velocity, and hence, the aerodynamic effects, fixed for different perturbing frequencies. The Weber number, $We = \rho U^2 a/\sigma$, is the dimensionless parameter characterizing this process. Here, U is the mean orifice exit velocity (from volume flowrate measurements), a is the orifice radius, and ρ and σ are liquid density and surface tension, respectively. All experiments are conducted
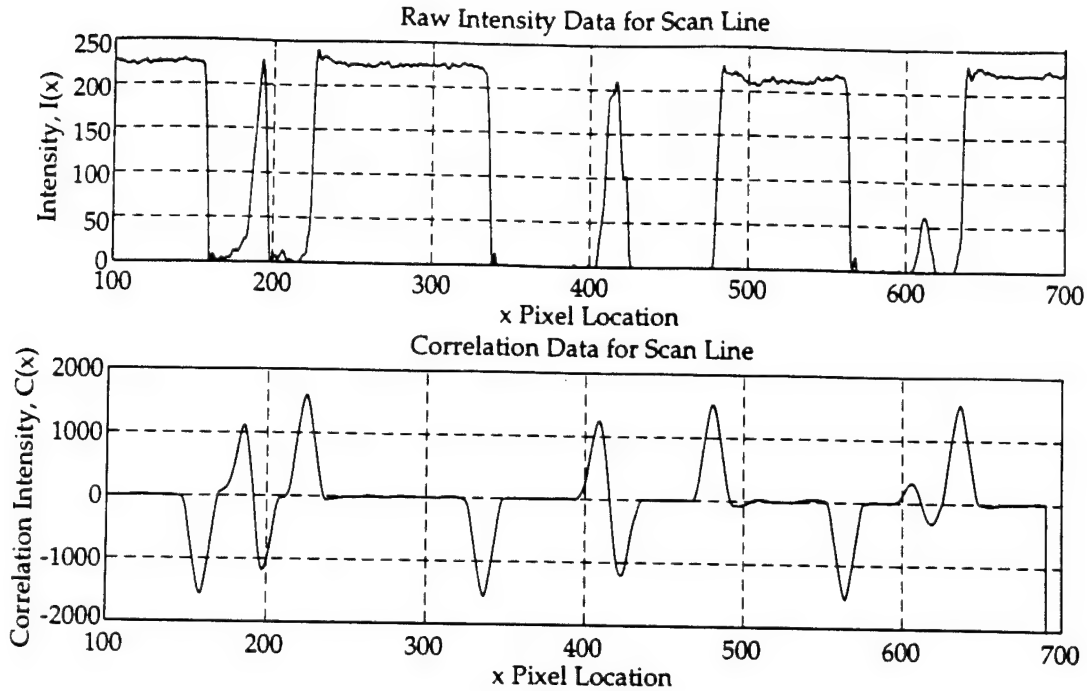
Figure 3: Intensity and Correlation Plots for Sample Droplet Image

with water exhausting into ambient pressure air. The two Weber numbers are 17.6 and 76.6, corresponding to jet velocities of 2.13 and 4.44 m/s, respectively, for this orifice.

By varying the frequency of the speaker at the top of the tank, various dimensionless wave numbers, k, are generated. Linear stability theories indicate that the jet should be unstable for $0 < k < 1$, but in practice it is difficult to force instability for very long (small k) or very short waves due to the tendency of the jet to break up at the most destructive wavenumber, $k \approx 0.7$. Thus, experimental observations are limited to $0.3 < k < 0.85$, similar to that achieved by others[7,8]. Frequencies in the range of 300-1800 Hz produce this wave number range for the two Weber numbers noted above. The measured wave numbers, based on a calculation of the volume of fluid within a single wave near the breakup point, differ noticeably from the expected wave numbers. Measured wave numbers were as much as 10% smaller than the input wave number, attributed to jet (and wave) stretching by gravity and surface tension effects.

A typical image, at $k = 0.447$, and We = 17.6, is compared with numerical simulation[13] in Fig. 2. The image shows the main and satellite droplets, plus a wavy surface on the core column of liquid. This wavy surface is another satellite droplet just prior to pinch. The waves are caused by the "recoil" of the surface after the main drop separates. Note that these features are predicted correctly by the inviscid boundary element method (BEM) simulation, as are the sizes of the main and satellite droplets. The BEM simulation predicts atomization of the satellite as well into two subsatellites whose trajectories merge (indicating possible coalescence). Viscosity may serve to inhibit this process, which is not observed in
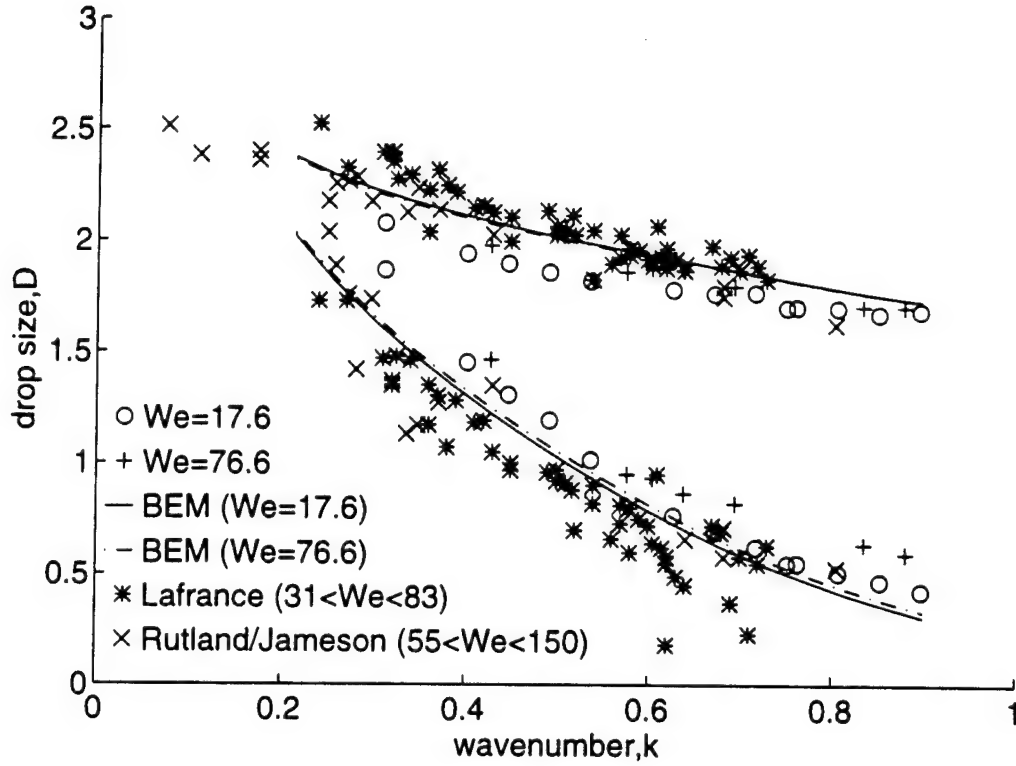
Figure 4: Droplet Size Measurements and Theoretical Results

this particular experiment (but can be observed at lower wave numbers where satellite drops are larger).

A summary of the droplet size measurements from both the present and previous[7,8] studies is compared with BEM predictions[12] in Fig. 4. Wave numbers are adjusted such that the total volume of fluid in main and satellite drops corresponds to the initial column (of radius a) of the same volume. Each of the data from this study represents the average of between two and thirteen independent measurements. At a given set of conditions, the standard deviation of main drop sizes is typically less than 2%, while satellite drops have a larger dispersion ($< 9\%$) due to their lesser size.

Agreement of the present experimental results with those of Rutland and Jameson is quite good, with the exception of four satellite drops in the $0.3 < k < 0.4$ range. Discrepancies here could be caused by formation of subsatellites (which combine with main drops). Agreement of the present data with measurements of Lafrance indicates a systematic bias which may be attributable to the electrostatic data collection of Lafrance. In that technique, one cannot account for the wave stretching phenomena observed in this study and by Rutland and Jameson.

Agreement of the present results with the theoretical BEM predictions also indicates a systematic bias. This is believed to the effect of the inviscid assumption in the BEM model. The BEM results do predict an increase in the size of satellite drops, albeit minor, with increasing Weber number. Comparison of present experimental results indicates a similar trend, but the effect appears to be more pronounced than that predicted with the inviscid
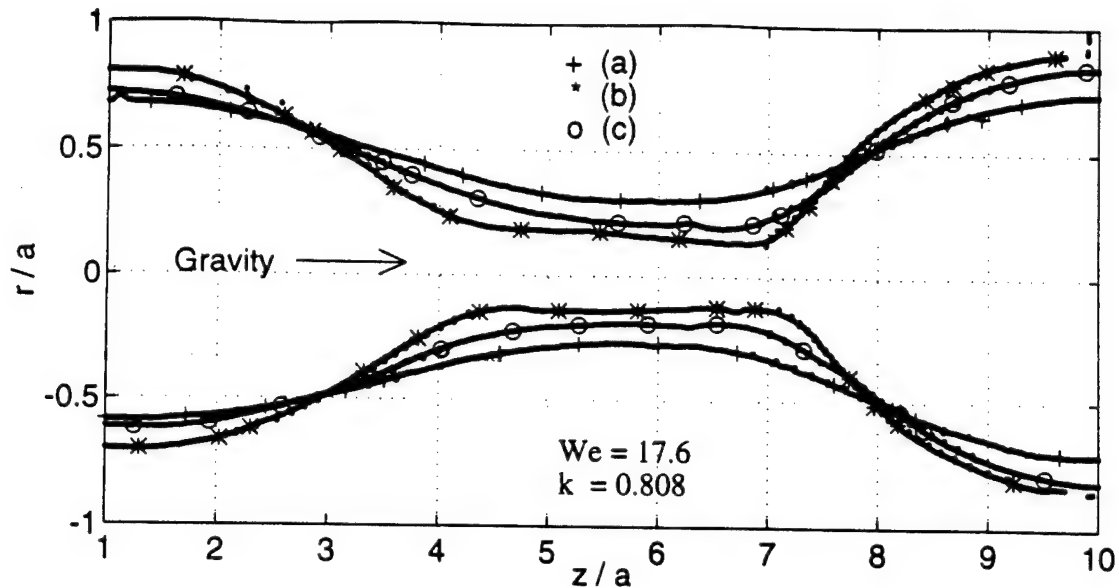
Figure 5: Jet Surface Shape at Different Downstream Positions, We = 17.6, k = 0.808

theory. Nevertheless, the overall comparison between the current measurements and the inviscid theory is quite good.

Numerous images of wave shapes in various stages of the pinch-off process are also obtained in this work. A sampling of these waves is shown in Fig. 5, where curves (a)-(c) were obtained at successive downstream locations. Note the nonlinear wave growth, and the preferential necking of the surface toward the downstream (right) half of a given wave. The preferential necking can not be predicted with an infinite jet analysis, so simulations of a finite-length jet are underway. Many other results of jet surface and droplet images in this experiment are published in Moses[15].

Conclusions

Experiments measuring main and satellite drop sizes show the influence of aerodynamic forces as Weber number is increased, causing the satellite drops to become larger. This effect is also predicted by the BEM model[13]. This effect can not be seen in the previously available data, due to the large scatter in Weber number[6,8]. Investigation of wave shape profiles at We=17.6 and 76.6 compare very favorably with BEM models. This research (see also Moses[15]) has also expanded the database of experimental wave shape profiles available for comparisons.

The benefits of the 1-D theoretical edge-response correlation are sizable: unambiguous and consistent edge location, a large reduction in the effect of image noise on edge location, automation, and the ease of error quantification. Wave shape determination is simple and droplet sizing requires only additional processing. Magnification measurement by spectral analysis of test images reduces the magnification error to a level comparable with other errors in the system. These improvements make possible the detailed investigations of drop sizes and wave shapes for a wide range of jet flows.

Acknowledgements

References

1. Rayleigh, Lord, "On the Instability of Jets", Proc. of London Math. Soc., V. 10, 1878.
2. Weber, C. "Disintegration of Liquid Jets", Z. Agnew Math. Mech., V 11, 1931.
3. Sterling, A. M., and Sleicher, C. A., "The Instability of Capillary Jets", *Journal of Fluid Mechanics*, V 68, pp. 477-495, 1975.
4. Lin, S. P., and Webb, R., "Nonaxisymmetric Evanescent Waves in a Viscous Liquid Jet", *Physics of Fluids*, V6, pp. 2545-2547, 1994.
5. Goedde, E. F., and Yuen, M. C., "Experiments of Liquid Jet Instability", *Journal of Fluid Mechanics*, V40, pp. 495-511, 1970.
6. Rutland, D. F., and Jameson, G. J., "Theoretical Predictions of the Sizes of Drops Formed in the Breakup of Capillary Jets", *Chem. Eng. Sc.*, V25, pp. 1689-1698, 1970.
7. Rutland, D. F., and Jameson, G. J., "A Non-Linear Effect in the Capillary Instability of Liquid Jets", *Journal of Fluid Mechanics*, V46 part 2, pp. 267-271, 1971.
8. Lafrance, P., "Nonlinear Breakup of a Laminar Liquid Jet", *The Physics of Fluids*, V18 N4, pp. 428-432, 1975.
9. Orme, M., "On the Genesis of Droplet Stream Microspeed Dispersions", *Physics of Fluids*, V3, pp. 2936-2947, 1991.
10. Chaudhary, K. C., and Redekopp, L. G., "The Nonlinear Capillary Instability of a Liquid Jet. Part 1. Theory", *Journal of Fluid Mechanics*, V96, pp. 257-274, 1980.
11. Mansour, N. N., and Lundgren, T. S., "Satellite Formation in Capillary Jet Breakup", *Physics of Fluids*, V2, pp. 1141-1144, 1990.
12. Spangler, C. A., Hilbing, J. H., and Heister, S. D., "Nonlinear Modeling of Jet Atomization in the Wind-Induced Regime", *Physics of Fluids*, V 7, pp. 964-971, 1995.
13. Hilbing, J. H., and Heister, S. D., "A Boundary Element Method for Atomization of a Finite Liquid Jet", In Press, *Atomization and Sprays*, 1994.
14. Collicott, S. H., Zhang, S., and Schneider, S. P., "Quantitative Liquid Jet Instability Measurement System Using Asymmetric Magnification and Digital Image Processing", *Experiments in Fluids*, V15, pp. 345-347, 1994.
15. Moses, M. P., *Visualization of Liquid jet breakup and Droplet Formation*, Ph.D. Thesis, Purdue University, 1995.

7 Appendix B - Nonlinear Jet Modeling

Hilbing, J.H., and Heister,, S.D., "Droplet Size Control in Liquid Jet Breakup," *Physics of Fluids*, V 8, No. 6, pp. 1574-1581, 1996.

Droplet size control in liquid jet breakup

James H. Hilbing and Stephen D. Heister
Purdue University, West Lafayette, Indiana 47907

A Boundary Element Method (BEM) has been developed to investigate the nonlinear evolution of the surface of liquid jets injected from circular orifices under unsteady inflow conditions. For fixed wavelength perturbations, the model predicts the formation of main and satellite droplets. The size of the droplets is affected by changes in the perturbation wavelength, perturbation magnitude and Weber number. Satellite droplet velocities are less than main droplet velocities due to the sequential shedding of droplets from the orifice. Using this information, one can determine the likelihood of droplet recombinations downstream of the initial pinching event. © 1996 American Institute of Physics. [S1070-6631(96)02506-8]

I. INTRODUCTION

The breakup of a low speed liquid jet is one of the fundamental problems in two-phase flow. The resultant drop sizes formed from the breakup process are of interest to a variety of industrial processes, such as the manufacture of metal powders via solidification of a stream of molten material. In addition, the performance of ink jet printers is closely tied to the atomization process in the stream of ink emanating from an injection orifice. For these reasons, a wide variety of both analytic and experimental treatments have been applied to this problem.

Early analytic works were performed on linearized governing equations; results led to a prediction that a single droplet is formed from a given wavelength instability on the surface of the jet. Experimental observations, and more recent nonlinear analytic treatments, have revealed that a given wave along the surface actually atomizes into two droplets (termed "main" and "satellite" drops in the literature). Many experiments have been conducted utilizing a small amplitude perturbation in order to create disturbances of a given wavelength[1-4] and to measure the size of resulting main and satellite droplets. Nonlinear models have been developed to analyze this situation by assuming a periodic disturbance along the length of the jet (infinite jet assumption).[5,6] In addition, the effect of the presence of the orifice has been included in recent "finite length" jet simulations.[7] These models have been quite successful in replicating the droplet sizes obtained from the experiments using a small controlled disturbance.

In spite of these advances, many applications would benefit from an ability to provide additional droplet size control via modulation of disturbance amplitude or frequency from a controlled perturbation. For example, wavelengths which would be predicted to be stable on a linear basis could be forced to instability through the use of high amplitude, nonlinear perturbations. Monodisperse droplet trains have been produced in this fashion by Dressler.[8,9] Another alternative is to utilize finite amplitude frequency modulation to affect nonlinear wave deformation processes and control drop size. These notions have been utilized by Orme and coworkers in recent experiments.[10-12] This technique relies on recombination of main and satellite drops due to "microspeed dispersions" between the two bodies. Through experimentation, various manufacturing operations have made use of these ideas to optimize droplet production processes.

While experimentalists and manufacturing disciplines have made progress in controlling droplet sizes using the techniques described above, the approaches have received very little analytic treatment. Models based on the infinite jet treatment cannot be used to analyze these disturbances because of the assumption of periodicity. i.e. the effect of disturbance magnitude increasing as one approaches the orifice cannot be addressed.

However, with the use of a finite-length jet model,[7] the effect of large amplitude perturbations on the behavior of the jet (and resulting drop sizes) can be predicted. In this paper, we discuss the model developed for this purpose and present results for a variety of different injection conditions. The model is described in Section II. Validation of the model is presented in Section III, while results are described in Section IV.

II. MODEL DEVELOPMENT

We assume an axisymmetric, incompressible, inviscid flow in which gas pressure variations are negligible. Under these assumptions, the unsteady liquid flow is described by Laplace's equation $\nabla^2\phi=0$, where ϕ is the velocity potential defined as the function whose gradient is simply the velocity, i.e. $\nabla\phi=\mathbf{v}$.

Following Liggett and Liu,[13] the BEM formulation of Laplace's equation becomes

$$\alpha\phi(\mathbf{r}_i)+\int_\Gamma\left[\phi\frac{\partial G}{\partial n}-qG\right]d\Gamma=0; \tag{1}$$

where $\phi(\mathbf{r})$ is the value of the potential at a point $\mathbf{r}_i$, Γ denotes the boundary of the domain, G is the Green's function corresponding to Laplace's equation, n is the outward normal of the boundary and $q=\partial\phi/\partial n$ is the velocity normal to the surface. The quantity α results from singular contributions due to an integration over the "base point" and is equal to π for nodes along a smooth boundary. At a sharp corner, α is equal to the angle of the corner as measured from inside the domain.[7]
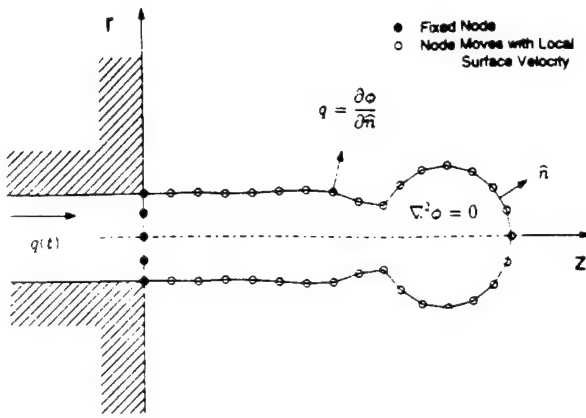
FIG. 1. Computational domain.

The free space Green's function solution to the axisymmetric Laplacian is[13]

$$G = \frac{4rK(p)}{\sqrt{a}}.$$ (2)

with

$$a = (r + r_i)^2 + (z - z_i)^2$$ (3)

and

$$p = \frac{(r - r_i)^2 + (z - z_i)^2}{(r + r_i)^2 + (z - z_i)^2},$$ (4)

where $K(p)$ is the complete elliptic integral of the first kind. The quantity $\partial G / \partial n$ can be expressed:[13]

$$\frac{\partial G}{\partial n} = \frac{-2}{\sqrt{a}} \left[\hat{n}_r K(p) + \frac{E(p)}{(r - r_i)^2 + (z - z_i)^2} \right.$$

$$\left. \times [(r^2 - r_i^2 - (z - z_i)^2)\hat{n}_r + 2r\hat{n}_z(z - z_i)] \right],$$ (5)

where $E(p)$ is the complete elliptic integral of the second kind.

Since Eq. (1) involves an integration only around the boundary, we need not discretize the entire domain. To perform this integration, it is necessary to assume a behavior of ϕ and q over the length of an element, and we assume a linear variation between "nodes" in our model. By assuming a linear variation between nodes, the integration in Eq. (1) becomes a function of geometry alone, and the governing equation can be written in matrix form:[7]

$$[D]\{\phi\} = [S]\{q\},$$ (6)

where the elements of S result from the integration of G, the elements of D result from the integration $\partial G / \partial n$ and the values of α have been incorporated into the D matrix. Presuming that ϕ or q is specified at each node on the boundary, this equation can be solved for the remaining flow variable at each node.

Figure 1 shows the computational domain for the liquid jet. Nodes are fixed in the orifice with a prescribed inflow velocity, so that the BEM solution returns the velocity po-

tential. The velocity potential is specified along the free surface of the jet, and q is returned by the BEM solver. The surface is tracked by allowing the nodes to move with their local velocity vectors. In this case, flow kinematics require

$$\frac{Dz}{Dt} = \frac{\partial \phi}{\partial z}, \quad \frac{Dr}{Dt} = \frac{\partial \phi}{\partial r}.$$ (7)

Here, $\partial \phi / \partial z$ and $\partial \phi / \partial r$ can be written in terms of derivatives parallel and normal to the surface ($\partial \phi / \partial s$ and q) and the local wave slope through a standard coordinate transformation. The derivative $\partial \phi / \partial s$ is obtained via a fourth-order centered difference approximation. The unsteady Bernoulli equation provides the boundary conditions along a free surface interface. Using the liquid density (ρ), orifice radius (a) and mean inflow velocity (U) as dimensions, the nondimensional form of Bernoulli's equation can be written:

$$\frac{\partial \phi}{\partial t} = -\frac{1}{2}(\nabla \phi)^2 - \frac{\kappa}{We} + \frac{Bo}{We}z,$$ (8)

where $We = \rho U^2 a / \sigma$ is the Weber number, $Bo = \rho g a^2 / \sigma$ is the Bond number, σ is the liquid surface tension and κ is the local surface curvature. The Eulerian–Lagrangian transformation for nodes on the interface moving with the *liquid velocity* is

$$\frac{D()}{Dt} = \frac{\partial ()}{\partial t} + \nabla \phi \cdot \nabla ().$$ (9)

Using this transformation, the Bernoulli equation in the liquid becomes

$$\frac{D\phi}{Dt} = \frac{1}{2}(\nabla \phi)^2 - \frac{\kappa}{We} + \frac{Bo}{We}z.$$ (10)

Equations (7) and (10) are integrated in time using a 4th-order Runge-Kutta scheme to solve for the evolution of the liquid jet. To keep a roughly constant grid spacing, cubic splines are used to regrid the surface of the jet every time step.

As the jet issues from the orifice, a droplet will be formed at the tip of the jet and the radial coordinate of the necking region will tend to zero. To extend calculations beyond droplet pinching events, a "pinch criteria" is required to remove droplets from the main body of the jet at times when the radial coordinate in the necking region is still a finite positive value. In the following calculations, we presume that droplet pinching occurs when the minimum radius in the necking region is less than 5% of the orifice radius. When this event occurs, the node at this location is moved to the symmetry axis, and the value of the velocity potential is estimated based on a zeroth-order extrapolation. Approaches similar to this have been verified by other researchers.[6,16] In addition, numerical experiments utilizing differing values of the pinch criteria have verified that near the selected value, droplet sizes and velocities are insensitive to this parameter.

III. MODEL VALIDATION

The axisymmetric BEM solver and free surface modules have been validated with results for the oscillation of a liquid droplet in the absence of gravity.[7] In the linear regime, os-
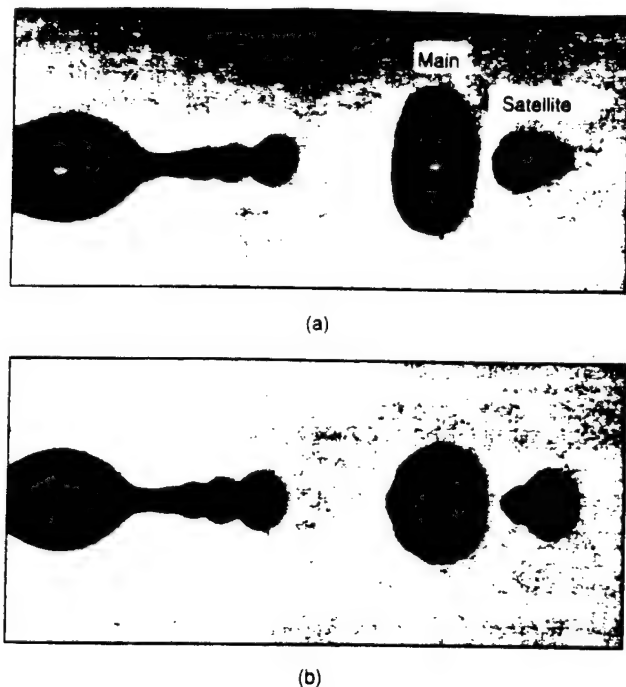
Phys. Fluids, Vol. 8, No. 6, June 1996

J. H. Hilbing and S. D. Heister   1575

25

(a)

(b)

FIG. 2. Jet profile comparison near the pinch location. (a) experiment of Moses. (b) BEM Result. $We = 17.6$, Bo=0.0109, $k = 0.447$.

FIG. 3. Typical jet evolution. $We = 100$, $k = 0.70$, $q' = 2\%$.

cillation frequencies are within one tenth of one percent of the analytical frequency given by Lamb.[14] For moderate oscillations, the BEM solver calculates frequency shifts relative to the linear frequency within 0.5% of the analytic result presented by Tsamopoulos and Brown.[15]

Moses[1] investigated the breakup of a liquid jet with an experimental setup using water in air. He incorporated digital image processing techniques to provide accurate data on droplet size and surface wave shapes. His setup consisted of a tank draining through an orifice with radius $a = 0.0283$ cm and length to orifice radius ratio $L/a = 10.22$. A speaker externally fitted to the tank with an input sine wave from a signal generator provided acoustic perturbations to the jet. The jet was illuminated with a spark source, and imaged by a CCD camera connected to a video tape recorder. Edge detection was by the convolution of a video image of the jet with a mask. Data were collected at fixed Weber numbers of 17.6 and 76.6, and with wave numbers in the range $0.3 \leqslant k \leqslant 0.85$. Figure 2(a) shows a typical jet image near the pinch location with satellite droplet formation.

A BEM calculation was performed in order to match the experimental results of Moses. The numerical simulation used a grid spacing of 20% of the orifice radius, a time step $\Delta t = 0.0025$ and separated droplets when the radial coordinate at the pinch point was within 5% of the orifice radius. Figure 2(b) shows a three-dimensional rendering of the jet profile at time $t = 92.4$ time units. Here, the BEM result was aligned axially with the experimental image such that the breakup point occurs at the same axial location; the inviscid simulation tends to underpredict jet breakup length due to the neglect of viscous effects. This figure shows the excellent qualitative agreement between the experimental and numerical results. Note how the tip of the jet shows a series of three
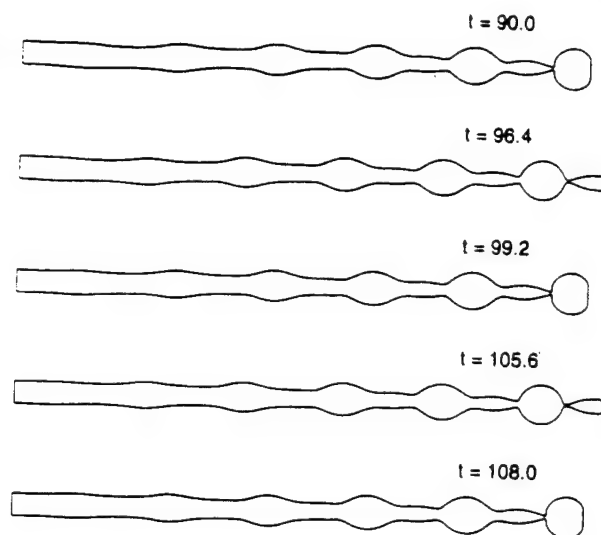
or four ripples formed by the recoil of the surface after the pinching event. In our simulation, these disturbances lead to atomization of the jet tip into 3-4 sub-satellite droplets. Integration of the motion of these sub-satellite droplets show their tendency toward recombination. That is, the satellite droplet shown in Figure 2(b) is actually the superposition of two sub-satellite droplets which were integrated in time separately, and therefore the size of droplet shown is less than the actual size due to this overlap. The model is currently incapable of recombining droplets after pinch.

IV. RESULTS

To simulate experimental results of liquid jet breakup, the computational domain shown in Figure 1 was used with an inflow velocity along the entire orifice exit of the form

$$q = U[1 + q'\sin(kt)], \qquad (11)$$

where q' is the amplitude of the oscillatory disturbance and k is the wave number of the perturbation. Calculations were run for various velocity perturbations, wave numbers, and Weber numbers. Gravity is neglected, so that $Bo = 0$. All calculations begin with a long column of fluid, usually about 15 to 20 orifice radii, outside the orifice in order to ensure that perturbations from the assumed spherical end cap do not influence the development of waves due to the imposed perturbation. The calculations presented here use a grid spacing of 20% of orifice radius, a time step of $\Delta t = 0.0025$ time units (unless noted otherwise), and separate droplets from the calculation when the radial coordinate at the pinch location is within 5% of the orifice radius.

A standard case is chosen as $We = 100$, $k = 0.7$ and $q' = 2\%$. Linear stability analysis shows that this wave number is the most unstable for this Weber number.[17] Figure 3 shows jet profiles for five successive droplet shedding events for the standard case, beginning at $t = 90.0$ time units. By this time, the calculated drop sizes and jet breakup length predicted by the BEM solver have a repeating pattern with very little variation. Periodic bulges appear in the jets due to the

J. H. Hilbing and S. D. Heister

26

TABLE I. Jet breakup simulation results.

We	k	q'	R_{main}	R_{sat}
50	0.7	2%	1.845	0.713
100	0.5	2%	1.946	1.250
100	0.7	2%	1.818	0.867
100	0.9	2%	1.719	0.443
100	1.1	2%	1.616	0.183
100	0.7	3%	1.793	0.986
100	0.7	4%	1.771	1.053
100	0.7	5%	1.762	1.091
100	0.7	6%	1.750	1.136
100	0.7	7%	1.749	1.158

FIG. 5. Droplet radii vs. inflow velocity disturbance magnitude for We = 100, k = 0.7 (o finite-length calculation; ___infinite jet calculation).

unsteady inflow, as noted by Reba and Brosilow.[18] The nonlinear effects on the bulges lead to the formation of "main" and "satellite" droplets, a behavior well known for low-speed jets.

A moderate 2% disturbance magnitude was chosen over typical acoustically-generated perturbation magnitudes in order to keep the jet breakup length to a reasonable size, and therefore make calculation times acceptable. After the jet sheds the fluid from the initial assumed geometry, there were between 255 and 290 nodes on the jet surface during this calculation. The first 77 time units of the calculation required about 500,000 CPU seconds on an IBM RISC/6000 computer. Table I presents a summary of the droplet radii for the calculations in this report.

A. Effect of oscillation magnitude

The effect of the oscillation magnitude on the jet breakup is investigated by six simulations of $q' = 2\%$ through 7%. Figure 4 shows jet profiles for three of these disturbance magnitudes. Each pair of profiles shows the jet at
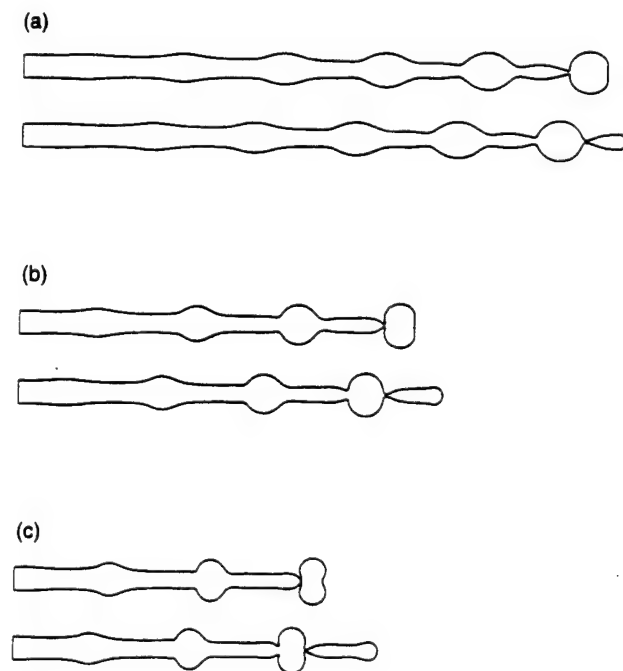

FIG. 4. Effect of inflow velocity disturbance magnitude, We = 100, k = 0.70, (a) $q' = 2\%$, (b) $q' = 4\%$, (c) $q' = 6\%$.

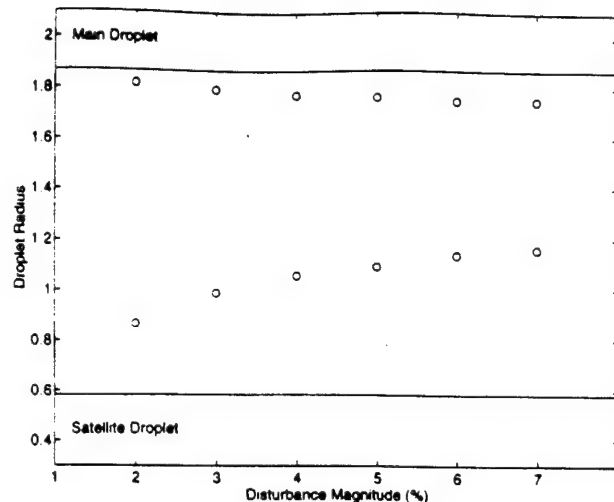times just before a main droplet and a satellite droplet are shed from the calculation. As this figure shows, increasing the size of the perturbation decreases the breakup length and changes the shape of the droplets. At larger disturbance magnitudes, the main droplets take on a "squashed" shape as a result of the high velocity fluid (when $-\pi/2 + 2n\pi < kt < \pi/2 + 2n\pi$) encountering lower velocity fluid which has already exited the nozzle. This phenomena, known as the "Klystron" effect, has been documented qualitatively by numerous researchers[19,20] in the case where forcing perturbations are very large amplitude.

In the other half of the imposed oscillation (when $\pi/2 + 2n\pi < kt < 3\pi/2 + 2n\pi$), the jet is "stretched" since the fluid immediately outside the orifice is at a higher velocity than the inflow. Therefore, the overall effect of increased disturbance amplitude is to narrow the peaks and broaden the troughs in the surface waves on the jet. Breakup times are reduced (as compared to the infinitesimal case) primarily due to the fact that the troughs begin at a lower height.

Calculated droplet sizes are compared with an infinitesimal disturbance[5] values in Figure 5. The satellite size is shown to increase with disturbance magnitude at the wave number ratio selected for these simulations. Necking and pinching of the jet under finite-amplitude disturbance occur at locations much closer to the peak of the wave. The broad, flat troughs created by these perturbations explain the increase in satellite droplet sizes with increasing disturbance magnitude.

Extrapolation to higher q' values would presumably lead to a monodisperse case in which both drops are the same size. Through the use of piezoelectric drivers, droplet trains of this type have been created experimentally by Dressler and coworkers.[8] Direct comparison with these experiments is not possible because pressures are not typically measured in the plenum upstream of the orifice in Dressler's device.
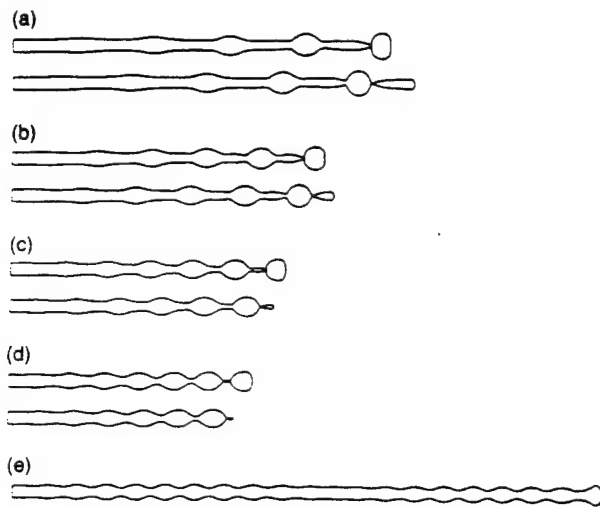
Phys. Fluids, Vol. 8, No. 6, June 1996

J. H. Hilbing and S. D. Heister   1577

27

FIG. 6. Effect of disturbance wave number. $We = 100$, $q' = 2\%$, (a) $k = 0.5$, (b) $k = 0.7$, (c) $k = 0.9$, (d) $k = 1.1$, (e) $k = 1.3$.

FIG. 7. Droplet radii vs. disturbance wave number.

B. Effect of oscillation wave number

Since the jet radius and mean orifice exit velocity are chosen as characteristic dimensions, non-dimensional wave numbers are equivalent to disturbance frequency. Figure 6 shows the effect of wave number on the character of the jet for $We = 100$ and $q' = 2\%$. Each of the first four pairs of profiles show the jet at times just before a main droplet and just before a satellite droplet are shed from the calculation. Increasing the wave number from $k = 0.5$ to $k = 1.1$ tends to decrease the breakup length, even beyond the most unstable wave number, $k_{max} = 0.7$; a trend not predicted by linear theory. In addition, the size of satellite drops tends to decrease with increasing frequency in this range. At a wave number of $k = 1.1$, satellite drops have nearly vanished, indicating that a wave number near this value can produce monodisperse atomization. In fact, viscous effects would probably inhibit the formation of the very small satellite droplet in Figure 6(d). At $k = 1.3$, the breakup length of the liquid jet increases drastically from the previous calculation, and the model no longer predicts the formation of satellite droplets. Figure 6(e) shows the jet profile at time $t = 107.0$ time units; the jet length length is still increasing at this point in the calculation. Note the damping of the waves along the jet surface.

Quantitative predictions of droplet sizes are shown in Figure 7. As in Figure 5, the solid lines are results for infinitesimal disturbances. Here, experimental results are a composite of data from Lafrance[3] and Rutland and Jameson.[2] The finite-amplitude results are for $q' = 2\%$, and they show a tendency to drive conditions toward a monodisperse result by increasing satellite drop size and decreasing main drop size over the entire range of wave numbers investigated. Once again, the peak-sharpening and trough-broadening which occur with increased disturbance magnitude provide an explanation for the observed results. At higher disturbance amplitudes, local curvature in the transition region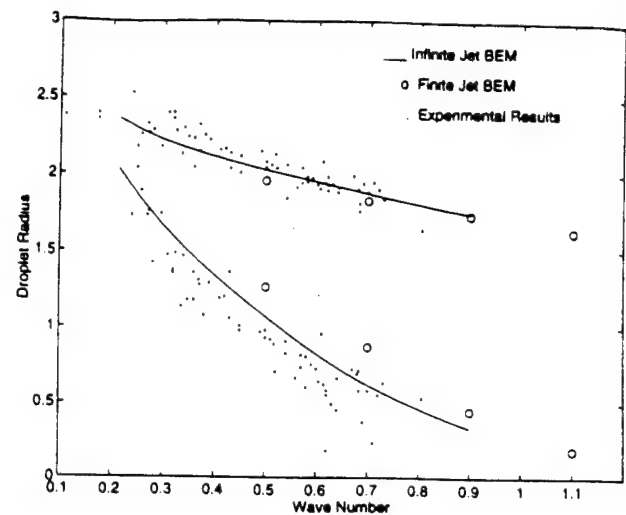 between peaks and troughs can be driven to large enough values to promote nonlinear instability at wavelengths predicted to be stable using linear analysis.

C. Effect of Weber number

For fixed orifice radius and liquid density, decreasing the Weber number corresponds to either increasing the surface tension or decreasing the inflow velocity. As the surface tension is increased, the wave formed on the surface of the jet from the unsteady inflow should tend to grow more quickly, leading to shorter breakup lengths. This effect is shown in Figure 8 for $We = 50$ and 100, using $k = 0.7$ and $q' = 2\%$. Each pair of profiles shows the jet just before a main droplet and satellite droplet are shed from the calculation. Increasing the Weber number also tends to decrease the size of the satellite droplets for the chosen conditions. Note that the tip of the satellite droplet for the lower Weber number case takes on a more spherical shape before being shed from the calculation. In addition, at lower We values, the pinching event tends to form a series of waves on the parent surface due to the enhanced influence of surface tension. This effect
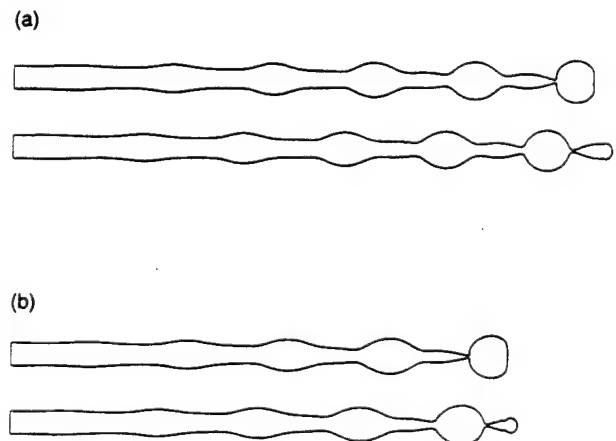

FIG. 8. Effect of Weber number on jet profile, $k = 0.7, q' = 2\%$, (a) $We = 100$, (b) $We = 50$.
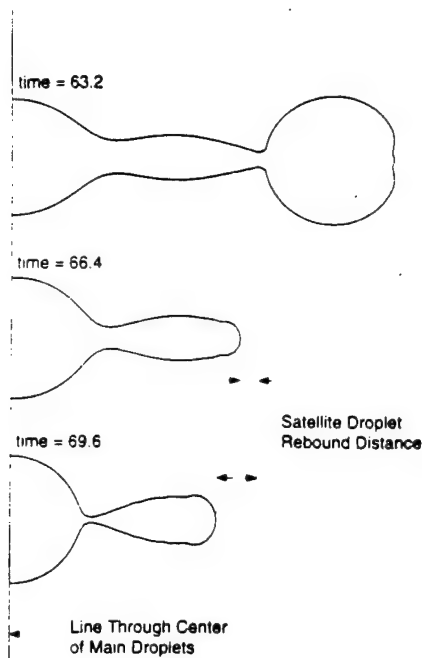
J. H. Hilbing and S. D. Heister

28

FIG. 9. Satellite droplet evolution just prior to shedding.

FIG. 10. Droplet center of mass position and velocity ($We = 100$, $k = 0.7$, $q' = 2\%$).

can also be observed (both in calculations[7] and experimental results[1]) in the low We case shown in Fig. 2.

D. Droplet velocities

Infinite jet simulations lead to droplets with no velocity relative to each other due to the assumption of periodicity over a given wavelength of the jet.[5] However, for finite-length liquid jets, droplets can be shed sequentially, so that the droplet velocities are not necessarily equal to each other or to the orifice velocity. The calculations presented here show that the satellite droplets are shed from the jet with velocities less than that of the main droplets. Figure 9 shows the jet profiles at three times near a droplet pinch. Each profile in this figure has been shifted axially so that the left-hand side of the jet remains in the same relative location. Just after a main droplet is shed from the jet, the surface of the satellite droplet is roughly conical at the tip. Surface tension acts to pull this liquid into a spherical shape, and tends to slow the velocity of the satellite droplet. Note in Figure 9 at $t = 69.6$ time units the distance that the surface has rebounded towards the orifice before the satellite droplet is separated from the calculation. This phenomenon is also present for the main droplets, so that a monodisperse droplet train should have droplets of constant axial velocity slightly less than the mean orifice velocity.

The droplet velocity difference is defined as the percent difference in satellite and main droplet velocities relative to the main droplet velocity. This difference is calculated by integrating the motion of the droplet after being shed from the jet. The position of the droplet's calculated center of mass is differenced to determine the droplet velocity. Figure 10 shows a typical plot of the position and velocity of the center of mass for a main droplet and a satellite droplet. Table II presents velocity differences for selected calcula-
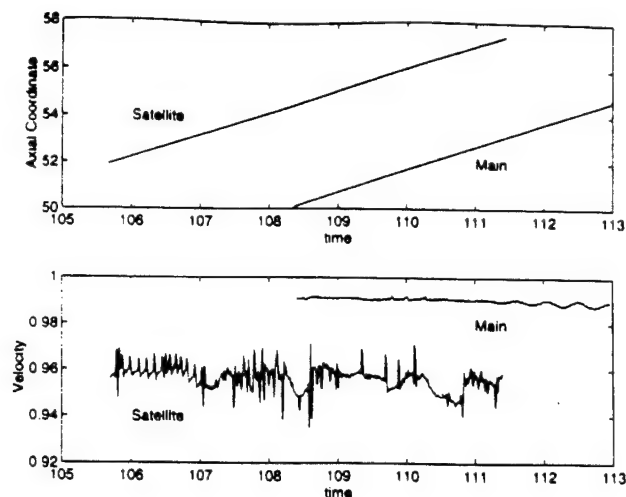
tions. As this table shows, the velocity difference increases when the Weber number decreases, the wave number increases or the disturbance magnitude decreases. This increase in velocity difference can be attributed to increasing surface tension or decreasing satellite droplet size.

Pimbley and Lee[12] investigated satellite droplet formation experimentally, noting the velocity difference between the main and satellite droplets. They found appropriate excitation conditions to separate satellite droplets from either side of a main drop, as well as forming both droplets simultaneously, the so-called "infinite" satellite condition. Satellite droplets not at the infinite condition were found to merge with main droplets a few wavelengths downstream. At the lowest excitation amplitudes, rear-merging satellites were observed in the experiment. These satellite droplets merged backwards with next main droplet. As the amplitude was increased, the velocity difference decreased until the infinite condition was reached. Increasing the amplitude farther resulted in forward-merging satellites, which merged with the parent main droplet. The BEM calculations presented here agree with the low-amplitude experimental results which produced backward-merging satellite droplets.

E. Amplitude modulated disturbances

Orme and Muntz[10] studied the breakup of a liquid jet using amplitude-modulated sinusoidal disturbances. They

TABLE II. Droplet velocity differences.

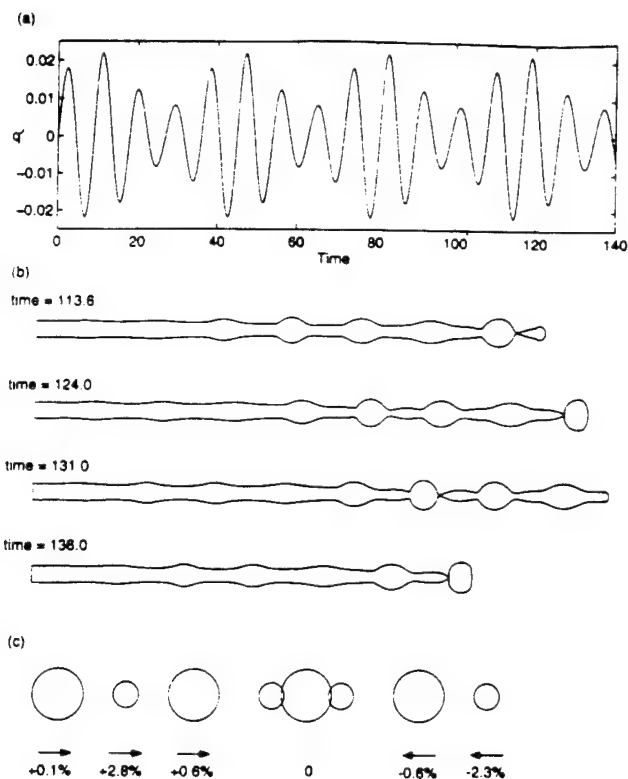| We	k	q'	Velocity difference
50	0.7	2%	$-12.0 \pm 1.4\%$
100	0.5	2%	$-1.4 \pm 0.9\%$
100	0.7	2%	$-3.4 \pm 0.9\%$
100	0.9	2%	$-3.9 \pm 0.9\%$
100	1.1	2%	$-9.8 \pm 4.7\%$
100	0.7	4%	$-1.9 \pm 0.6\%$

J. H. Hilbing and S. D. Heister   1579

29

FIG. 11. Jet breakup with an amplitude-modulated inflow velocity, (a) inflow disturbance waveform, (b) jet profiles at four successive pinch events, (c) relative droplet velocities.

packet, at $t = 131.0$ time units, of two main and three satellite droplets. When this multiple droplet packet is integrated after pinch, the two droplets on the orifice-side of the packet pinch off. The velocity of each droplet's center of mass is calculated, and the arrows in Figure 11(c) show their direction of motion relative to the fluid packet consisting of one main and two satellite droplets. Our results of Fig. 11(c) compare well with Fig. 2 from Orme and Muntz,[10] predicting the formation of a single droplet.

V. CONCLUSIONS

A numerical model has been developed to investigate the influence of unsteady inflow conditions on the nonlinear evolution and droplet formation processes within a low speed, finite-length liquid jet. The size of both main and satellite droplets is predicted under the assumption of a sinusoidal perturbation to the orifice exit velocity. Results indicate that modulation of either the amplitude or the frequency (wave number) of the perturbation can affect droplet sizes so as to create a monodisperse droplet train. In addition, velocity dispersions (between main and satellite droplets) are predicted with the model; therefore, the tendency of droplets to recombine after pinch off can also be addressed.

ACKNOWLEDGMENTS

found that the droplets coalesced downstream due to variations in their velocities. For this type of disturbance, the inflow velocity can be written in the form

$$q = U\left\{1 + \left[q' + q'_m \sin\left(\frac{kt}{N}\right)\right]\sin(kt)\right\}, \qquad (12)$$

where q'_m is the magnitude of the modulated disturbance and N is the modulation frequency ratio.

A BEM calculation was performed in order to simulate these experiments. We chose disturbance magnitudes of $q' = 0.015$ and $q'_m = 0.0074$, which correspond to a 5% fluctuation in the reservoir pressure, a wave number of $k = 0.7$ and a frequency ratio of $N = 4$. Figure 11(a) shows the inflow disturbance waveform corresponding the these values. A Weber number of $We = 200$ is chosen for this simulation in order to limit the CPU time required; gravity is neglected. The jet begins with length $15a$ outside the orifice, and is marched with a time step of $\Delta t = 0.01$ through a number of droplet shedding events.

Orme and Muntz predict the shedding of a fluid packet containing N pairs of main and satellite droplets, the subsequent breakup of this packet into $2N$ droplets, followed by the recombination of these droplets into one large droplet. Figure 11(b) shows the jet profiles at four times just prior to four successive pinch events. These four pinch events include the eight droplets for one complete cycle of the modulation frequency. Instead of a single packet with eight droplets, we find that three packets of one droplet, plus one

[1]M. P. Moses, "Visualization of liquid jet breakup and droplet formation," M.S. thesis, Purdue University, 1995.
[2]D. F. Rutland and G. J. Jameson, "Theoretical prediction of the sizes of drops formed in the breakup of capillary jets," Chem. Eng. Sci. **25**, 1689 (1970).
[3]P. Lafrance, "Nonlinear breakup of a laminar liquid jet," Phys. Fluids **18**, 428 (1975).
[4]K. C. Chaudhary and L. G. Redekopp, "The nonlinear capillary instability of a liquid Jet. Part 1. Theory," J. Fluid Mech. **96**, 257 (1980).
[5]C. A. Spangler and J. H. Hilbing, and S. D. Heister, "Nonlinear modeling of jet atomization in the wind-induced regime," Phys. Fluids **7**, 964 (1995).
[6]N. N. Mansour and T. S. Lundgren, "Satellite formation in capillary jet break-up," Phys. Fluids A **2**, 1141 (1990).
[7]J. H. Hilbing, S. D. Heister, and C. A. Spangler, "A boundary element method for atomization of a finite liquid jet," Atom. Sprays **5**, 621 (1995).
[8]J. L. Dressler, "Two-dimensional, high flow, precisely controlled monodisperse drop source," Wright Laboratory WL-TR-93-2049, 1993.
[9]F. Takahashi, W. J. Schnoll, and J. L. Dressler, "Characterization of a velocity-modulation atomizer," Rev. Sci. Instrum. **65**, 3563 (1994).
[10]M. Orme and E. P. Muntz, "The manipulation of capillary stream breakup using amplitude-modulated disturbances: A pictorial and quantitative representation," Phys. Fluids A **2**, 1124 (1990).
[11]M. Orme, "On the genesis of droplet stream microspeed dispersions," Phys. Fluids A **3**, 2936 (1991).
[12]W. T. Pimbley and H. C. Lee, "Satellite droplet formation in a liquid jet," IBM J. Res. Dev. **21**, 21 (1977).
[13]J. A. Liggett and P. L-F. Liu, *The Boundary Integral Equation Method for Porous Media Flow* (George Allen and Unwin, London, 1983).
[14]H. Lamb, *Hydrodynamics*, 6th ed. (Dover, New York, 1982).
[15]J. A. Tsamopoulos and R. A. Brown, "Nonlinear oscillations of inviscid drops and bubbles," J. Fluid Mech. **127**, 519 (1983).
[16]R. M. S. M. Schulkes, "The evolution and bifurcation of a pendant droplet," J. Fluid Mech. **278**, 83 (1994).

J. H. Hilbing and S. D. Heister

30

[17] A. M. Sterling and C. A. Sleicher, "The instability of capillary jets," J. Fluid Mech. **68**, 477 (1975).

[18] I. Reba and C. Brosilow, "Combustion instability: Liquid stream and droplet behavior," WADC TR 59-720 (1960).

[19] D. T. Harrje and F. H. Reardon, "Liquid propellant rocket combustion instability," NASA SP-194 (1972).

[20] B. Dunne and B. Cassen, "Velocity discontinuity instability of a liquid jet," J. Appl. Phys. **27**, 577 (1956).

Phys. Fluids, Vol. 8, No. 6, June 1996

J. H. Hilbing and S. D. Heister   1581

31

8   Appendix C - Acoustic Interactions with Liquid Jet

Heister, S. D., Rutz, M., and Hilbing, J., "Effect of Acoustic Perturbations on Liquid Jet Atomization", To Appear, *Journal of Propulsion and Power*, 1996.

EFFECT OF ACOUSTIC PERTURBATIONS ON LIQUID JET ATOMIZATION

S. D. Heister [*], M. W. Rutz[†]
and J. H. Hilbing [†]

July 31, 1996

Nomenclature

a = orifice radius
I_m = modified Bessel fct. of 1st kind, order m
K_m = modified Bessel fct. of 2nd kind, order m
k = wave number
n = mode number for column excitation (Eq. 5)
P = pressure
q = velocity normal to local surface
r = radial coordinate
t = time
U = velocity
We = Weber number, $We = \rho_g U^2 a/\sigma = \rho U^2 a/\sigma$ in Figs. 8-12
x = horizontal coordinate
y = vertical coordinate
z = axial coordinate
κ = surface curvature
ρ = density
ϵ = density ratio, ρ_g/ρ
σ = surface tension
ω = oscillation frequency
ϕ = velocity potential

Subscripts
$()_g$ = gas phase

Superscripts
$\hat{()}$ = perturbation quantity

[*]Associate Professor, Member, AIAA
Purdue University, West Lafayette, Indiana, 47907
[†]Graduate Research Assistant, School of Aeronautics and Astronautics. Member, AIAA

Abstract

The effect of unsteady chamber characteristics on the atomization process is investigated using non-linear free-surface models based on Boundary Element Methods (BEMs). Two separate scenarios are considered. In the first case, a liquid column is subjected to transverse oscillations from the gas phase. The second calculation addresses "dynamic orifice massflow" due to the presence of longitudinal acoustic perturbations. Results indicate that the atomization process can be strongly affected by these perturbations. As expected, the most prominent coupling occurs at driving frequencies which are at (or near) the natural frequency of oscillation of the liquid.

Introduction

In a liquid rocket engine (LRE) combustion chamber, the atomization process serves as a precursor to complex vaporization, mixing, and reaction processes. Not only is the atomization process important to characterizing the steady-state performance of a LRE, but it also can play an important role in unsteady processes within the combustion chamber. In fact, numerous authors[1-5] have implicated the atomization process as a mechanism to (at least partially) explain high-frequency LRE combustion instabilities.

Even under steady conditions, our knowledge of the detailed processes leading to atomization of a liquid jet is quite modest. For this reason, there have been relatively few efforts aimed at improving our understanding of injection processes under dynamic conditions. Most previous efforts have been experimental in nature and have been motivated by LRE combustion stability concerns.

One group of experiments have focused on longitudinal acoustic fields[6-9] investigating both low injection velocities[6,7] and high injection velocities[8,9] characteristic of actual LRE injectors. These authors concluded that the presence of a time-dependent pressure field at the injection point leads to a dynamic orifice massflow, even in the event that the injector manifold pressure remains constant. At low injection velocities, this effect leads to periodic "bulges" in the jet diameter; this character also persists into the higher jet velocity regime[6]. In addition, droplet coalescence was effected by the time-dependent injection flowrate. Similar effects have been observed[10,11] when the chamber pressure is held fixed, but the flowrate is varied using piezoelectric drivers upstream of the orifice inlet. At high injection velocities, Ingebo[9] showed a dramatic decrease in mean droplet size with the amplitude of the disturbance. This compelling evidence indicates the importance of the acoustic interaction with the atomization process.

A second group of researchers[5,12-14] have focused on interactions of a liquid jet with a transverse acoustic perturbation. Here, experiments have revealed a broadening of the jet cross-section[14], and a physical deflection of the jet due to the "crosswind" from the acoustic field[13]. Here, the variable massflow effect can also be present due to the fact that the injector manifold reacts to the average pressure at the injector face and distributes fluid spatially in accordance with the local injector face pressure[12].

Analytic models aimed at quantifying the phenomena described above have made heavy use of experimental results. Early efforts[5-7] made use of one-dimensional mass and momentum balances in which liquid and gas phases were decoupled. Other researchers have simply sought to correlate their experimental results with injection and acoustic wave conditions. More recently, the jet broadening phenomena present under some transverse acoustic interactions was quantified using a static equilibrium analysis[14].

While these efforts have advanced our understanding of these processes, the effect of coupling of gas and liquid flowfields in a dynamic environment has yet to be considered. Recent developments

34

of numerical models based on the use of Boundary Element Methods (BEMs)[15,16] permit us to analyze the acoustically-driven interactions described above. The use of the BEM approach provides high resolution of the interface (under very large distortions), as well as the capability to extend simulations *beyond* atomization events. This paper will present simulations of both longitudinal and transverse acoustic wave interactions with an initially-cylindrical column of fluid. Transverse simulations will include coupling of gas and liquid velocity fields and longitudinal simulations will include the effect of dynamic orifice massflow in time-accurate calculations valid for nonlinear deformations of the liquid.

Classification of Acoustically-Driven Instabilities

Before performing the numerical simulations described above, it is prudent to determine the applicable flow regimes in LREs, as well as those studied by other researchers. One important consideration involves the "frequency response" of the liquid to the imposed oscillation. Consider the cylindrical column of liquid subject to either longitudinal or transverse acoustic perturbations as shown in Fig. 1. Variables shown in this figure are defined in the Nomenclature.

For the transverse oscillation in Fig. 1, fundamental frequencies are obtained from a linearized, inviscid, 2-D analysis similar to the classic axisymmetric analysis used by Lamb[17] in the case of a droplet. In the 2-D case, it is straightforward to show that velocity potentials satisfying Laplace's equation in the liquid and gas phases can be represented:

$$\phi = \frac{\hat{a}\omega}{n}(r/a)^n \cos(n\theta)\cos(\omega t) \tag{1}$$

$$\phi_g = -\frac{\hat{a}\omega}{n}(a/r)^n \cos(n\theta)\cos(\omega t) \tag{2}$$

assuming a surface shape $r = a + \hat{a}\cos(n\theta)\sin(\omega t)$. Here, n is the order of the oscillation and we will assume that $\hat{a}$ is a perturbation ($\hat{a} << a$). Since the column is initially at rest, the linearized result from Bernoulli's equation can be expressed:

$$P - P_g = \frac{\sigma}{a} - \rho\frac{\partial\phi}{\partial t} + \rho_g\frac{\partial\phi_g}{\partial t} = \kappa\sigma \tag{3}$$

where κ is the linearized curvature of the distorted surface:

$$\kappa = \frac{1}{a}[1 - \frac{\hat{a}}{a}(1 - n^2)\cos(n\theta)\sin(\omega t)] \tag{4}$$

Combining Eqs. 1-4, we obtain the fundamental frequencies of oscillation of the column:

$$\omega^2 = \frac{n(n^2 - 1)\sigma}{(\rho + \rho_g)a^3} \tag{5}$$

As in the case of a droplet[17], we see that the lowest order mode is for $n = 2$. In this case, the fundamental frequency is given by $\omega^2 = 6\sigma/((\rho + \rho_g)a^3)$ which gives a result 13% lower than that of a droplet in a low density gas.

For the case of a longitudinal excitation, the fundamental frequency of the liquid column can be determined by analysis of a dispersion relation[18] which describes the variation of ω with changes in wave number, k:

$$\omega^2(\frac{I_0(k)}{\epsilon I_1(k)} + \frac{K_0(k)}{K_1(k)}) + 2ik\omega - k^2\frac{K_0(k)}{K_1(k)} - \frac{k(1 - k^2)}{We} = 0 \tag{6}$$

35

Table 1: Frequency Characterization, Acoustic Interactions

Researcher(s)	$\Delta P/P$	$\epsilon x 10^3$	We	Frequencies in Hz	
				ω_g	ω
Reba & Brosilow[6] (L)	0.03-0.49	1.2-4.2	0.38-21	250-500	4-2700
Ingebo[9] (L)	0.11-0.22	0.5-4.4	47-1700	1190	600-373,000
Miesse[4] (T)	—	1.2	—	1100-8800	100-400
Hoover, et. al.[14] (T)	0.0046-0.055	1.2-14	0.03-80	500-2500	470-920
Oefelein & Yang[19] (T)	0.65-4.0	17.8	—	454-538	$80 - 270^*$

Note: (T), (L) denote tangential and longitudinal modes, respectively.
* - Fuel and oxid. orifices for 5U and Double-Row Cluster injectors.

Here, we assume that variables have been nondimensionalized using the jet radius, jet velocity, and liquid density as dimensions. Under this assumption, the density ratio, $\epsilon = \rho_g/\rho$, and the Weber number, $We = \rho_g U^2 a/\sigma$, are the relevant dimensionless groups. Equation 6 is developed assuming a jet deformation of the form:

$$r = 1 + \frac{\hat{a}}{a}e^{\omega t + ikz} \tag{7}$$

such that the real part of ω corresponds to the "growth rate" of disturbances with wave number k and the imaginary part of ω represents the characteristic frequency of disturbances traveling along the surface. Following Sterling and Sleicher[18], we presume that after some finite time, only the disturbance with maximum growth rate will be present. By iterating on various k values, we can find the wave number of the disturbance satisfying this criteria and determine the fundamental frequency response (imaginary part of ω) corresponding to this condition.

Using these notions, we can characterize the frequency and flow regimes investigated by various researchers, as well as those present in engines which have experienced combustion instabilities. Data resulting from this procedure are summarized in Table 1. This table summarizes experimental results from cold flow[4,6,14] and combusting[9,19] flows with imposed oscillations. Ingebo[9] ran a series of combusting experiments under oscillating chamber pressure conditions (created using a siren at the chamber exit), while Oefelein and Yang[19] report on the extensive data available from stability testing of the F-1 engine. This engine exhibited tangential-mode instabilities in many of the early injector designs. In the case of transverse oscillations, Weber numbers in Table 1 are based on estimated peak crossflow velocities and liquid frequencies are calculated using the primary ($n = 2$) mode in Eq. 5. For longitudinal oscillations, Weber numbers are based on jet velocity, and ω values are calculated from Eq. 6.

Results indicate that frequencies observed in firings (or utilized in tests) are within (or near) the natural frequency range of the liquid columns. In particular, the observed instability frequencies in the F-1 engine are very near the natural frequency of oscillation for fuel jets used in early (unstable) injector designs for this engine. Since $\omega \propto a^{-1.5}$, the natural frequency of the column doubles with a 37% reduction in jet radius (presumed to occur with the shedding of drops from the periphery). Therefore, it will be fruitful to investigate jet response near the condition $\omega \approx \omega_g$ to investigate coupling between the atomization process and the acoustic modes from the chamber.

Modeling Approach

Liquid jet atomization problems represent significant challenges to modelers due to the nonlinear nature of the free surface, and viscous and turbulence effects. Current models are unable to address all these physical processes. The present analysis is intended to shed some light on the gross response of liquid jets to both longitudinal and transverse acoustic oscillations. In particular, we will presume that both liquid and gas phases are incompressible and inviscid with negligible turbulence in the flow. The lack of viscosity in the gas implies that pressure distributions in separated regions will not be resolved. In the liquid, viscosity does not alter the basic surface shape unless droplet sizes are of the same order as the boundary layer thickness.

Many authors have proposed that the gas field can be treated as locally incompressible in analyzing the flow of the gas around the liquid jet. This assumption is valid when the wavelength of the acoustic disturbance is much larger than that which is applicable to the liquid. In our case, wavelengths in the gas phase are proportional to combustion chamber dimensions, whereas, the wavelength in the liquid jet is proportional to the orifice size. Since the orifice is typically 2-3 orders of magnitude smaller than the applicable chamber dimension, the incompressible gas phase assumption is prudent.

In this section, we will choose the jet radius (a), liquid density (ρ), and a characteristic velocity (U) as dimensions. Under this nondimensionalization, the Weber number, $We = \rho_g U^2 a / \sigma$ and the gas/liquid density ratio, $\epsilon = \rho_g / \rho$ are the two dimensionless variables characterizing these flows. For an inviscid gas or liquid domain, velocity potentials ϕ_g, ϕ exist and must satisfy Laplace's equation:

$$\nabla^2 \phi = \nabla^2 \phi_g = 0 \tag{8}$$

The unsteady Bernoulli equation provides conditions relating velocity potentials at the gas/liquid interface:

$$\frac{\partial \phi}{\partial t} + \frac{1}{2}(\nabla \phi)^2 + P_g + \frac{\kappa}{We} = 0 \tag{9}$$

where P_g is the dimensionless gas pressure at the interface, and κ is the local surface curvature. On the gas side of the interface, Bernoulli's equation is:

$$\epsilon \frac{\partial \phi_g}{\partial t} + \frac{\epsilon}{2}(\nabla \phi_g)^2 + P_g = 0 \tag{10}$$

Mathematically, Eqs. 8-10 provide a well-posed set of equations for velocity potentials, the gas pressure at the interface, and the shape of the interface (implicit in the surface curvature, κ). This set of equations is solved using a Boundary Element Method (BEM) which begins with an integral representation of Laplace's equation:

$$\alpha \phi(\vec{r_i}) + \int_{\Gamma} [\phi \frac{\partial G}{\partial n} - qG] d\Gamma = 0 \tag{11}$$

where $\phi(\vec{r_i})$ is the value of the potential at a point $\vec{r_i}$, Γ denotes the boundary of the domain, and G is the free-space Green's function corresponding to Laplace's equation. An analogous form of Eq. 11 can also be derived for the gas phase potential. For a well-posed problem, either ϕ or $q = \partial \phi / \partial n$ must be specified at each "node" on the boundary. Here n is the outward normal to the boundary so that q represents the velocity normal to the boundary. The quantity α in Eq. 11 results from singularities introduced as the integration passes over the boundary point, $\vec{r_i}$.

Using this methodology, models have been developed for both two-dimensional[20] and axisymmetric[15] flowfields. If we let r and z denote radial and axial coordinates, respectively, and denote the base

37

point with subscript "i", the Green's function solution to the axisymmetric Laplacian can be written:

$$G = \frac{4r K_e(p)}{\sqrt{(r + r_i)^2 + (z - z_i)^2}} \tag{12}$$

where

$$p = \frac{(r - r_i)^2 + (z - z_i)^2}{(r + r_i)^2 + (z - z_i)^2} \tag{13}$$

and $K_e(p)$ is the complete elliptic integral of the first kind. For computational efficiency, this quantity is calculated using a curve fit[15] which has an accuracy to 10^{-8}.

In the case of a 2-D flow (letting x and y represent the coordinates), we have:

$$G = \frac{1}{2\pi} \ln |\vec{r} - \vec{r_i}| = \frac{1}{4\pi} \ln[(x - x_i)^2 + (y - y_i)^2] \tag{14}$$

In both cases, we presume that both ϕ and q vary linearly along the length of a given element. This assumption permits the construction of a set of matrices involving the nodal values of ϕ and q and the integrals (over a given element) given in Eq. 11. For the 2-D flows, integration across a segment can be carried out analytically. Singularities resulting from integration across a segment containing the base point are also integrable[20]. In the case of axisymmetric flow, the integrations must be carried out numerically[15]. In this case, we choose a four-point Gaussian quadrature for evaluation of integrals. Logarithmic singularities which arise in the elliptic integral when the segment contains the base point are treated with a special Gaussian integration designed to accurately treat this condition.

Nodes on the interface are assumed to travel with the local liquid surface velocity, so a transformation from the Eulerian to Lagrangian reference frame is required. After this transformation, Eqs. 9 and 10 become:

$$\frac{D\phi}{Dt} = \frac{1}{2} (\nabla \phi)^2 - P_g - \frac{\kappa}{We} \tag{15}$$

$$P_g = -\frac{\epsilon}{2} (\nabla \phi_g)^2 - \epsilon \frac{D\phi_g}{Dt} + \epsilon \nabla \phi \cdot \nabla \phi_g \tag{16}$$

In these expressions, the notation D/Dt denotes changes in time for nodes moving with the liquid interfacial velocity.

Surface slope and curvature are obtained from a 4th-order treatment to insure accurate resolution of the surface. Cubic splines are used to fit current locations of surface nodes for the purpose of regridding as the calculation proceeds. Regridding is necessary in many calculations because of the tendency of nodes to "bunch" in regions of highest curvature. Models have been validated (for nonlinear calculations) to insure that solutions are insensitive to the grid which has been selected. Droplets are assumed to be "pinched" from the main body of fluid if a node lies within 5% of the orifice radius of the centerline (or another node). Numerous validations have proven that solutions are insensitive to this "pinch criterion". Using this methodology, the BEM formulation permits accurate solution of highly-distorted interfaces in an unsteady flow.

Computational Grids and Boundary Conditions

Transverse Mode Simulations

Figure 2 highlights the computational grid and boundary conditions employed for coupled, 2-D simulations of a liquid column subjected to an acoustic oscillation. For this problem, the Weber

number (We), gas/liquid density ratio (ϵ), and gas/liquid frequency ratio (ω_g/ω) are input parameters for a given simulation. Assuming quantities are nondimensionalized using the liquid density, column radius, and peak acoustic velocity, the dimensionless liquid column natural frequencies (Eq. 5) can be written:

$$\omega^2 = \frac{\epsilon n(n^2 - 1)}{(1 + \epsilon)We} \tag{17}$$

We presume that the acoustic oscillation can be represented by a simple sine wave, so that the gas-phase velocity potential far from the column may be written:

$$\phi_g = x \sin(\omega_g t/2) \tag{18}$$

The factor of $1/2$ is included inside the sine function to account for the fact that the inviscid solution is insensitive to the direction of gas flow. Numerical experiments indicate that farfield conditions may be accurately assumed if the outer gas boundary is placed 15 jet radii from the origin.

For nodes along the symmetry axis in Fig. 2, the normal velocity, q, is assumed to be zero, while the Bernoulli conditions (Eqs. 15 and 16) provide the necessary boundary information for liquid and gas nodes lying on the free surface boundary. A stable, accurate, treatment of the coupling of the two flows through the gas pressure (which appears in both Eqs. 15 and 16) has been developed[15,20]. The treatment begins by solving for liquid surface velocities from Eq. 11 and noting that $q_g = -q$ on the surface since we are tracking nodes with respect to the motion of the liquid. Given the q_g value on the surface, solution of the analagous form of Eq. 11 provides current values for ϕ_g on the interface. The current gas pressure is then computed from Eq. 16 by approximating the $D\phi_g/Dt$ term using a first-order backward difference. Finally, new values of ϕ on the interface (for the next timestep) are obtained via integration of Eq. 15. Simulations presented in the following section employ 17-33 nodes along the interface and typically run in a few hours on a Sun Sparcstation 5 using a dimensionless time step of 0.005.

Longitudinal-Mode Simulations

Longitudinal-mode simulations are performed by assuming that an oscillation in chamber pressure at the injector face will lead to a dynamic massflow through the orifice. Under this assumption, we employ the axisymmetric model of Hilbing, et al.[15] with an unsteady inflow as indicated in Fig. 3. For this calculation, the presence of the gas is neglected, and nodes placed along the orifice exit plane are held fixed. Along this inflow boundary, the velocity is assumed to be:

$$q = 1 + q' \sin(\omega_g t) \tag{19}$$

where q' is the fractional change (in magnitude) of the velocity due to pressure oscillations at the injector face. The oscillation is assumed to be at a frequency identical to that of the acoustic disturbance, and velocities are nondimensionalized against the mean velocity exiting the orifice.

For nodes lying on the free surface, Eq. 11 (with $P_g = 0$) is integrated in time to give ϕ values along the interface which serve as boundary conditions. Gravity is neglected in the simulations since its influence is very small for high-speed jets. Typical solutions employ a grid spacing corresponding to 20% of the orifice radius. Run times can vary substantially (from a few hours, to several days) depending on the length of the jet, i.e., long jets have a large number of nodes and require more calculations per timestep.

Results

Transverse Mode Simulations

For all simulations presented here, a gas/liquid density ratio of $\epsilon = 0.01$ has been assumed. This value is typical of high pressure combustion conditions as can be noted in Table 1. Parametric studies involving this parameter[20] indicate that jet behavior is not terribly sensitive to ϵ for low density ratios.

Under this assumption, the response of a column to an acoustic oscillation at the lowest-order natural frequency of the jet ($\omega_g = \omega|_{n=2}$) is shown in Fig. 4 for a Weber number of 0.1. As expected, we see a strong response under these conditions, with the distortion increasing with each successive period of the oscillation. However, for long times (several periods), a very interesting behavior results. This behavior is best observed by plotting the time history of the position of a node on the top of the column, as shown in Fig. 5. Here we note that the overall magnitude of the distortion *is bounded* even though there is no dissipation in this inviscid simulation.

The explanation for this phenomena lies in the nonlinear behavior of the column itself. For finite deformations, the natural frequency of oscillation is reduced from that predicted by linear theory. This effect is well documented for oscillations of liquid droplets, but has not been investigated substantially for liquid columns. Figure 6 shows the nonlinear frequency shift as a function of initial surface deflection for both droplets and columns. As the jet distorts due to excitation at its linear natural frequency, further excitation at this frequency will actually become destructive for some level of column deformation. Beyond this point, the oscillation will decay (as shown in Fig. 5) until the cycle repeats.

The overall frequency response of the column is shown in Fig. 7. As expected, we see a strong peak at excitation frequencies near the natural harmonic ($n = 2$) frequency of the column. However, it is quite interesting to note that very little response is obtained for *all* other frequencies in the domain. There is a small peak at the subharmonic $\omega_g = \omega_{Nat}/2$, but there is very little activity at the higher order (4th, 6th, etc.). We expect very little response if $\omega_g >> \omega$ since the jet inertia does not permit reactions on this short time scale. In the other limit $\omega_g << \omega$, the column response is nearly quasi-steady and peak deflections are simply a function of We. Note that at this condition ($We = 0.1$) very little jet broadening would be predicted for a steady crossflow as indicated in the far left half of the curves in Fig. 7.

These results have obvious implications to LRE combustion instability. A design which has transverse acoustic modes near the jet natural frequency (n=2 in Eq. 6) will be subject to coupling from wave structures present in the gas domain. If the jet broadens substantially, its drag will increase and it will be more subject to deflection by the transverse flow. For impinging element designs, the broadening will have direct consequences on the atomization/mixing in the impingement region. As indicated in Table 1, the F-1 injector natural frequencies do lie near the range of tangential acoustic frequencies experienced during testing of this engine. Therefore, this phenomenom could explain (at least in part) the tangential stability problems encountered by this engine. The "good news" is that this phenomenom appears to be limited to the lowest-order natural frequency of the column; subharmonics and higher harmonics do not play a substantial role as indicated in Fig. 7.

Longitudinal Mode Simulations

Currently, simulation of a three-dimensional, viscous, turbulent, two-phase flow which corresponds to "real world" conditions is well beyond current modeling capabilities. For this reason, the longitudinal simulations have been limited to a relatively low velocity regime in which the assumptions

of axisymmetry and inviscid flow are most appropriate. The main focus of these simulations is to address the effects of unsteady perturbations on the character of breakup under these assumptions. Since the simulations in this section do not include the influence of gas-phase pressure variations about the jet, the Weber number is defined in terms of the *liquid* density. A Weber number of 100 is assumed for results presented herein.

Figures 8 and 9 address the effect of the effect of disturbance magnitude on the atomization process for a disturbance at the jet natural frequency. In this case, analysis of Eq. 6 indicates that a dimensionless frequency of $\omega \approx 0.7$ generates waves of the most unstable length. In Fig. 8, one can note that nonlinear effects lead to the formation of a "main" and "satellite" droplet from a single wavelength of the instability. This behavior is well known for low-speed jets. Periodic bulges appear in the jet due to the unsteady inflow, as noted experimentally by Reba and Brosilow[6].

Increasing the size of the perturbation not only decreases jet breakup length, but also effects the shape and size of both main and satellite drops. As q' is increased, main droplets take on a "squashed" shape as a result of high velocity fluid (when $\sin(\omega t) > 0$) encountering lower velocity fluid which has already exited the nozzle. This phenomena, known as the Klystron effect, has been documented qualitatively by numerous researchers[1,8,19]. Quantitative comparisons of droplet sizes are compared with an infinitessimal disturbance[16] in Fig. 9. Note that the inviscid predictions match experiments quite well in this regime. Viscosity tends to slow down the breakup process, but does not fundamentally change droplet sizes in this flow regime. The satellite size is shown to increase with perturbation amplitude at the frequency ratio selected for these simulations. Extrapolation to higher q' values would presumably lead to a monodisperse case in which both drops are the same size. Through the use of piezoelectric drivers, droplet trains of this type have been created experimentally[10].

Figures 10 and 11 address the effect of disturbance frequency on the character of the jet. As in the case of amplitude dependence (Figs. 8,9), the jet behavior is also frequency dependent. In this case, increasing disturbance frequency tends to decrease breakup length even beyond $\omega_g/\omega > 1$; a trend not predicted by linear theory. In addition, the size of satellite drops tends to decrease with increasing frequency as shown in Fig. 10. At a frequency ratio of 1.57, satellite drops have nearly vanished indicating that a frequency near this value can produce monodisperse atomization. In fact, viscous effects would probably preclude the formation of this very small structure. Quantitative predictions of droplet sizes are shown in Fig. 11. Here, the solid lines reflect results for an infinitessimal perturbation, as in Fig. 9 and the datapoints are measurements of Rutland and Jameson[21] and Lafrance[22].

A final simulation was conducted for the case of a high Weber number ($We = 1000$), large amplitude ($q' = 10\%$), perturbation. A time sequence for this case is shown in Fig. 12. In this case, the Klystron effect leads to a large radial broadening of the jet, as observed in numerous experiments[1,8,23]. Large perturbations of this nature have obvious repercussions to jet behavior, causing clustered "clumps" of fluid at locations corresponding to peak flowrates during the unsteady process. In addition, the droplets formed from the annular rings of fluid shown in Fig. 12 will be much smaller than drops formed from a "steady" atomization process; an effect observed by Ingebo[9]. Additional modeling efforts will be required to obtain a more quantitative evaluation of this effect.

Conclusions

Nonlinear two-dimensional and axisymmetric numerical simulations have been applied to simulate the effect of acoustic perturbations on liquid jet atomization processes. A liquid column is shown to react very strongly to perturbations at its lowest-order natural frequency $\omega = \sqrt{(6\sigma)/((\rho + \rho_g)a^3)}$,

but has minimal unsteady response for frequencies not near this value. Early (unstable) fuel injector designs used in the F-1 engine program were shown to be near this natural frequency. In addition, nonlinear natural frequencies for columns under finite deformation have been quantified. The frequency shift associated with a finite amplitude deformation is shown to cause a limiting amplitude of column distortion.

The response of a liquid jet to longitudinal excitation (as modeled through the use of a dynamic orifice massflow) has also been quantified. Periodic bulges in the jet's surface, typically referred to as the "Klystron effect", are described quantitatively using this model. For low speed jets, increasing both amplitude and frequency of the disturbance is shown to increase the size of "satellite" drops formed by nonlinear deformation of the column. At large excitation amplitude, distinct "mushroom-shaped" structures appear, as described by several researchers. It is obvious that the formation of these structures will decrease mean drop size, but more effort is required to quantify the extent of the size change.

Acknowledgement

References

1. Harrje, D. T. and Reardon, F. H., ed., *Liquid Propellant Rocket Combustion Instability*, NASA SP-194, 1972.

2. Jensen, R., (Ed.), "JANNAF Subcommittee on Combustion Stability - Annual Report," 27th JANNAF Combustion Meeting, Cheyenne, Wyoming, 1990.

3. Huynh, C., Ghafourian, A., Mahalingam, S., and Daily, J. W., "Combustion Design for Atomization Study in Liquid Rocket Engine," AIAA 92-0465, 1992.

4. Miesse, C. C., "The Effect of Ambient Pressure Oscillations on the Disintegration and Dispersion of a Liquid Jet," *Jet Propulsion*, October 1955, pp. 525-534.

5. Miesse, C. C., "Correlation of Experimental Data on the Disintegration of Liquid Jets," *Industrial and Engineering Chemistry*, Vol. 47, No. 9,1955, pp. 1690-1701.

6. Reba, I. and Brosilow, C., "Combustion Instability: Liquid Stream and Droplet Behavior," WADC TR 59-720, 1960.

7. Torda, T. P. and Schmidt, L. A., "One Dimensional Unsteady Aerothermo-chemical Analysis of Combustion Instability in Liquid Rocket Engines," *Pyrodynamics*, Vol. 1, 1964, pp. 89-111.

8. Dunne, B. and Cassen, B., "Velocity Discontinuity Instability of a Liquid Jet," *Journal of Applied Physics*, Vol. 27, No. 6, 1956, pp. 577-582.

9. Ingebo, R. D., "Atomization of Ethanol Jets in a Combustor with Oscillatory Combustion-Gas Flow," NASA TN D-3513, 1966.

10. Dressler, J. L., "Characterization of a Velocity-Modulation Atomizer", *Review of Scientific Instruments*, Vol. 65, pp. 3563-3569, 1994.

11. Orme, M., "On the Genesis of Droplet Stream Microspeed Dispersions", *Physics of Fluids*, V3, pp. 2936-2947, 1991.

12. Heidmann, M. F., "Oxygen-Jet Behavior During Combustion Instability in a Two-Dimensional Combustor," NASA TN D-2725, 1965.

13. Buffum, F. G. and Williams, F. A., "The Response of a Turbulent Jet to Transverse Acoustic Fields," *Proceedings of the 1967 Heat Transfer and Fluid Mechanics Institute*, 1967, pp. 247-276.

14. Hoover, D. V., Ryan, H. M., Pal, S., Merkle, C. L., Jacobs, H. R., and Santoro, R. J., "Pressure Oscillation Effects on Jet Breakup," *Heat and Mass Transfer in Spray Systems*, HTD-Vol. 187, ASME, 1991, pp. 27-36.

15. Hilbing, J. H., Heister, S. D., and Spangler, C. A., "A Boundary Element Method for Atomization of a Finite Liquid Jet", *Atomization and Sprays*, V 5, No. 6, pp 621-638, 1995.

16. Spangler, C. A., Hilbing, J. H., and Heister, S. D., "Nonlinear Modeling of Jet Atomization in the Wind-Induced Regime", *Physics of Fluids*, V 7, No. 5, pp 964-971, 1995.

17. Lamb, H. *Hydrodynamics, 6th Ed.*, Dover Publications, 1982.

18. Sterling, A. M. and Sleicher, C. A., "The Instability of Capillary Jets," *Journal of Fluid Mechanics*, Vol. 68, Pt. 3, 1975, pp. 477-495.

19. Oefelein, J. C. and Yang, V., "Comprehensive Review of Liquid-Propellant Combustion Instabilities in F-1 Engines," *Journal of Propulsion and Power*, Vol. 9, No. 5, 1993, pp. 657-677.

20. Rutz, M. W., "Effect of Transverse Acoustic Oscillations on Behavior of a Liquid Jet", M.S. Thesis, Purdue University, School of Aeronautics and Astronautics, 1995.

21. Rutland, D. F., and Jameson, G. J., "A Non-Linear Effect in the Capillary Instability of Liquid Jets", *Journal of Fluid Mechanics*, V46 part 2, pp. 267-271, 1971.

22. Lafrance, P., "Nonlinear Breakup of a Laminar Liquid Jet", *The Physics of Fluids*, V18 N4, pp. 428-432, 1975.

23. Dressler, J.L., "Two Dimensional, High Flow, Precisely Controlled Monodisperse Drop Source", WL-TR-93-2049, Wright Laboratory, Wright Patterson AFB, 1993.
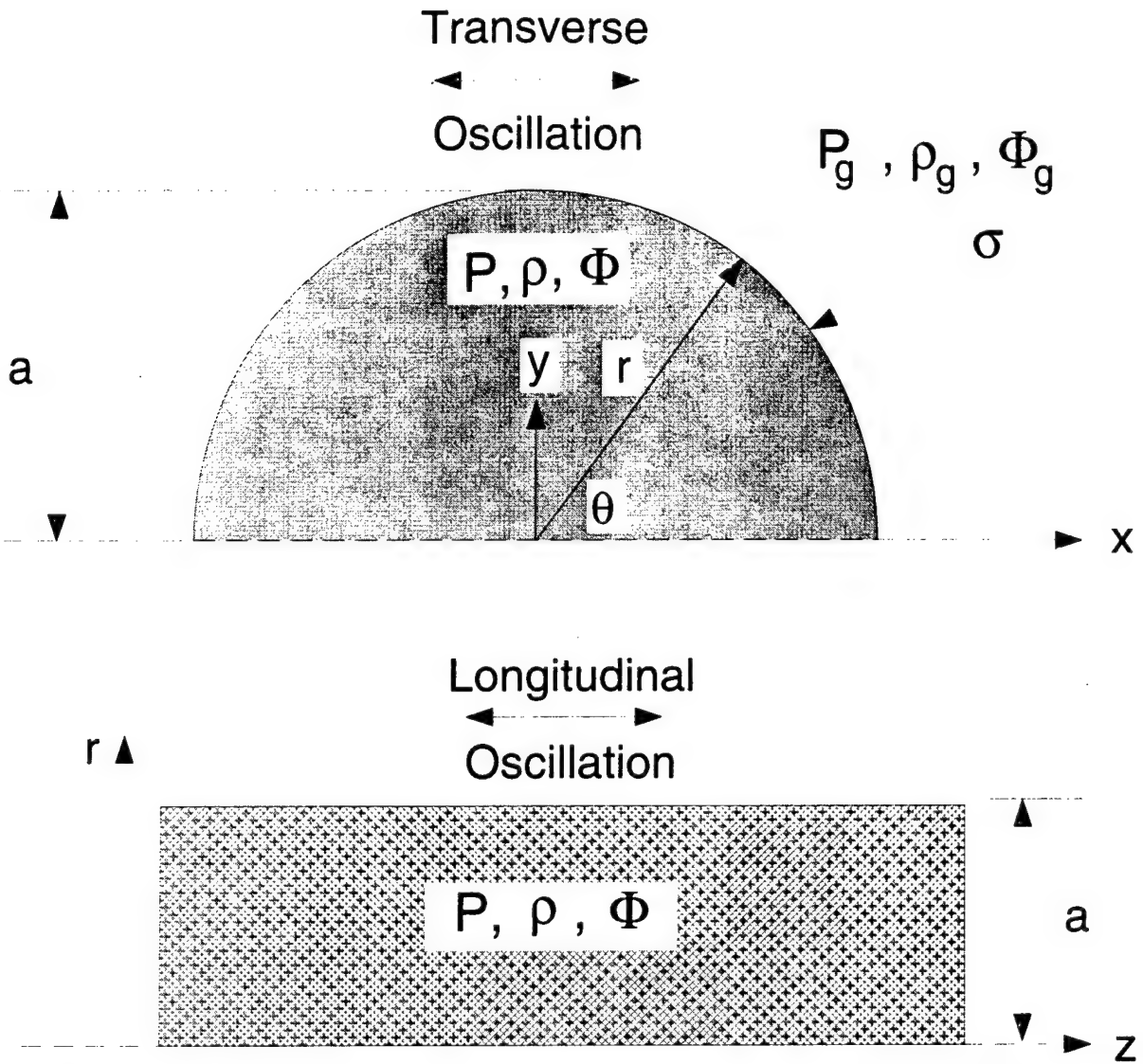
Figure Captions

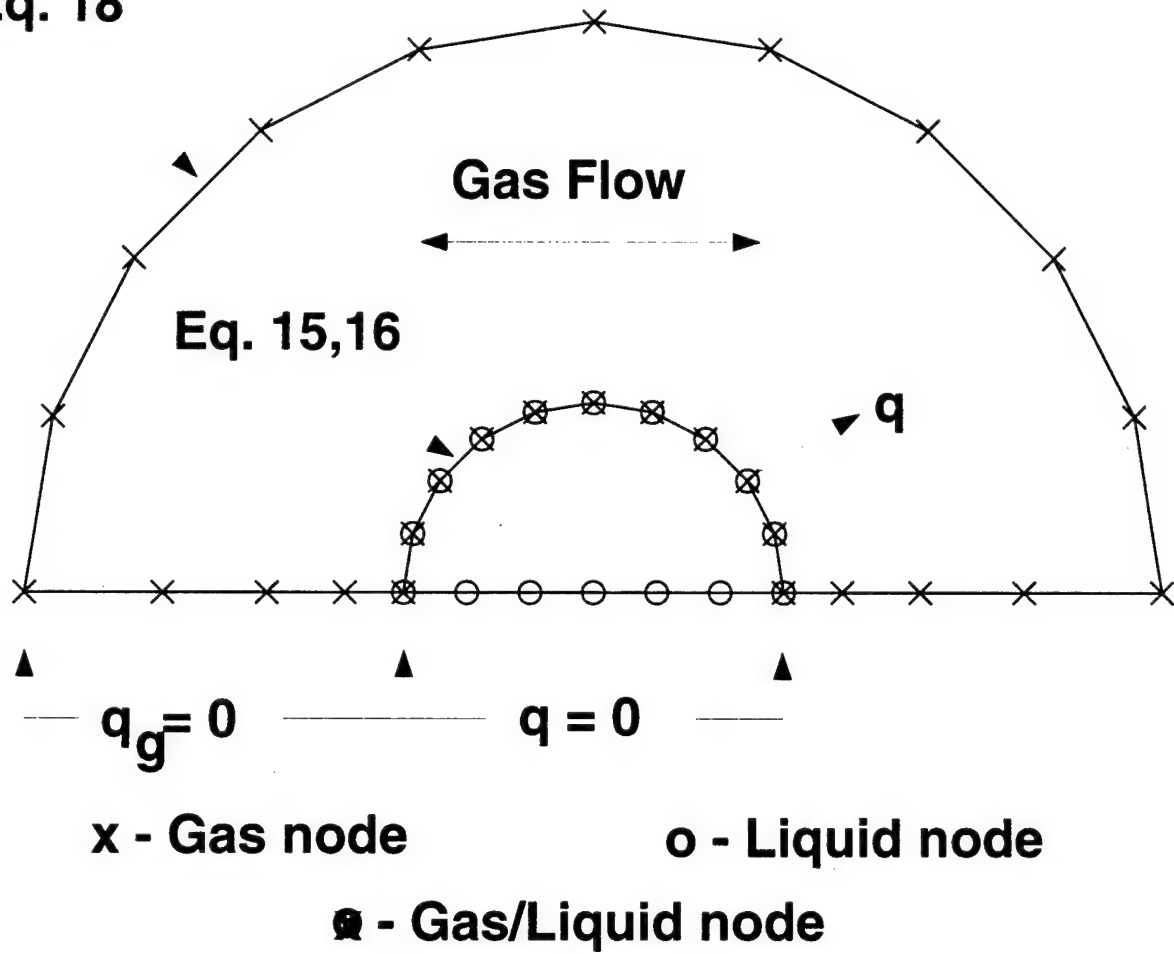1. Liquid Jets Subjected to Transverse and Longitudinal Acoustic Oscillations

2. Computational Domain and Boundary Conditions for Transverse Mode Simulations
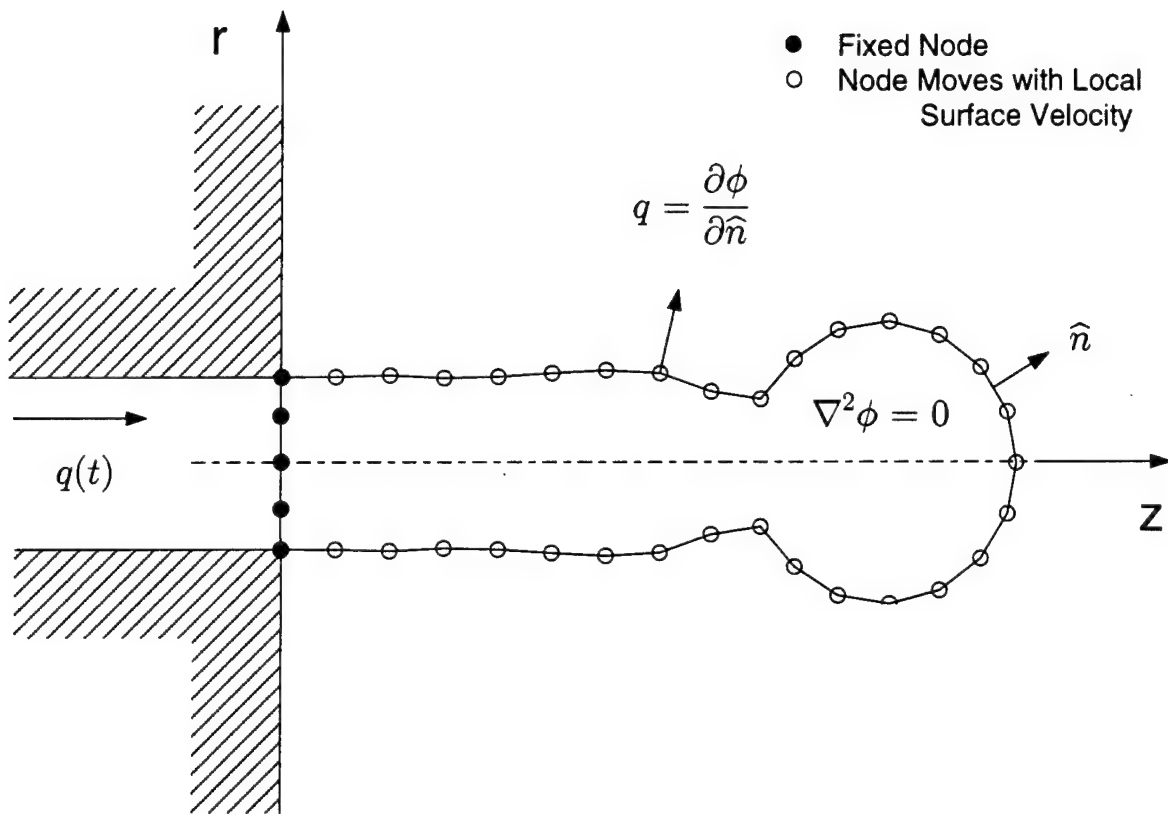
3. Computational Domain and Boundary Conditions for Longitudinal Mode Simulations

4. Column Shapes at Various Times of an Acoustic Perturbation, $\omega_g = \omega$, $We = 0.1$, $\epsilon = 0.01$

5. Motion of a Node on the Top of the Column During Acoustic Perturbation, $\omega_g = \omega$, $We = 0.1$, $\epsilon = 0.01$

6. Nonlinear Frequency Shift for Liquid Drops and Columns under Vaccuum (or Low Gas Density) Conditions

7. Nonlinear Frequency Response of Liquid Column; Maximum (Prolate) and Minimum (Oblate) Aspect Ratios Obtained During Oscillation

8. Effect of Longitudinal Disturbance Amplitude on Behavior of Liquid Jet at $We = 100$, $\omega_g = \omega = 0.7$. (a) $q' = 2\%$, (b) $q' = 4\%$, (c) $q' = 6\%$

9. Effect of Longitudinal Disturbance Amplitude on Drop Size for $We = 100$, $\omega_g = \omega = 0.7$. Solid Lines are for Infinitessimal ($q' \approx 0$) Disturbance.

10. Effect of Longitudinal Disturbance Frequency on Behavior of Liquid Jet at $We = 100$, $q' = 2\%$. (a) $\omega/\omega_g = 0.71$, (b) $\omega/\omega_g = 1.0$, (c) $\omega/\omega_g = 1.29$, (d) $\omega/\omega_g = 1.57$

11. Effect of Longitudinal Disturbance Frequency on Drop Size for Liquid Jet at $We = 100$, $q' = 2\%$. Solid Lines are for $q' \approx 0$.

12. Jet Behavior Under Violent Oscillation, $We = 1000$, $k = 1$, $q' = 10\%$.

Figure 1: Liquid Jets Subjected to Transverse and Longitudinal Acoustic Oscillations

Figure 2: Computational Domain and Boundary Conditions for Transverse Mode Simulations

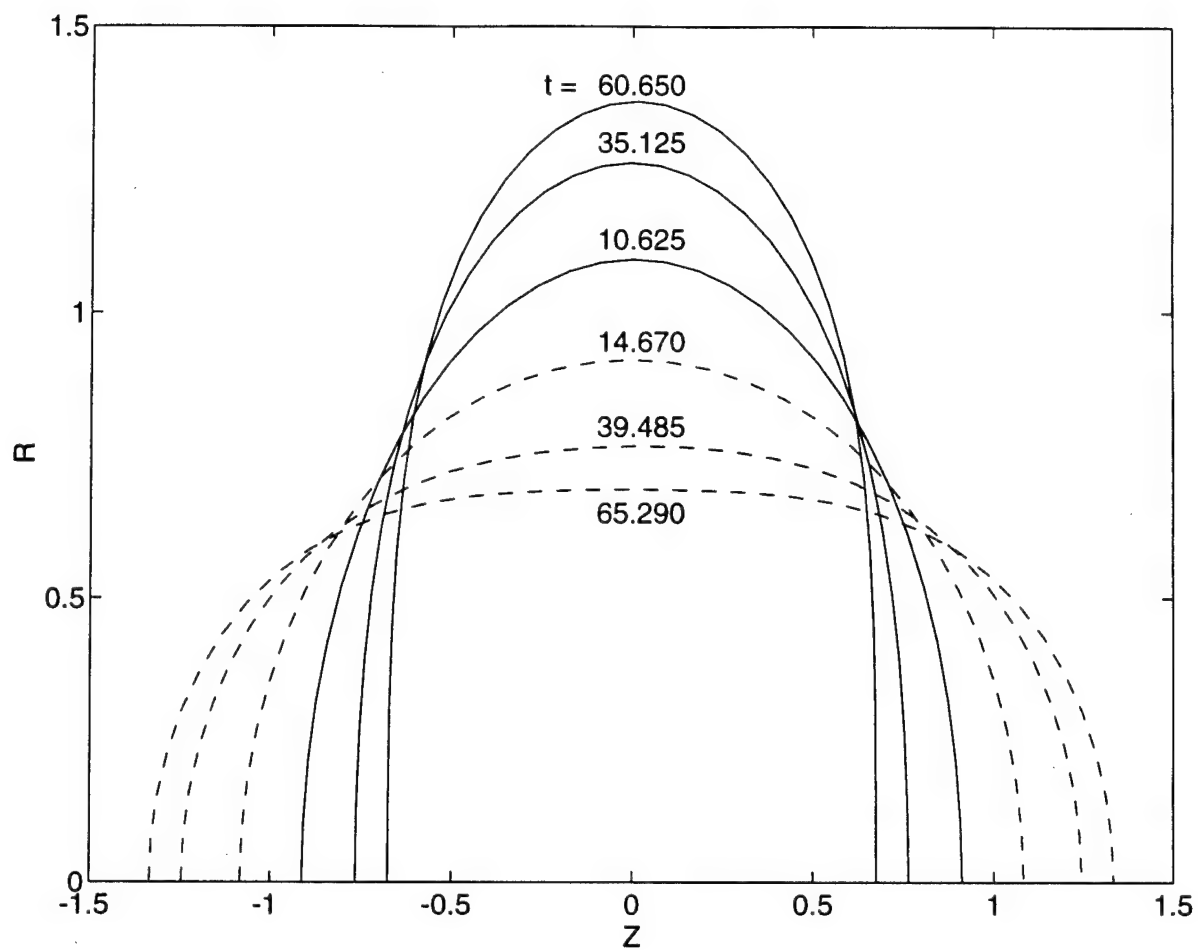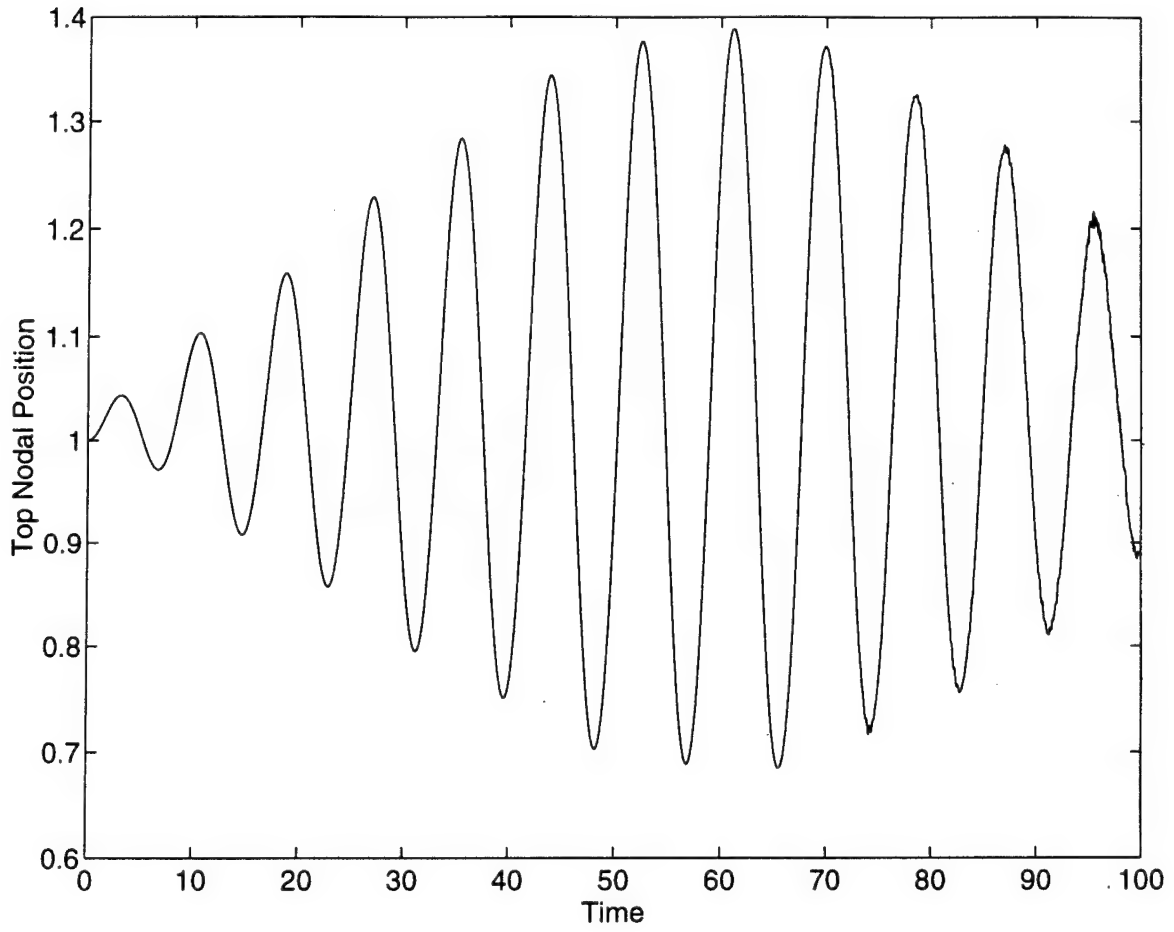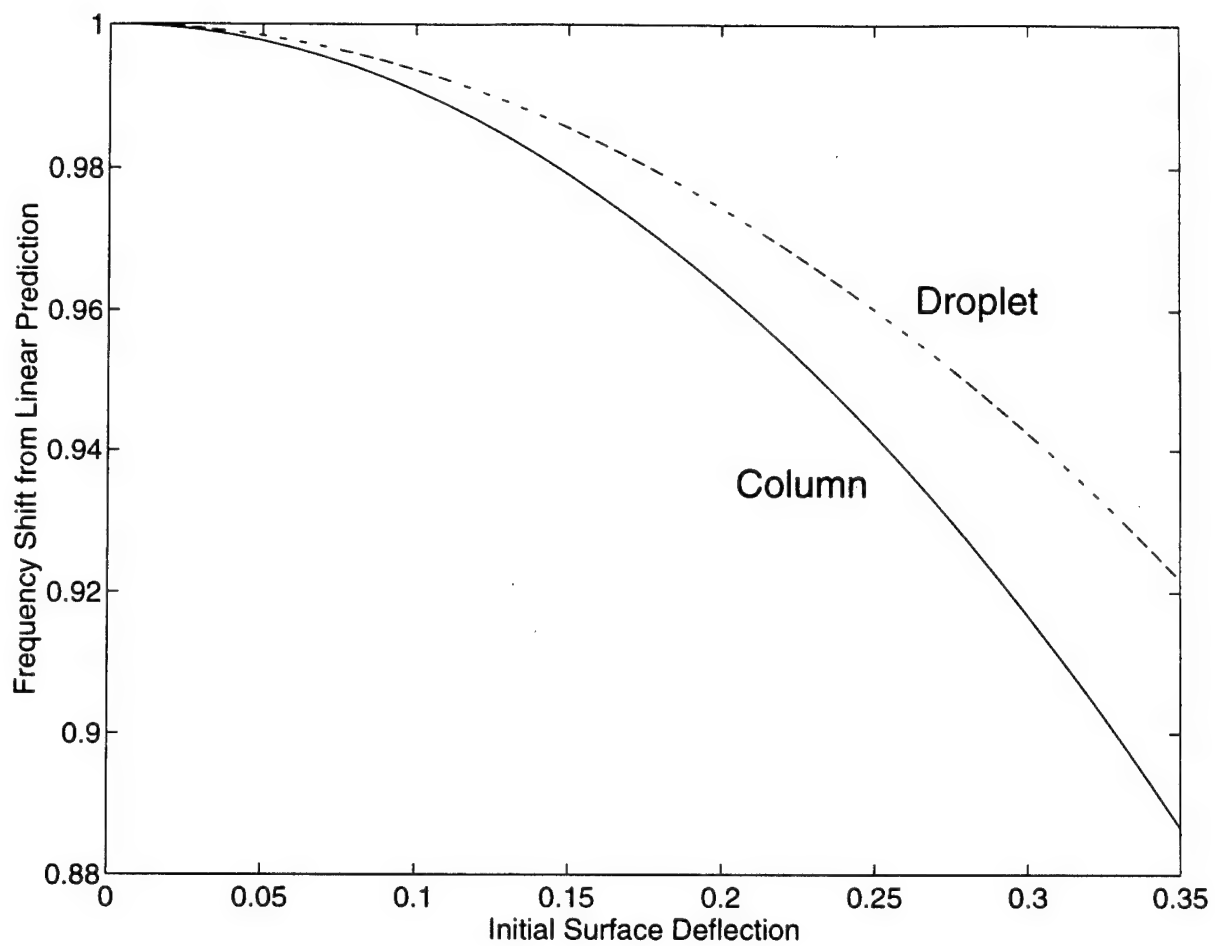Figure 3: Computational Domain and Boundary Conditions for Longitudinal Mode Simulations

Figure 4: Column Shapes at Various Times of an Acoustic Perturbation, $\omega_g = \omega$, $We = 0.1$, $\epsilon = 0.01$

Figure 5: Motion of a Node on the Top of the Column During Acoustic Perturbation, $\omega_g = \omega$, $We = 0.1$, $\epsilon = 0.01$

Figure 6: Nonlinear Frequency Shift for Liquid Drops and Columns under Vaccuum (or Low Gas Density) Conditions
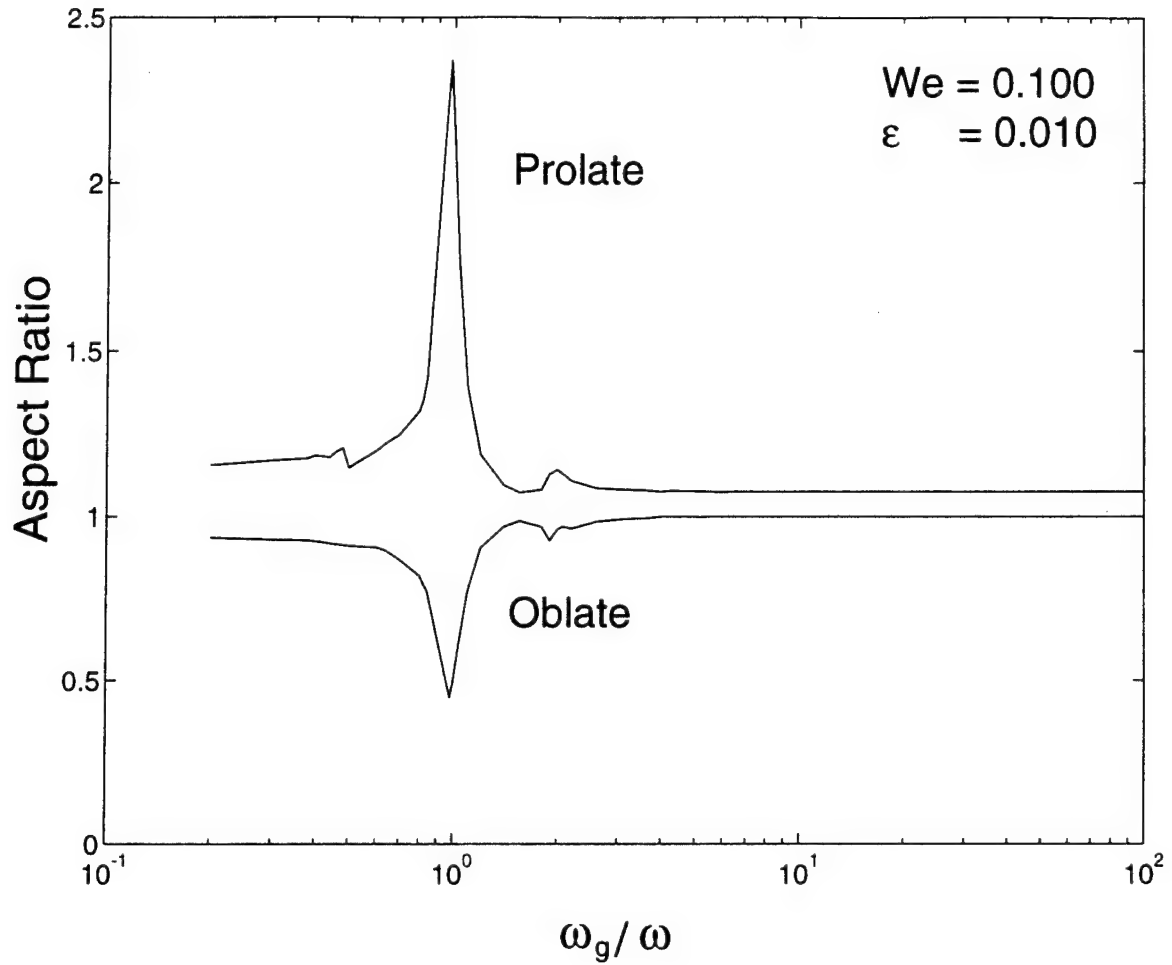
Figure 7: Nonlinear Frequency Response of Liquid Column; Maximum (Prolate) and Minimum (Oblate) Aspect Ratios Obtained During Oscillation
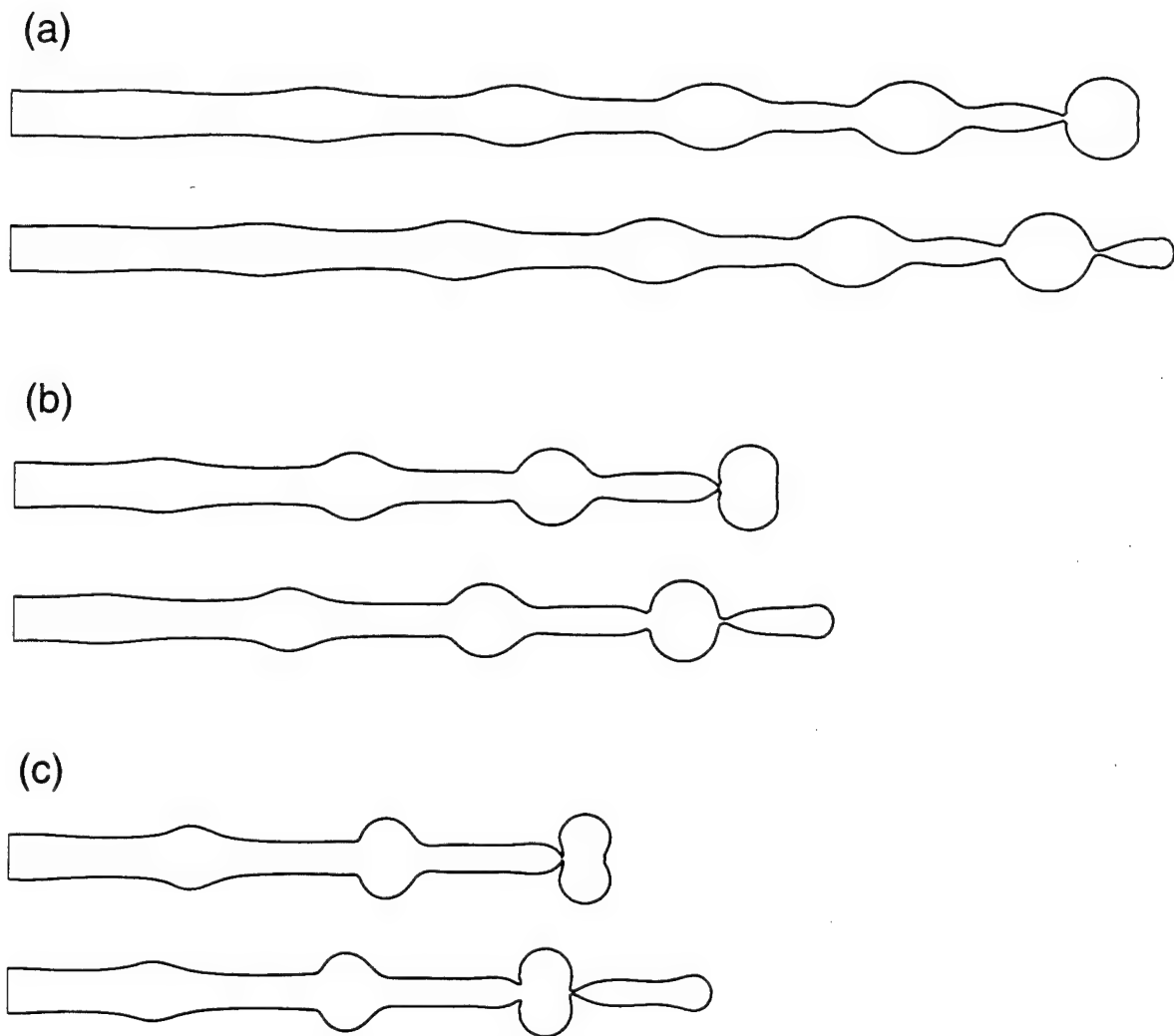
Figure 8: Effect of Longitudinal Disturbance Amplitude on Behavior of Liquid Jet at $We = 100$, $\omega_g = \omega = 0.7$. (a) $q' = 2\%$, (b) $q' = 4\%$, (c) $q' = 6\%$
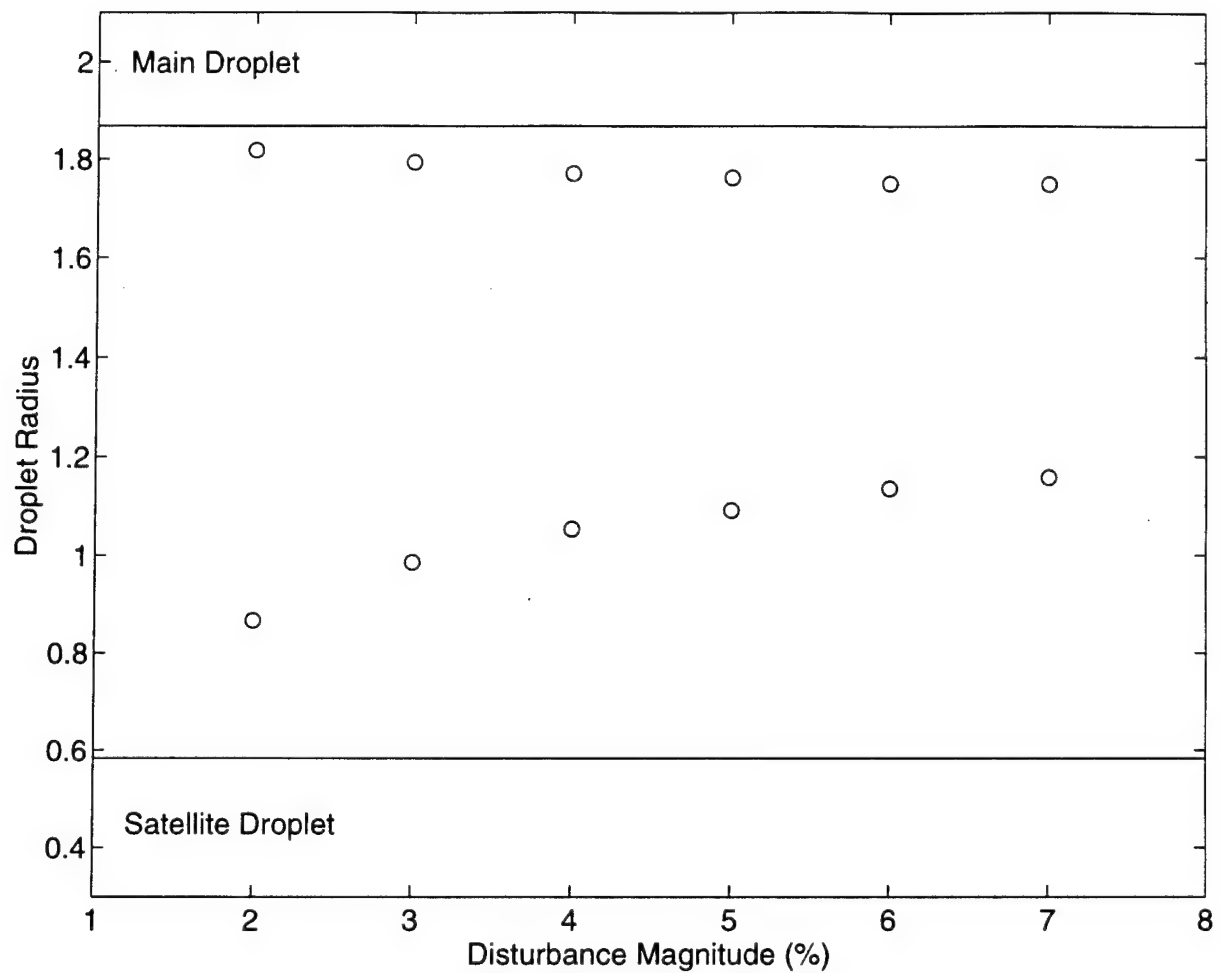
Figure 9: Effect of Longitudinal Disturbance Amplitude on Drop Size for $We = 100$, $\omega_g = \omega = 0.7$. Solid Lines are for Infinitessimal ($q' \approx 0$) Disturbance.
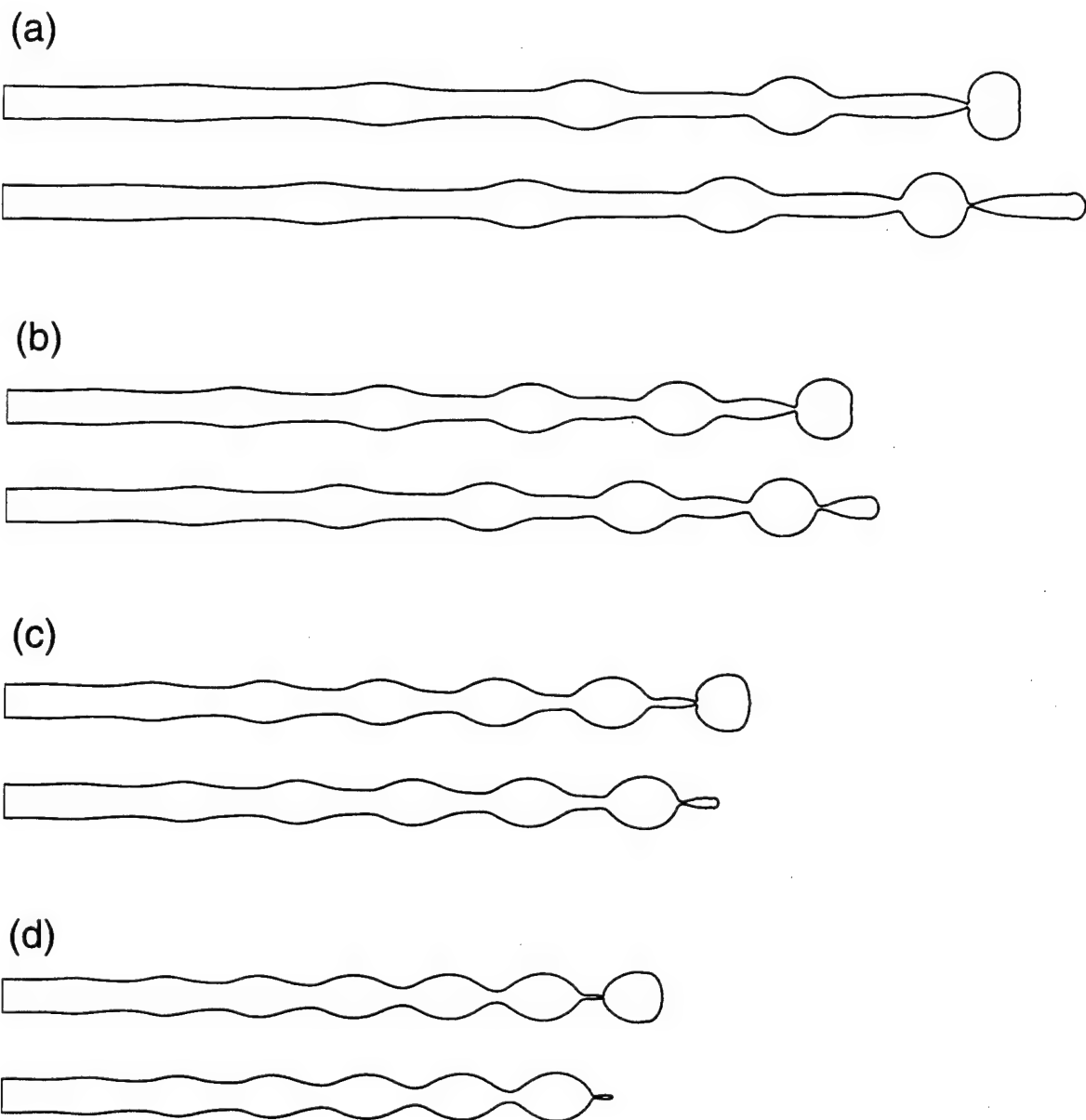
Figure 10: Effect of Longitudinal Disturbance Frequency on Behavior of Liquid Jet at $We = 100$, $q' = 2\%$. (a) $\omega/\omega_g = 0.71$, (b) $\omega/\omega_g = 1.0$, (c) $\omega/\omega_g = 1.29$, (d) $\omega/\omega_g = 1.57$
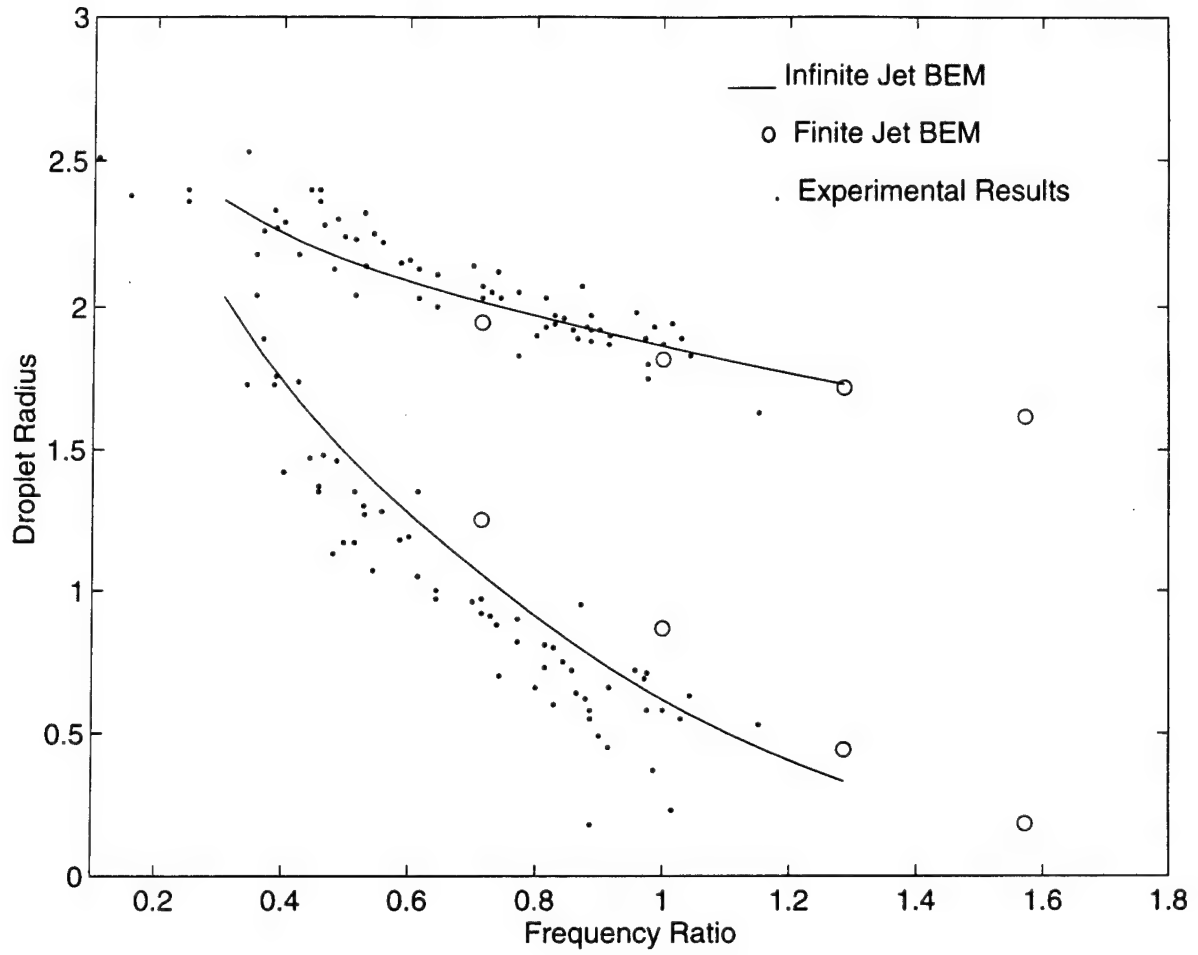
Figure 11: Effect of Longitudinal Disturbance Frequency on Drop Size for Liquid Jet at $We = 100$, $q' = 2\%$. Solid Lines are for $q' \approx 0$.
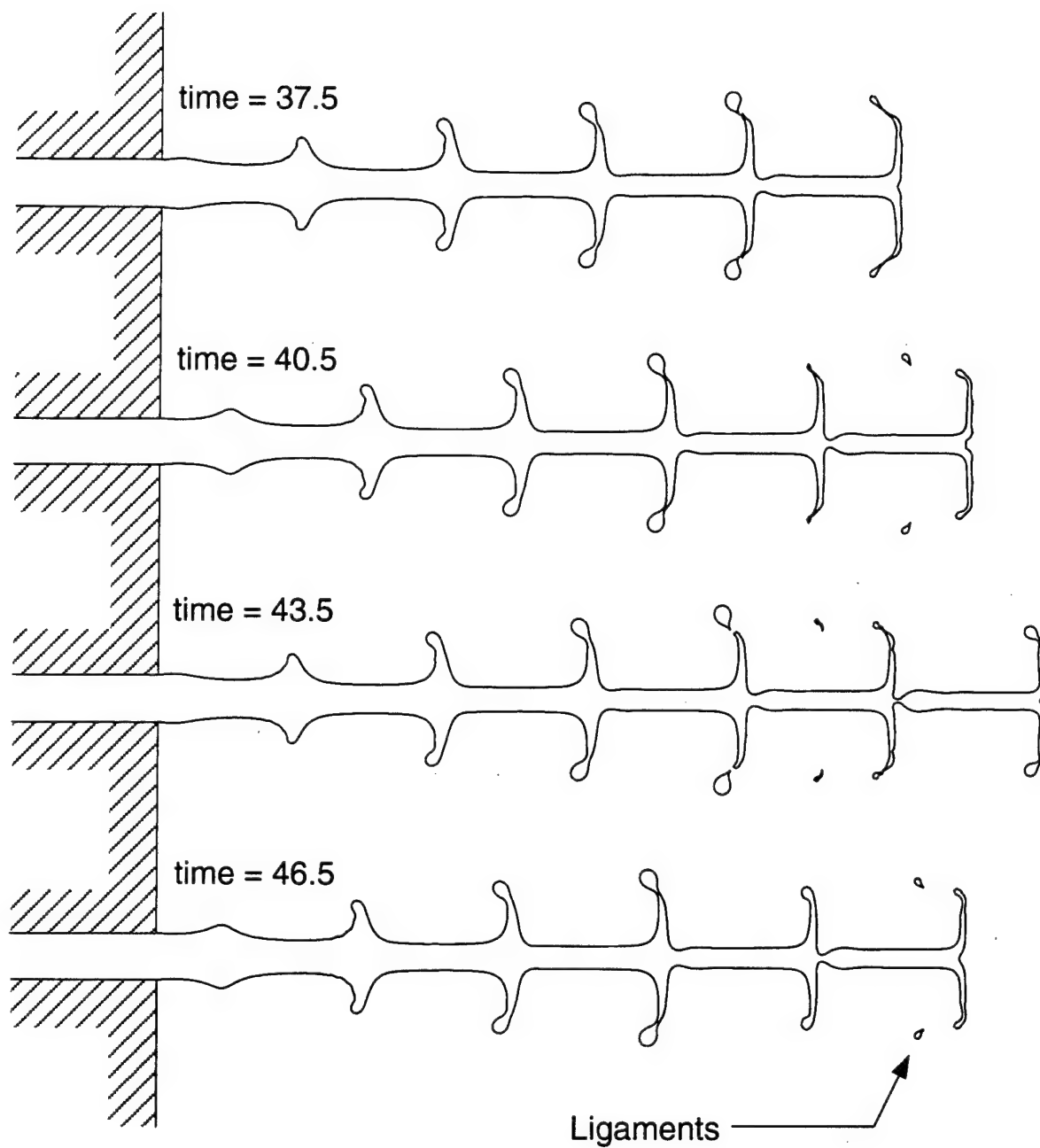
time = 37.5

time = 40.5

time = 43.5

time = 46.5

Ligaments

Figure 12: Jet Behavior Under Violent Oscillation, $We = 1000$, $k = 1$, $q' = 10\%$.

9 Appendix D - Acoustic Interaction with a Droplet

Murray, I. F., and Heister, S. D., "On the Response of a Droplet to Acoustic Excitation", In Review, *International Journal of Multiphase Flow*, 1996.

On a Droplet's Response to Acoustic Excitation

I. F. Murray*, **S. D. Heister**[†]

*Graduate Research Assistant

[†] Associate Professor, School of Aeronautics and Astronautics, Purdue University, W. Lafayette, IN, 47907

Abstract-The unsteady, nonlinear response of a liquid droplet to an imposed acoustic perturbation has been simulated using a model based on Boundary Element Methods (BEMs). The model was used to study the influence of the acoustic frequency, intensity, and gas/liquid density ratio upon the droplet behavior. Heightened droplet responses were observed for frequencies near the harmonics of the second and fourth mode frequencies. Several types of droplet atomization have been observed as the acoustic intensity is increased. Increasing gas density (at fixed excitation conditions) also heightens droplet response.

Key Words: drop break up, atomization, drop dynamics, acoustics, drop oscillations

1   Introduction

The behavior of liquid droplets in the presence of an acoustic field is a phenomena of fundamental importance. There are a variety of applications in which droplets are excited by acoustic energy, such as meteorological physics, containerless processing, and atomization. Droplet oscillations in the absence of external excitation will ultimately dissipate, and the drop will return to its equilibrium state. However, a strong acoustic field may be present, such is the case in airborne combustors and acoustic levitators. In such a situation, the droplet will experience forced oscillations. This oscillatory behavior of drops may greatly affect the process of secondary atomization.

A large number of researchers have studied "free oscillations" of droplets under conditions where forces from the gaseous phase are neglected. The initial linear analyses of this problem are due to Rayleigh (1879) and Lamb (1932) for the inviscid and weak-viscous cases. These results provide the droplet's frequency of oscillation under various modes under the presumption that the shape perturbation is infinitessimal. Lamb's result indicates that weak viscous effects have a negligible effect on the frequency predicted by Rayleigh. Prosperetti (1980) furthered the linear analysis for arbitrary viscous effects. Despite his improvements to the linear analysis, there was considerable disparity between his predicted decay rate of oscillations and the experimentally observed rate.

More recently, theoretical/numerical efforts have focused on nonlinear effects. Tsamopoulos and Brown (1983) developed a theoretical series solution for moderate amplitude, inviscid droplet oscillations. They determined that the droplet resonant frequency decreases with the square of the oscillation amplitude. Lundgren and Mansour (1988) used a boundary integral method to develop a model for large amplitude oscillations of droplets in zero-gravity including weak viscous effects. They discovered that relatively small viscosities can significantly affect the coupling of oscillatory modes. However, their method was limited to only weak viscous problems. More recently, Basaran (1991) used the Galerkin/finite element technique to model nonlinear oscillations of viscous droplets. From these simulations he observed that a finite viscosity has a much larger effect on mode coupling than what is predicted by the calculations including weak viscous effects.

Some notable experimental work in droplet oscillations has been conducted by Trinh and Wang (1981), in which large amplitude, nonlinear oscillations of drops were studied. In their work, a neutrally-buoyant droplet was suspended in an immiscible liquid and excited by acoustic-radiation pressure forces generated by an acoustic levitator. More recently, Wang, Anilkumar, and Lee (1996) studied the oscillations of low-viscosity drops in a microgravity environment on board the space shuttle using a similar acoustic chamber to induce droplet deformation. In these experiments, droplets were deformed and then allowed to oscillate freely. From a controlled break up of a liquid jet, Becker, Hiller, and Kowalewski (1990) generated virtually monodispersed droplets that oscillated in a damped, axisymmetric fashion. These experiments verified the reduction in natural frequency at finite amplitudes as predicted by Tsamopolous and Brown.

Despite these advancements in the area of free-oscillations of droplets, there have been relatively few works aimed at increasing the understanding of droplet response to forced oscillations. Here, the experimental work of Daidzic (1995) is a notable exception. Using an acoustic levitator, Daidzic examined nonlinear forced oscillations of droplets. In his experiments the droplets exhibited "chaotic behavior", presumably because

the forcing function was three-dimensional and time-dependent. He concluded that prediction of droplet behavior over a long period of time is difficult at best, and warrants further investigation.

The works of the aforementioned researchers have considerably improved the understanding of droplet behavior. However, the forced oscillation problem still warrants additional consideration. The focus of this work is to examine forced, nonlinear, inviscid droplet oscillations by computational analysis. The Boundary Element Method (BEM) will be used to conduct these studies. This technique offers a savings in computational power as compared to other methods, such as computational fluid dynamics, while maintaining a high degree of accuracy. As the name implies, BEMs require the discretization of only the boundary of the domain, providing a drastic reduction in the total number of nodes (as compared to a mesh based schemes) needed for an accurate solution. Hilbing, Heister, and Spangler (1995) and Mansour and Lundgren (1990) have also demonstrated a capability of running BEM simulations beyond atomization events. The following sections of this paper describe the development, validation, and results generated using this computational tool.

2   Model Development

Under many situations, the wavelength of the acoustic perturbation is much greater than the droplet radius, which implies that spatial variations within the acoustic wave are negligible and that the disturbance can be modeled as an unsteady, incompressible flow. Further, we assume an axisymmetric domain and neglect viscosity in both gas and liquid phases. Under these conditions, the dynamics of both liquid and gas phases are described by Laplace's equation:

$$\nabla^2 \phi = \nabla^2 \phi_g = 0 \tag{1}$$

where ϕ and ϕ_g are velocity potentials for liquid and gaseous phases, respectively.

If we choose the droplet radius (a), peak speed in the acoustic disturbance (U), and liquid density (ρ) as dimensions, the interaction between the droplet and the acoustic disturbance is characterized by the gas/liquid density ratio,

$$\epsilon = \frac{\rho_g}{\rho} \tag{2}$$

the Weber number based on gas density,

$$\mathrm{We} = \frac{\rho_g U^2 a}{\sigma} \tag{3}$$

and the frequency ratio,

$$\frac{\omega}{\omega_n} \tag{4}$$

Changes in the magnitude of the acoustic disturbance are introduced through the Weber number, which is the ratio of the aerodynamic forces to surface tension (σ) forces. The frequency ratio is the ratio of the acoustic frequency of the gas, ω, to the linear natural frequency of the second mode for a liquid drop, ω_n. In the following development, we presume that the nondimensionalization described above has been applied.

The droplet's fundamental frequencies are obtained from the classic analysis by Lamb. The nondimensional form for the frequency of mode "m" is:

$$\omega_m^2 = \frac{m(m+1)(m-1)(m+2)}{(m+1+m\epsilon)\mathrm{We}} \tag{5}$$

For this case, the lowest-order $(m = 2)$, or natural frequency of a droplet reduces to:

$$\omega_2^2 = \frac{24\epsilon}{(3+2\epsilon)\mathrm{We}} \tag{6}$$

We expect strong droplet response when the acoustic excitation frequency ω lies near harmonics of ω_n.

At any instant in time, Eqn. 1 provides a connection between values of the velocity potentials and velocities measured normal to the local surface $(q$ and $q_g)$ for liquid and gaseous phases, respectively. This

equation is solved using the BEM by beginning with its integral representation. For the liquid phase, the resulting integral representation of Eqn. 1 becomes:

$$\alpha\phi(\vec{r_i}) + \int_\Gamma \left[\phi \frac{\partial G}{\partial \hat{n}} - qG \right] d\Gamma = 0 \tag{7}$$

where $\phi(\vec{r_i})$ is the velocity potential at a point $\vec{r_i}$. Γ is the boundary of the domain, and G denotes the free space Green's function corresponding to Laplace's equation. In addition, $\hat{n}$ is taken to be the outward normal to the domain boundary, and α results from singularities introduced as the integration passes over the boundary point, $\vec{r_i}$. By using Eqn. 7, it is possible to solve for ϕ or q provided that one of them is known at each point on the boundary. If we let r and z represent radial and axial coordinates and use the subscript i to denote the "base point" where the integration takes place, the free space Green's function for the axisymmetric Laplacian can be expressed (Liggett and Liu 1983):

$$G = \frac{4rK(p)}{\sqrt{(r + r_i)^2 + (z - z_i)^2}} \tag{8}$$

where

$$p = \frac{(r - r_i)^2 + (z - z_i)^2}{(r + r_i)^2 + (z - z_i)^2} \tag{9}$$

and, $K(p)$ is the complete elliptic integral of the first kind. For computational efficiency, this parameter is curvefit (to an accuracy of 10^{-8}) using results from Abramowitz and Stegun (1970).

The integration in Eqn. 7 is performed by discretizing the boundary into a finite number of segments. Along each segment, both ϕ and q are assumed to vary linearly. Integrations are carried out by letting each node on the boundary represent a base point, yielding a set of linear equations relating ϕ and q involving all boundary nodes. The fully-populated matrices used to store coefficients of these equations are inverted using the Crout Method LU Decomposition from Numerical Recipes in Fortran (Beyer 1991). Additional details regarding the BEM solution procedure are provided in Hilbing, Heister, and Spangler (1995).

2.1   Free Surface Treatment

A procedure similar to that of Longuet-Higgins and Cokelet (1976) is used to update the position of nodes on the interface. Free surface nodes are "tracked" along lines parallel with the local velocity vector *in the liquid*. Under this assumption, flow kinematics require:

$$\frac{Dr}{Dt} = \frac{\partial \phi}{\partial r} \qquad\qquad \frac{Dz}{Dt} = \frac{\partial \phi}{\partial z} \tag{10}$$

The velocities calculated by solving Laplace's equation are normal and tangential to the surface. While the normal velocity is generated via the solution of Laplace's equation, the tangential velocity $(\partial\phi/\partial s)$ is calculated using a 4th-order (five point) centered difference method. Radial and axial velocities required in Eqn. 10 are determined via the coordinate transformation:

$$\frac{\partial \phi}{\partial r} = \frac{\partial \phi}{\partial s} \sin \beta + q \cos \beta \tag{11}$$

and

$$\frac{\partial \phi}{\partial z} = \frac{\partial \phi}{\partial s} \cos \beta - q \sin \beta \tag{12}$$

where β is the local wave slope.

The unsteady Bernoulli equation provides the dynamic boundary condition for nodes on the interface. In an Eulerian system where time derivatives are assumed to occur at a fixed spatial location, the dimensionless form of this relation valid in the liquid domain is:

$$\frac{\partial \phi}{\partial t} + \frac{1}{2}(\nabla \phi)^2 + P_g + \frac{\kappa \epsilon}{\mathrm{We}} = 0 \tag{13}$$

and the gas domain analog is:

$$\epsilon \frac{\partial \phi_g}{\partial t} + \frac{\epsilon}{2}(\nabla \phi_g)^2 + P_g = 0 \tag{14}$$

61

Since the nodes on the interface are assumed to travel with the local liquid surface velocity, a transformation from the Eulerian to Lagrangian reference frame is required. Under this assumption, the following equation can be used to perform the Eulerian - Lagrangian transformation [23]:

$$\frac{D(\ )}{Dt} = \frac{\partial(\ )}{\partial t} + \nabla\phi \cdot \nabla(\ ) \tag{15}$$

By applying this transformation, the Bernoulli's equations (13,14) become:

$$\frac{D\phi}{Dt} = \frac{1}{2}\left(\nabla\phi\right)^2 - P_g - \frac{\kappa}{\text{We}} \tag{16}$$

$$P_g = -\frac{\epsilon}{2}(\nabla\phi_g)^2 - \epsilon\frac{D\phi_g}{Dt} + \epsilon\nabla\phi \cdot \nabla\phi_g \tag{17}$$

where $D(\ )/Dt$ denotes changes in time for nodes moving with the liquid interface velocity.

In the case of the liquid domain, the substantial derivative, $D\phi/Dt$, is calculated using Eqn. 16. A first order backward difference method was used to calculate the gas based substantial derivative appearing in Eqn. 17:

$$\frac{D\phi_g}{Dt} = \frac{\phi_g^{n+1} - \phi_g^n}{\Delta t} \tag{18}$$

where n indicates the time level.

A stable, time-accurate procedure has been developed to advance the solutions of (16, 17) for all free-surface nodes. The following steps are taken:

1. An initial value of ϕ and ϕ_g are given at each node on the interface.

2. Solution of Laplace's equation (described in previous section) provides the liquid domain velocities, q, at each node on the interface.

3. Set $q_g = -q$ since the gas nodes are fixed to move with the liquid nodes and the outward normals are in opposite directions.

4. Solve Laplace's equations for the gas domain to calculate ϕ_g at each node in the gas.

5. Calculate $D\phi_g/Dt$ using Eqn. 18.

6. Calculate the gas pressure distribution along the interface using Eqn. 17.

7. This value of gas pressure is used to solve for ϕ at the new time step via integration of Eqn 16.

8. The interface is "regridded" using cubic splines of r, z, P_g, and ϕ to preserve the even spacing between nodes (Hilbing et al. 1995).

9. Steps 2-4 are repeated with the "regridded" properties, in order to determine the boundary conditions at the next time step for the new grid.

A 4th-order Runge-Kutta scheme is employed in the time integrations. Using this scheme, it is necessary to solve the Laplace equation eight times, four for the liquid and four for the gas. However, at the end of each time step it is necessary to solve the Laplace equation for both domains again (due to the regridding), therefore Laplace's equation is solved a total of ten times per time step using this procedure.

2.2   Domain Discretization and Boundary Conditions

The computational domain and the boundary conditions used in this analysis are displayed in Figure 1. In this figure, ϕ and ϕ_g represent the velocity potentials in the liquid and gas domains respectively, and $q = \partial\phi/\partial\hat{n}$ stands for the velocity in the normal direction. The radial and axial directions are denoted by r and z. The flow is considered axisymmetric with respect to the z-direction, so that only a half section is needed for the model. However, another axis of symmetry exists along the radial axis due to the assumption of inviscid, incompressible flow. As a result, only a quarter section is required for this analysis. Nodes have been placed on the interface between the domains, along the radial axis in both domains, and the outer boundary of the gas. The gas nodes are denoted with a "x", while the liquid nodes are labeled with an "o".

62

Along the radial line of symmetry for both domains, $q = 0$ in the liquid and $\partial\phi_g/\partial r = 0$ in the gas. Equations 16 and 17 were used to set the boundary condition along the interface. Along the outer boundary of the gas domain, a sinusoidal velocity history is used to model the acoustic disturbance:

$$\phi_g = z_g \cos(\omega t) \tag{19}$$

Boundary conditions are not specified along the axis of axisymmetry, since the Green's functions vanish as $r \to 0$. For this reason, nodes are not required along this boundary.

3 Model Implementation and Validation

Once the model had been fully developed, its accuracy was checked by comparing its results to results from analytic and other numerical methods. Three separate validation cases were considered: steady flow over a sphere, non-linear oscillations of a liquid droplet, and droplet profiles for a steady crossflow.

The accuracy of the gas domain solution was tested by comparing the distribution of the velocity potential over a sphere with the analytic solution of the same problem. The analytic solution was compared to the numerical solutions for grids using, 45, 35, 25, and 15 nodes along the interface. The numerical results agree well with the analytic solution, and the magnitude of the error is well below 0.5% for all cases. For computational efficiency, it was decided to employ only 15 nodes to model the surface of the droplet. For cases when the drop becomes highly deformed, as many as 45 nodes were employed in order adequately resolve the surface.

As explained previously, an expression for the fundamental oscillatory mode was developed by Lamb using linear analysis. This analysis assumed a linearized surface shape of the form:

$$r = 1 + \eta \cos(n\theta) \, \sin(\omega_n t) \tag{20}$$

where η is the measure of the initial disturbance amplitude. Tsamopoulos and Brown (1983) later expanded upon this analysis by including second order effects. They observed that the frequency of oscillation decayed with the square of the initial deformation. The accuracy of the liquid domain solution was determined by making comparisons between the oscillatory frequencies from the numerical model and the results of Tsamopoulos and Brown. The numerical model was run for an array of initial surface distortions with 23 nodes along the boundary. Figure 2 shows the comparison of the results from the two models. Excellent agreement exists between the two results. It was concluded that the liquid domain solution is accurate.

The last section of the validation process was to check the accuracy of the model when there is a strong coupling effect between the gas and liquid domains. This was accomplished by comparing droplet profiles calculated by the numerical model and the profiles predicted by Miksis, Vanden-Broeck, and Keller (1981). They developed a model to predict the equilibrium shape of a droplet subjected to a uniform flow. The equilibrium drop profile was determined by balancing the pressure of the gas on the surface with the surface tension and internal pressure at the same point.

In order to achieve a steady state solution with the model, it was necessary to introduce a dissipative mechanism, which ultimately yielded a steady state solution. Numerical smoothing was applied to ϕ until surface velocities vanished. Figure 3 shows a comparison between the predicted profiles of the numerical model and the method used by Miksis et al. These comparisons clearly show excellent agreement between the two models. Hence, it was concluded that the coupled solution is accurate.

4 Results

The model was utilized to assess the influence of perturbation frequency (ω/ω_n), Weber number (We), and density ratio (ϵ) on the nonlinear response of a droplet to an imposed acoustic oscillation. The results presented here represent over 200 runs of the model. Calculations typically used 15 nodes along the interface, 15 along the radial axis in the gas, and 10 nodes along the outer boundary of the gas domain. However, larger grids (as many as 45 nodes along the interface) were utilized to resolve more complex droplet shapes, such as those in Figure 14 described below.

During these simulations, the level of the droplet response is characterized by two parameters, the aspect ratio and the oscillatory mode coefficients. The aspect ratio provides a gross measure of overall droplet

deformation and is defined as being the ratio of the major axis over the minor axis of the droplet at peak deformation. The mode coefficients, are determined by expressing the current droplet shape as a sum of Legendre Polynomials:

$$r = 1 + \sum_{m=1}^{\infty} C_m(t) \cos(m\theta) \tag{21}$$

where θ is the angle measured from the positive z axis and C_n are the time varying coefficients. Because Cosine functions are orthogonal, it is possible to calculate the coefficients using (Lundgren and Mansour 1988):

$$C_m = \frac{1}{\pi} \int_{-\pi}^{\pi} (r-1) \cos(m\theta) d\theta \tag{22}$$

Due to the fact that both incompressible and inviscid assumptions are employed in the gas phase, there is no mechanism to generate a surface pressure distribution which is asymmetric about the r axis in Fig. 1. For this reason, the model cannot excite odd modes of oscillation. This fact was verified by demonstrating that mode coefficients for the odd modes were all zero to within machine accuracy (10^{-14}).

4.1 Frequency Response Spectrum

The effect of the acoustic perturbation frequency was investigated by performing approximately 100 simulations. While the frequency was varied, the Weber number was held at 0.5779 and the density ratio was 0.00123. These conditions correspond to acoustic excitation of a 100 micron water droplet with a 160 db disturbance in ambient air. A time step of 0.05 seconds was employed for these computations. Results are displayed on Figure 4, which charts the aspect ratio for a range of frequency ratios. Readers are cautioned that the purpose of this investigation is to determine regions of high response; actual aspect ratios do depend on the assumed initial conditions (spherical vs. deformed drop, sine wave vs. cosine wave disturbance).

Figure 4 displays a series of peaks that occur near the harmonics of the natural frequency of the droplet. A noteworthy area is the break up region that exists for frequency ratios between 0.80 and 0.90. In this band, the disturbance is tuned to the natural frequency of the droplet to an extent such that atomization occurs. All peaks are shifted to frequencies slightly less than the linear result due to the nonlinear frequency shift as shown in Figure 2. The continual shifting of droplet natural frequency with deformation level leads to a bounded response over much of the frequency range (for this Weber number). In these regions, the acoustic perturbation continues to excite the droplet until the oscillations of the drop become out of phase with the disturbance, thereby tending to reduce the amplitude of the oscillation. This process repeats indefinitely or until the drop breaks up.

Areas of significant response occur for $\omega/\omega_n =$ near 0.5, 1.0, 2.0, 3.0, 4.0, and 6.0. The peaks near $\omega/\omega_n = 0.5$, 1.0, and 2.0 are primarily driven by second mode oscillations, while the peaks near $\omega/\omega_n = 3.0$, 4.0, and 6.0 contain significant fourth-mode effects. It is important to note that the fundamental frequency of the fourth mode is three times that of the fundamental frequency of the second mode, $\omega_4 = 3\omega_n$, for a drop in a low density gas ($\epsilon \ll 1$). It is worth mentioning that a frequency ratio near 5.0 does not produce a notable response.

For relatively low disturbance frequencies ($\omega << \omega_n$), a quasi steady-state response is observed whereby the droplet closely tracks the imposed perturbation with a very small phase lag. The amplitude (aspect ratio) in this region is greater than the response for higher off-harmonic frequency ratios due to the negligible phase lag in this region. At the other extreme ($\omega >> \omega_n$) the oscillations of the gas are so fast that the droplet is unable to respond appreciably to the changes in the gas flow. Here, the droplet responds to a mean dynamic pressure generated by the acoustic wave.

As the frequency ratio approaches a value of 0.5, the droplet begins to experience a sub-harmonic excitation. The frequency of its oscillation is 0.0604, which is approximately half of the natural frequency, 0.1304. The droplet behavior is characterized by a large deformation followed by a smaller one. The larger response is attributed to the peaks in the acoustic wave, whereas the secondary response is due to the droplet attempting to maintain its natural frequency. It has been observed that the second mode is solely responsible for the activity. There is a negligible amount of fourth mode activity, and the higher order modes are virtually non-existent (Murray 1996).

For frequency ratios near the drop natural frequency, the level of droplet activity is high, such is the case for $\omega/\omega_n = 0.79$. Figure 5 displays the radial position of the top node for this frequency ratio. As the

64

droplet begins to deform, it becomes increasingly excited as its natural frequency decreases and becomes in tune with the disturbance frequency. At this point the droplet repsonse peaks, and the natural frequency continues to decrease and becomes out of phase with the disturbance. The response begins to attenuate, which results in the natural frequency becoming in tune with the disturbance again. The period of this envelope of oscillations is 398 seconds (approximately 6 1/2 oscillations of the imposed gas disturbance). The droplet shapes at various times in this process are summarized in Figure 6. Here, T is the overall period associated with the process ($T = 398$) and the shapes are shown for various peaks and troughs in Fig. 5.

The activity of the droplet is initially controlled by second mode effects. The time history of the mode coefficients for the $\omega/\omega_n = 0.79$ case is shown in Figure 7. As the oscillatory amplitude increases, fourth mode coupling appears. As in all results investigated in this study, 6th, 8th, and higher even modes gave negligible contributions to the instantaneous droplet shapes. In conjunction with the nonlinear frequency shift, the fourth mode effects have a stabilizing influence upon the droplet. Figure 8 indicates that the second and fourth modes become coupled and destructively interfere, which causes the magnitude of the oscillations to dampen and the fourth mode effects to vanish. A similar envelope response is observed for the $\omega/\omega_n = 0.925$ case, however the interference that occurs is somewhat constructive, which serves to amplify the response.

For frequency ratios between 0.79 and 0.925, the second mode effects become overwhelming and the droplet breaks up. As the frequency ratio increases past 0.925, the droplet activity drops off since the excitation is above the resonant condition. A region of moderate droplet response lies in the frequency range of 1.2 to 1.4, which corresponds to the subharmonic of the fourth mode. Significant response is also noted at the second-harmonic of the fundamental mode, as one would expect.

For a frequency ratio near 3.0, the droplet experiences the third harmonic of the second mode of oscillation as well as the fundamental frequency of the fourth mode of oscillation. The time histories of the position of the top node and the mode coefficients are presented in Figures 9 and 10. The overall period for the process is over 2500 seconds, during which over 150 gas oscillations occur. Throughout this process, the magnitude of the second mode remains reasonably constant, whereas the fourth mode grows and decays over the period. Initially, the droplet oscillates in the second mode. As the fourth mode grows, it dominates the behavior of the droplet. The fourth mode then decays to roughly the same order of magnitude as the second mode. Similar behavior is observed for $\omega/\omega_n = 3.975$.

Probably the most surprising result from the frequency spectrum is that *more* response is noted near the second harmonic of the fourth mode ($\omega/\omega_n \approx 6$) than at the primary fourth mode excitation frequency. These two peaks were the subject of substantial scrutiny; model results were replicated for several different timesteps and mesh sizes. The top node position history for this case is shown in Figure 11. Here, the overall process takes about 780 dimensionless seconds, corresponding to about 95 periods of acoustic excitation. To seek an explanation for the heightened response (as compared to the $\omega/\omega_n = 2.97$ case), the second and fourth mode coefficients are compared in Figure 12. As seen in the upper plot, the second mode response is similar in both cases. However, the lower plot reveals a heightened fourth mode response near $t = 400$ for the $\omega/\omega_n = 5.89$ case. Apparently, there is a constructive nonlinear interaction in the $\omega/\omega_n = 5.89$ case leading to stronger fourth mode effects and increased overall excitation. Since viscous effects are more prevalent in damping higher modes, this curious response may not be replicated in actual experiments.

4.2   Effect of Acoustic Disturbance Intensity

The influence of the intensity of the acoustic wave was investigated by conducting a series of simulations at fixed density and frequency ratios, but with varying Weber number. For these simulations, the time step was set to be approximately 1/1000 of the period of a droplet oscillation for the $m = 2$ mode. Once again, the aspect ratio was used as an overall measure of droplet response; Figure 13 provides results for the case $\epsilon = 0.00123$, $\omega/\omega_n = 1.0$. During these simulations, it was observed that droplet atomization occurred at Weber numbers above 1.10. Here it is important to note that this "critical Weber number" is dependent on both density and frequency ratios; the 1.10 value is for harmonic excitation of a water droplet in air ($\epsilon = 0.00123$).

Droplet break up was studied by conducting trials using Weber numbers greater than the critical value. From this analysis, three regimes of break up were identified. Examples of these modes are shown in Figure 14. In the "nipple" breakup regime ($1.1 < We < 2.5$), two small satellite droplets are formed as a result of the nonlinear motion of the drop. Since the acoustic intensity is barely above the threshold value, breakup

in this region takes a substantial amount of time. The nipple regime is similar to the mode of break up experienced in the break up band of frequencies, as discussed in the beginning of Section 4.1. As Weber number is increased to 2.5, atomization occurs with the formation of two satellite droplets which are larger than the central drop. This "kidney" regime occurs The kidney regime exists for $2.5 < We < 3.0$. Kidney regime breakups are generated in 1-2 oscillations of the acoustic wave.

As the response amplifies, the drop flattens out in the direction perpendicular to the gas flow, and the center continues to flatten which results in the pushing out of a toroid of fluid. Break up occurs when the center of the drop pinches, and the cross-section resembles a torus. Atomization in this "toroidal" mode occurs in less than one acoustic period for $We \geq 3.0$. Here, the droplet rapidly flattens in a plane perpendicular to the acoustic wave. With increasing Weber number, the overall diameter of the droplet (at the atomization point) increases, while the inner diameter of the torus decreases as shown in Fig. 14. In this figure, the $We = 5.78$ case is at a reduced scale for display purposes. The droplet shapes at high We values are consistent with "aerodynamic shattering" which has been documented by observing the response of a droplet to a shock wave (see Hsiang and Faeth (1992) for background).

A summary of the breakup times (nondimensionalized by the period of the acoustic oscillation, τ) are provided in Figure 15. The curve is somewhat discontinuous in places due to the fact that breakups occur within discrete parts of a given cycle. Once again, for the conditions noted, no breakups occurred for $We < 1.1$.

4.3 Density Ratio Effects

The effect of the gas/liquid density ratio upon the droplet behavior was studied by varying this parameter while setting $We = 0.5779$ and $\omega/\omega_n = 1.0$. At a fixed Weber number, the gas-phase dynamic pressure can be thought to be fixed, so that an increase in density ratio under this constraint can be viewed as a decrease in density of the droplet. In effect, this approach holds the dynamic pressure constant, while decreasing the liquid inertia. The level of droplet response for a range of density ratios is shown in Figure 16. As expected, droplet response increases with density ratio. The results are somewhat discontinuous as droplet response enters the highly nonlinear region, primarily because inflections in the surface can start to occur in this area. For these flow conditions, droplets began to atomize for density ratios greater than 0.1.

5   Conclusions

The model presented in this paper has been used to study the nonlinear evolution of an acoustically excited droplet. While the maximum response of the droplet occurs at the harmonic condition ($\omega = \omega_n$), significant responses also occur for ω/ω_n near values of 0.5, 2, 3, 4, and 6. The actual peak responses are also slightly less than these values as a result of the reduction in the droplet's natural frequency at finite deformation amplitude (nonlinear frequency shift). Droplet responses for the frequency ratios near 0.5 and 2.0 are dominated by the second mode, whereas the coupling of the second and fourth modes are responsible for the responses to the frequency ratios near 3.0 and 4.0. The droplet response for $\omega/\omega_n \approx 6$, which represents the second harmonic of the fourth mode, is dominated by fourth mode activity and the amplitude of the response actually exceeds that of some of the lower-order harmonics.

As the magnitude of the acoustic disturbance increases, droplet atomization is predicted to occur. For harmonic forcing of a liquid droplet in air, a critical Weber number of 1.10 divides the oscillatory and atomization regimes. Droplet breakups occurred in "nipple", "kidney", and "toroidal" modes as Weber number was increased above this threshold value. Break up times were roughly inversely proportional to Weber number under these conditions. Finally, increasing gas/liquid density ratio under fixed Weber number and frequency ratio conditions was also shown to heighten droplet response.

Nomenclature

a = undisturbed droplet radius
G = free space Green's function

$\dot{n}$ = unit normal vector

P = pressure

q = velocity normal to local surface

t = time

U = maximum velocity in acoustic perturbation

We = Weber number, We= $\rho_g U^2 a/\sigma$

z = axial location

r = radial location

α = boundary point singularity contribution

β = surface slope

Γ = domain boundary

ϵ = ratio of gas to liquid density

κ = surface curvature

ρ = density

σ = surface tension

ϕ = velocity potential

ω_n = undisturbed droplet second mode natural frequency

ω = acoustic frequency (gas phase)

Subscripts

g = gas phase properties

References

1. Abramowitz, M. and Stegun, F. A., eds., *Handbook of Mathematical Functions.* Dover Publications, 9th ed., 1970.

2. Anderson, D. A., Tannehill, J. C., and Pletcher, R. H., *Computational Fluid Mechanics and Heat Transfer.* New York: Hemisphere Publishing Corporation, 1984.

3. Basaran, O., "Nonlinear Oscillations of Viscous Liquid Drops," *Journal of Fluid Mechanics*, Vol. 241, 1991. pp. 169–198.

4. Becker, E., Hiller, W., and Kowalewski, T., "Experimental and Theoretical Investigation of Large Amplitude Oscillations of Liquid Droplets," *Journal of Fluid Mechanics*, Vol. 231, 1990, pp. 189–210.

5. Beyer, W. H., ed., *CRC Standard Mathematical Tables and Formulas.* Ann Arbor: CRC Press, 29th ed., 1991.

6. Currie, I. G., *Fundamental Mechanics of Fluids.* New York: McGraw-Hill Publishing Company, 1974.

7. Daidzic, N., *Nonlinear Droplet Oscillations and Evaporation in an Ultrasonic Levitator.* Ph.D. Dissertation, Technical University of Erlangen-Nurnberg, 1995.

8. Hilbing, J. H., Heister, S. D., and Spangler, C. A., "A Boundary Element Method for Atomization of a Finite Liquid Jet", *Atomization and Sprays*, V 5, No. 6, 1995, pp 621-638.

9. Hsiang, L.-P. and Faeth, G. M., "Near-Limit Drop Deformation and Secondary Breakup," *Int. J. Multiphase Flow*, Vol. 18, No. 5, 1992.

10. Kreyszig, E., *Advanced Engineering Mathematics.* New York: John Wiley & Sons, 6th ed., 1988.

11. Lamb, H., *Hydrodynamics.* Dover Publications, 6th ed., 1982.

12. Liggett, J. A. and Liu, P. L.-F., *The Boundary Integral Equation Method for Porous Media Flow.* London: George Allen and Unwin, 1983.

13. Longuet-Higgins, M. S. and Cokelet, E. D., "The Deformation of Steep Surface Waves on Water, I, A Numerical Method of Computation," *Proceedings of the Royal Society of London A*, Vol. 350, 1976, pp. 1–26.

14. Lundgren, T. S. and Mansour, N. N., "Oscillations of Drops in Zero Gravity with Weak Viscous Effects," *Journal of Fluid Mechanics*, Vol. 194, 1988, pp. 479–510.

15. Mansour, N. N., and Lundgren, T. S., "Satellite Formation in Capillary Jet Breakup", *Physics of Fluids*, V2, 1990, pp. 1141-1144.

16. Medina, D. E., "On Droplets and Boundary Elements," Sibley School of Mechanical and Aerospace Engineering, Cornell University, Technical Report FDA-89-12, Ithaca, New York, 1989.

17. Miksis, M., Vanden-Broeck, J., and Keller, J., "Axisymmetric Bubble or Drop in a Uniform Flow," *Journal of Fluid Mechanics*, Vol. 108, 1981, pp. 89–100.

18. Murray, I., F., "Modeling Acoustically-Induced Oscillations of Droplets", M.S. Thesis, Purdue University, 1996.

19. Press, W. H., Teukolsky, S. A., Vetterling, W. T., and Flannery, B. P., *Numerical Recipes in FORTRAN, The Art of Scientific Computing.* New York, NY: Cambridge University Press, 2nd ed., 1992.

20. Prosperetti, A., "Free Oscillations of Drops and Bubbles: the Initial Value Problem," *Journal of Fluid Mechanics*, Vol. 100, 1980, pp. 333–347.

21. Rayleigh, L., "On the Capillary Phenomenon of Jets," *Proceedings of the Royal Society of London*, Vol. 29, 1879, pp. 71–97.

22. Smirnov, V. I., *A Course of Higher Mathematics*, Vol. II. New York: Pergamon Press, 1964.

23. Spangler, C. A., "Nonlinear Modeling of Jet Atomization in the Wind-Induced Regime," M.S. Thesis, Purdue University, 1994.

24. Trinh, E. and Wang, T., "Large-Amplitude Free and Driven Drop Shape Oscillations: Experimental Observations," *Journal of Fluid Mechanics*, Vol. 122, 1981, pp. 315–338.

25. Tsamopoulos, J. A. and Brown, R. A., "Nonlinear Oscillations of Inviscid Drops and Bubbles," *Journal of Fluid Mechanics*, Vol. 127, 1983, pp. 519–537.

26. Wang, T., Anilkumar, A., and Lee, C., "Oscillations of Liquid Drops: Results from USML-1 Experiments in Space," *Journal of Fluid Mechanics*, Vol. 308, 1996, pp. 1–14.

Figure 1: Schematic of Computational Domain and Boundary Conditions

Figure 2: Comparisons of Predicted Frequency Shifts for Nonlinear Oscillations of a Droplet

We = 0.90   We = 1.535

Miksis et al. • • •
BEM   ———
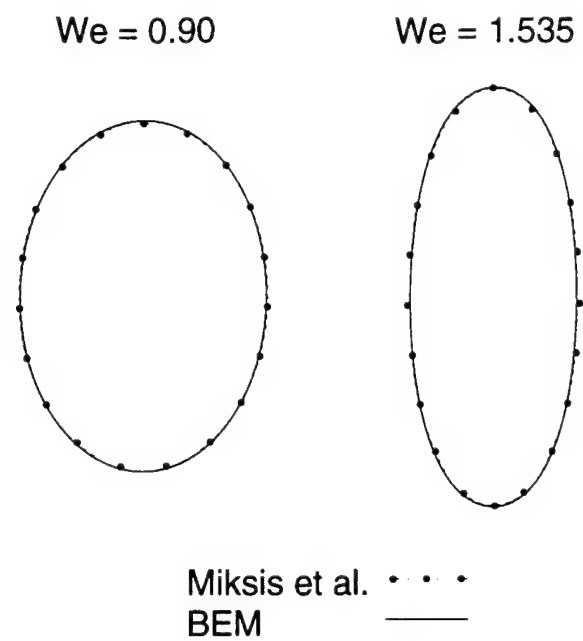
Figure 3: Comparisons of Steady State Droplet Profiles
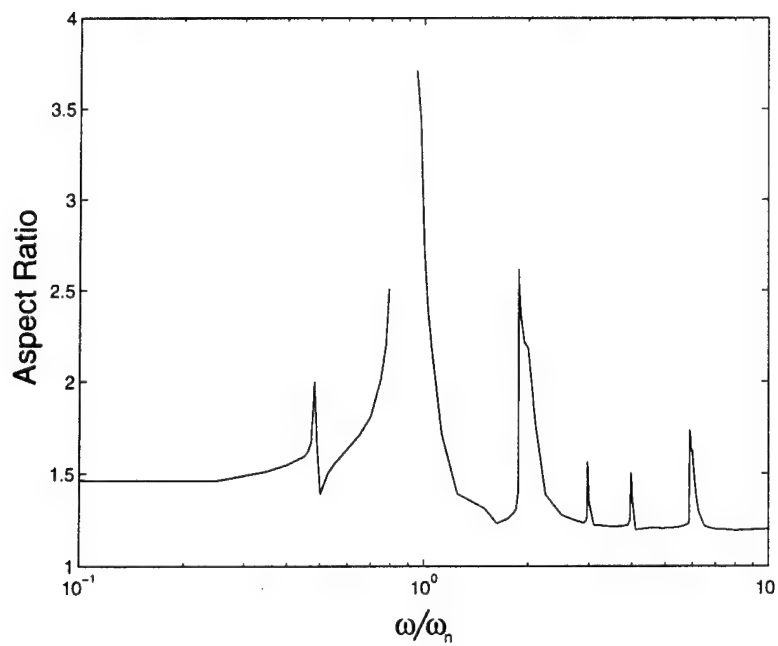
Figure 4: Frequency Response Spectrum

$\omega/\omega_n = 0.79$, We = 0.5779, $\varepsilon = 0.00123$

Figure 5: Time History of Top Node Position

$\omega/\omega_n = 0.79$, We = 0.5779, $\varepsilon = 0.00123$

0 T   .05 T   .11 T   .46 T

.54 T   .89 T   .95 T   1 T
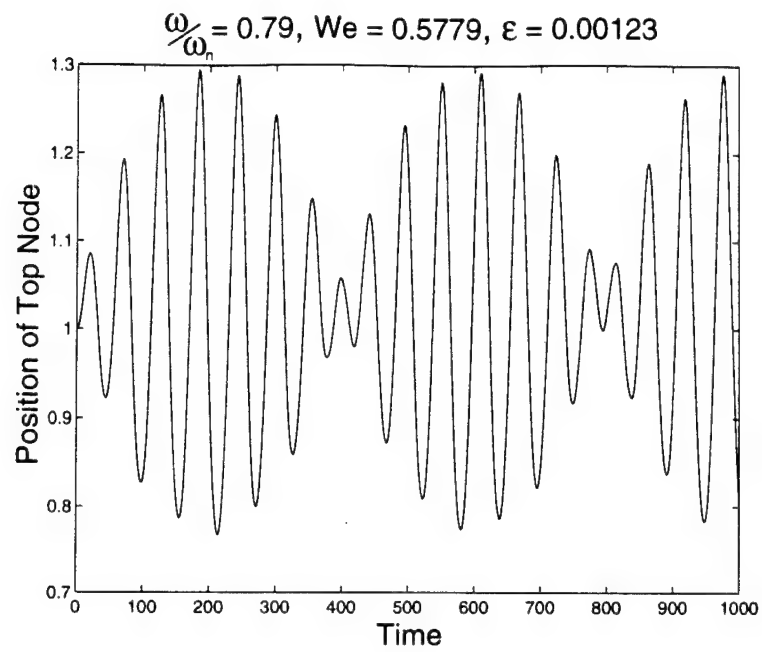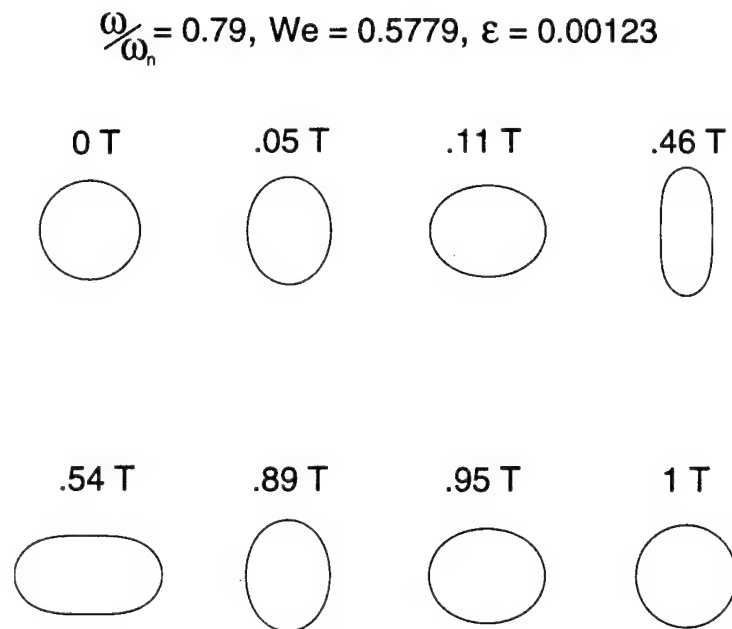
Figure 6: Time History of Droplet Profiles

73

$\omega/\omega_n = 0.79$, We = 0.5779, $\varepsilon = 0.00123$
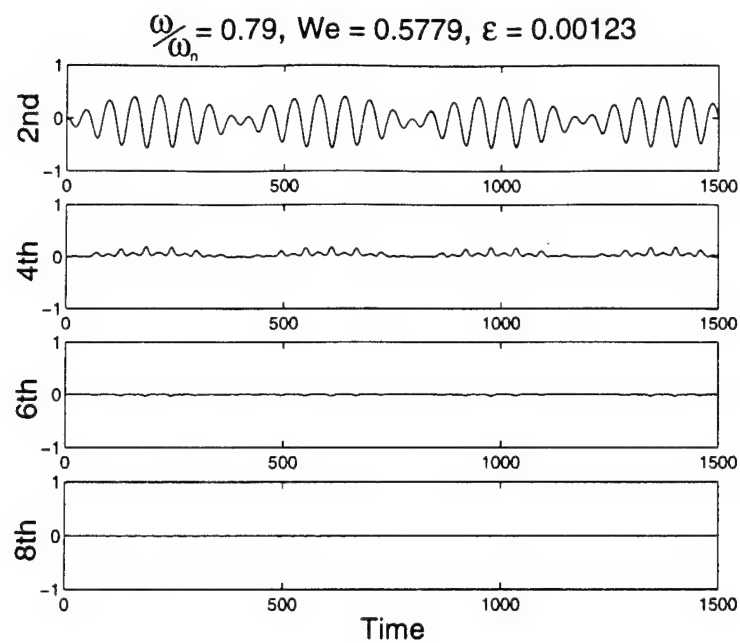
Figure 7: Time History of Mode Coefficients
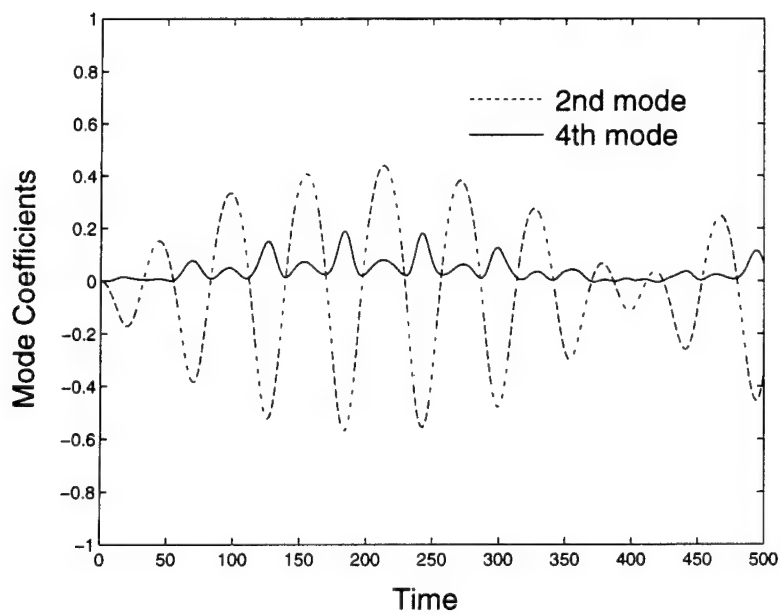
Figure 8: Oscillatory Mode Interference
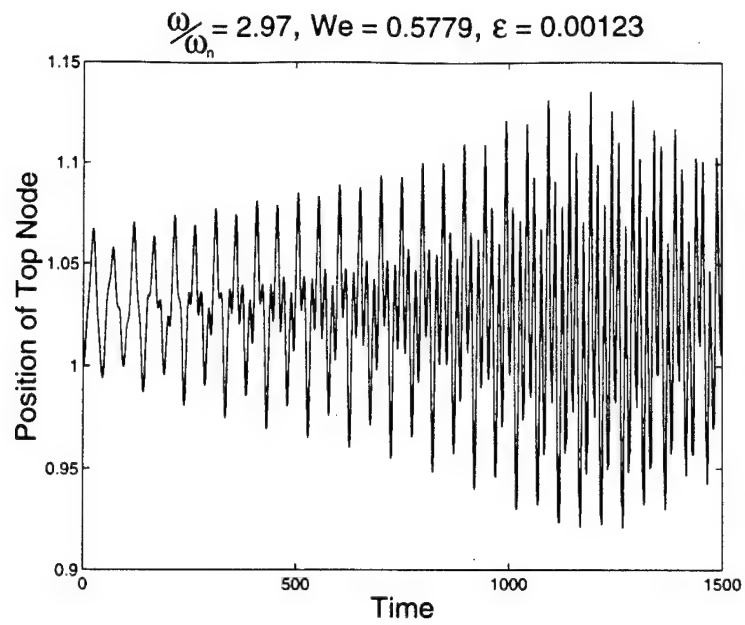
Figure 9: Time History of Top Node Position
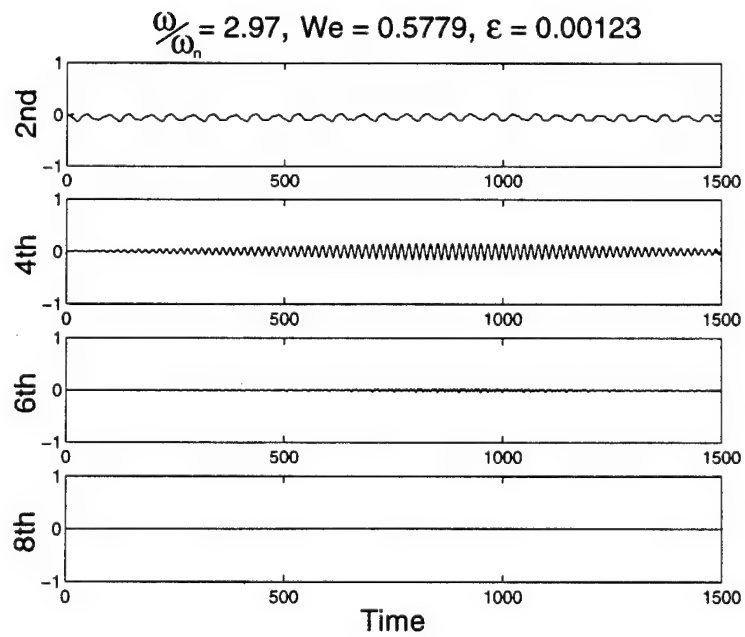
Figure 10: Time History of Mode Coefficients
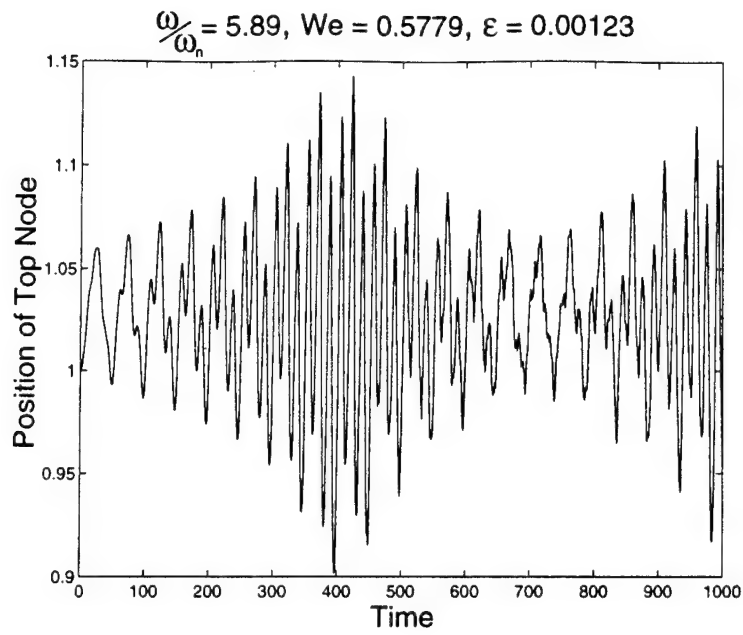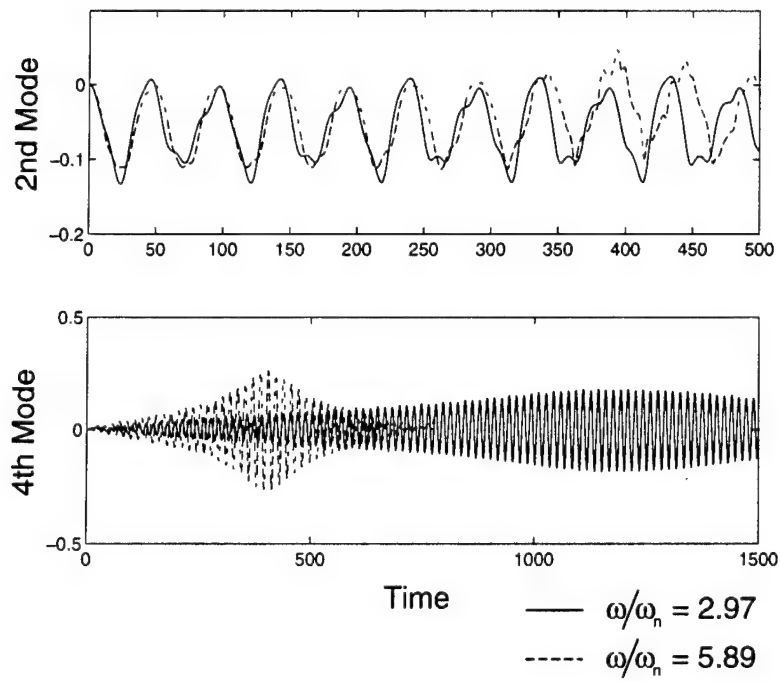
Figure 11: Time History of Top Node Position

Figure 12: Second and Fourth Mode Coefficients

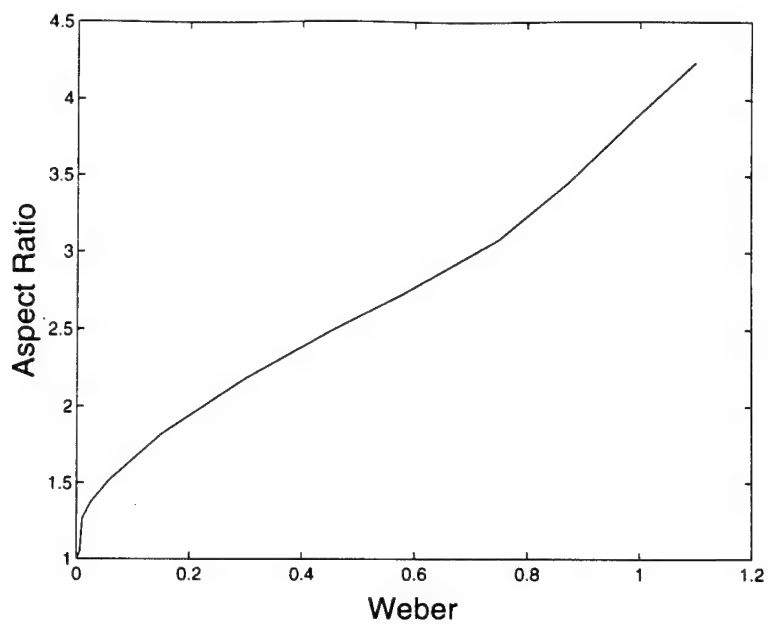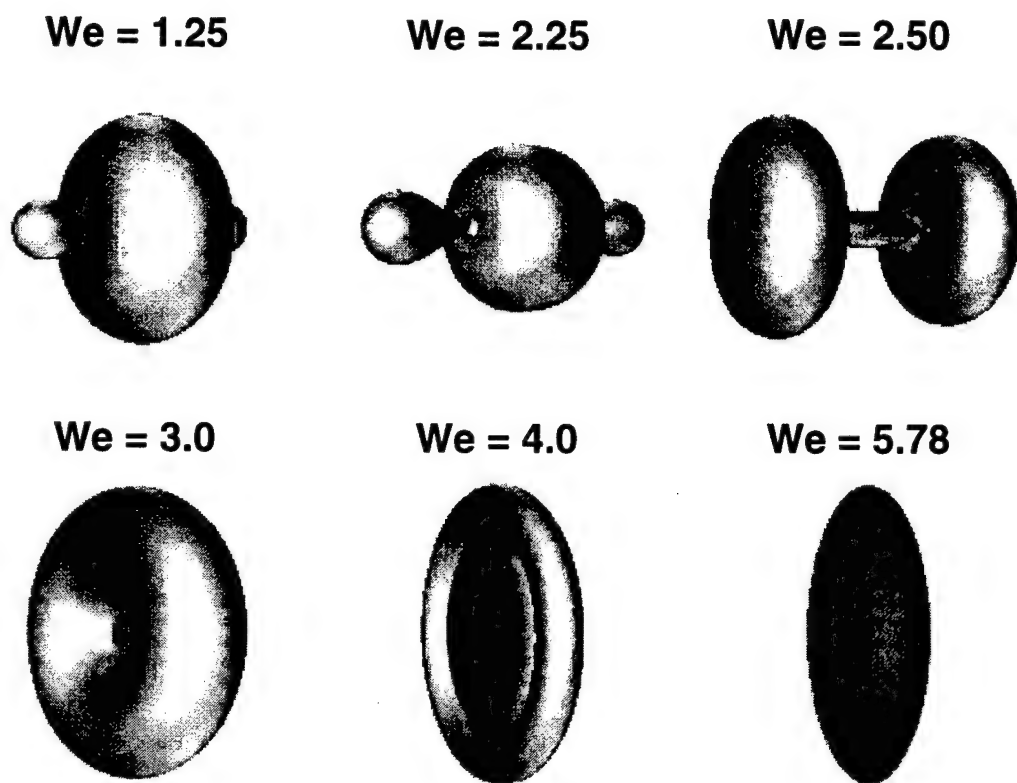Figure 13: Effects of the Weber Number upon Droplet Behavior ($\epsilon = 0.00123, \omega = \omega_n$)

We = 1.25   **We = 2.25**   **We = 2.50**

We = 3.0   **We = 4.0**   **We = 5.78**

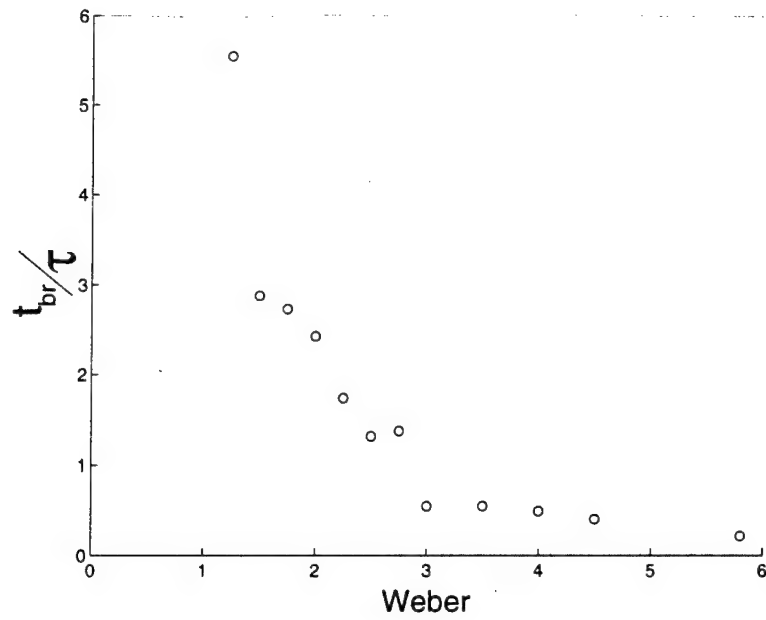Figure 14: Droplet Atomization Shapes at Various Weber Numbers ($\epsilon = 0.00123, \omega = \omega_n$)

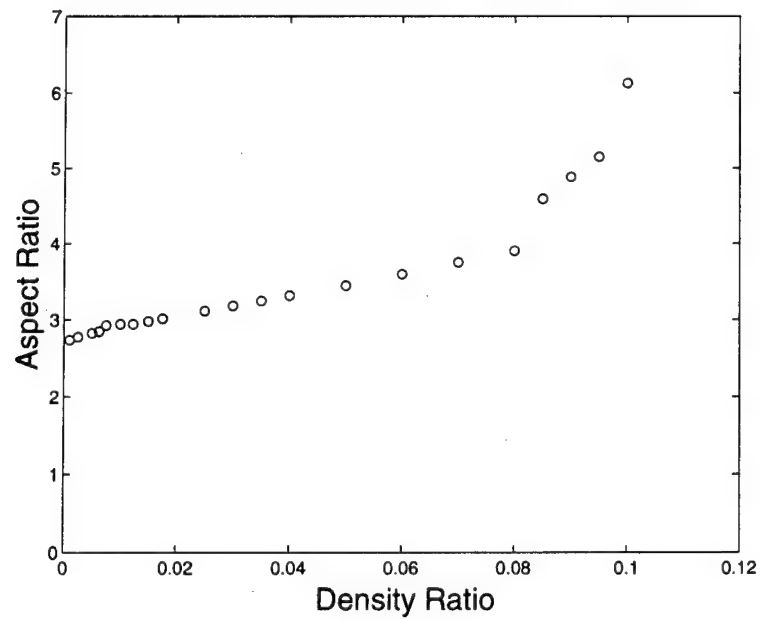Figure 15: Time Required for Droplet Break Up for Various Weber Numbers ($\epsilon = 0.00123, \omega = \omega_n$)

Figure 16: Influence of Liquid Density upon Droplet Behavior (We $= 0.5779, \omega = \omega_n$)

78

10   Appendix E - BEMs for Two-Fluid Flows

Heister, S. D., "Boundary Element Methods for Two-Fluid Free Surface Flows", In Review, *Engineering Analysis with Boundary Elements*, 1996.

BOUNDARY ELEMENT METHODS FOR TWO-FLUID FREE SURFACE FLOWS

S. D. Heister

Associate Professor, School of Aeronautics and Astronautics, Purdue University, W. Lafayette, IN, 47907

Abstract

Flows in which a low density (gaseous) phase contributes to the motion of a free surface have been studied numerically using boundary element methods. A stable, time-accurate integration scheme for the coupled, nonlinear free surface boundary conditions is described for the case where both phases are incompressible and inviscid. The effect of increasing gas/liquid density ratio on stability of the methodology is briefly discussed. The technique is illustrated through a series of examples involving: an infinite-length (periodic) liquid jet in a "wind-induced" flow regime; a two-dimensional liquid column subjected to acoustic excitation; and a finite-length liquid jet injected into a quiescent gas.

Introduction

Within the past two decades, researchers have adopted boundary element solutions to problems involving nonlinear deformations of a free surface. In these problems, the boundary element approach is attractive because the "grid" is simplified by one dimension over that of a more traditional computational fluid dynamic calculation. For two-dimensional geometries, the grid in the BEM formulation is simply a curved line. In problems where surface topology changes occur (such as atomization), this simplification becomes quite valuable. In fact, recent BEM simulations[1] have been conducted in which calculations proceed beyond atomization events.

Numerical approaches utilizing Finite Element Methods (FEM) and the Volume of Fluid (VOF) method have also been applied to problems of this type. The VOF technique relies on the interpolation of the surface location from a fixed computational mesh. In capillary flows, this interpolation procedure can introduce substantial inaccuracy in determining surface curvature (and hence the capillary force). As an example, a typical VOF calculation involving sloshing of a fluid in a tank[2] exhibits a 1% error in preserving the liquid volume, while a BEM calculation exhibits a 0.01% volume error[3]. A typical BEM calculation[1] involving nonlinear oscillations of a droplet utilizing 45 nodes achieves a maximum volume error of 0.04 %, while a comparable FEM calculation[4] would use over 1600 nodes and produce a volume error of 0.8%.

For these reasons, we have seen a variety of applications of BEMs to problems involving large deformations of a free surface. Several solutions have been developed for nonlinear evolution of water waves[5-7], and for nonlinear deformations of both viscous and inviscid drops[1,8]. A variety of solutions have been obtained for creeping (Stokes) flows in liquid columns[9-11], and in annular layers[11]. Inviscid solutions have also been obtained for both infinite[12] and finite-length[1] liquid jets, as well as for dripping flows[1], fountains[1], and fluid sloshing problems[13].

These simulations have all had to treat the primary nonlinearity associated with free surface flows involving the fact that the current surface location cannot be decoupled from the pressure/velocity field. In other words, the surface pressure is dependent on the shape of the interface, which in turn depends on the local pressure distribution. Most researchers have treated this nonlinearity by utilizing small time steps such that the surface pressure/velocity is invariant over a given step. More elaborate treatments have been suggested and validated by Liggett and coworkers[14,15].

Recently, a variety of models have been developed in order to include the influence of gas-phase pressure distribution on the nonlinear evolution of the interface[16-18]. Developing a capability to address these flows permits the consideration of problems in which wind-induced, or acoustic interactions from the gas phase can be included as physical factors affecting distortion of the interface. In this case, the nonlinear free surface boundary condition is coupled between the two fluids bordering the interface. This complication introduces some unique computational issues for those interested in modeling these flows. In this paper, we address these issues as applied to several problems of engineering interest. The following section provides

a detailed description of the BEM, while subsequent sections highlight boundary condition treatments for three example problems.

Model Development

Our interest lies in developing models which can address capillary (surface tension) forces at the interface. By choosing the liquid density (ρ), the size/height of the liquid body (a), and a farfield velocity (U) as dimensions, the gas/liquid density ratio:

$$\epsilon = \rho_g/\rho \tag{1}$$

and the Weber number based on gas density:

$$We = \frac{\rho_g U^2 a}{\sigma} \tag{2}$$

become the two dimensionless parameters characterizing the flowfield. Here, the Weber number measures the ratio of inertial forces imposed by the gas phase to surface tension (σ) forces. In the following development, we presume that the nondimensionalization described above has been applied.

We assume that both phases can be represented as incompressible, inviscid fluids. In this case, a velocity potential (whose gradient is simply the velocity) exists. Let ϕ and ϕ_g represent the velocity potential in liquid and gaseous phases, respectively. Continuity requires that both velocity potentials satisfy Laplace's equation:

$$\nabla^2 \phi = \nabla^2 \phi_g = 0 \tag{3}$$

Proceeding with a standard BEM formulation, the integral form of eqn 3 for the liquid domain becomes:

$$\alpha \phi(\vec{r_i}) + \int_\Gamma [\phi \frac{\partial G}{\partial n} - qG]d\Gamma = 0 \tag{4}$$

where $\phi(\vec{r_i})$ is the value of the potential at a point $\vec{r_i}$, Γ denotes the boundary of the domain, and G is the free-space Green's function corresponding to Laplace's equation. An analogous form of eqn 4 can also be derived for the gas phase potential. For a well-posed problem, either ϕ or $q = \partial \phi / \partial n$ must be specified at each "node" on the boundary. Here n is the outward normal to the boundary so that q represents the velocity normal to the boundary. The quantity α in eqn 4 results from singularities introduced as the integration passes over the boundary point, $\vec{r_i}$.

Models have been developed for both two-dimensional and axisymmetric flowfields. If we let r and z denote radial and axial coordinates, respectively, and denote the base point with subscript "i", the Green's function solution to the axisymmetric Laplacian can be written:

$$G = \frac{4rK(p)}{\sqrt{(r + r_i)^2 + (z - z_i)^2}} \tag{5}$$

where

$$p = \frac{(r - r_i)^2 + (z - z_i)^2}{(r + r_i)^2 + (z - z_i)^2} \tag{6}$$

and $K(p)$ is the complete elliptic integral of the first kind. For computational efficiency, this quantity is calculated using a curve fit[19] which has an accuracy to 10^{-8}.

In the case of a 2-D flow (letting x and y represent the coordinates), we have:

$$G = \frac{1}{2\pi} ln|\vec{r} - \vec{r_i}| = \frac{1}{4\pi} ln[(x - x_i)^2 + (y - y_i)^2] \tag{7}$$

In both cases, we have utilized linear elements in the formulation of a set of integral equations over a discretized boundary. Linear elements are desirable for problems with moving surfaces since the BEM solution in this case will return velocities at the ends of each segment corresponding to the nodal locations. In the case of constant elements (for example), a nodal velocity would be calculated at the center of each segment, but the end points of the segment would require a separate treatment (based on interpolation of nodal velocities) to update the mesh at subsequent times.

For the 2-D flows, integration across a segment can be carried out analytically. Singularities resulting from integration across a segment containing the base point are also integrable. In the case of axisymmetric flow, the integrations must be carried out numerically. In this case, we choose a four-point Gaussian quadrature for evaluation of integrals. Logarithmic singularities which arise in the elliptic integral when the segment contains the base point are treated with a special Gaussian integration designed to accurately treat this condition. Additional details regarding the numerical implementation can be found in Refs. 1 and 17 for the axisymmetric and 2-D cases, respectively.

Free Surface Treatment

Governing Equations

The main challenge in developing models capable of tracking large deformations of an interface lies in the treatment of the free surface itself. Since capillary forces are important, it is crucial to develop a treatment capable of accurately determining surface curvature at all times during the simulation. For this reason, all models employ fourth-order centered differencing (on a generalized, variable spacing mesh) to determine surface curvature. Curvature is calculated based on coordinate derivatives as a function of distance along the surface using the parametric representation due to Smirnov[20].

The modeler has the choice of tracking the motion of free surface nodes in a variety of directions[6]. In current models, we have opted to track surface nodes along the local liquid velocity vector. Under this assumption, for an axisymmetric situation, flow kinematics require:

$$\frac{Dz}{Dt} = \frac{\partial \phi}{\partial z} \qquad\qquad \frac{Dr}{Dt} = \frac{\partial \phi}{\partial r} \tag{8}$$

where the notation $D()/Dt$ implies a Lagrangian derivative for points on the surface moving with the local liquid velocity.

Recognizing that our BEM solver will return velocities normal to the surface, we employ the velocity transformations:

$$\frac{\partial \phi}{\partial r} = \frac{\partial \phi}{\partial s} sin(\beta) + qcos(\beta) \qquad\qquad \frac{\partial \phi}{\partial z} = \frac{\partial \phi}{\partial s} cos(\beta) - qsin(\beta) \tag{9}$$

where β is the local wave slope and $\partial \phi / \partial s$ is the velocity tangential to the local surface. This tangential velocity is calculated using 5-point centered differences on ϕ, except for nodes adjacent to ends of the free surface, where a 3-point formula is employed. The local wave slope, β, is calculated following the formulation of Medina[21]. For each node, a parabola is defined such that it passes through the previous node, the node in question, and the following node. The slope of the surface is given by the tangent to the parabola at the central node. A completely analogous treatment can be employed for 2-D flows by replacing r with y and z with x in eqns 8 and 9.

Dynamics of the interface are addressed through the unsteady Bernoulli equation. In an Eulerian system where time derivatives are assumed to occur at a fixed spatial location, the dimensionless form of this relation for the liquid surface is:

$$\frac{\partial \phi}{\partial t} + \frac{1}{2}(\nabla \phi)^2 + P_g + \frac{\kappa}{We} = 0 \tag{10}$$

where P_g is the gas pressure at the interface, and κ is the surface curvature. The Eulerian – Lagrangian transformation for nodes on the interface moving with the *liquid velocity* is:

$$\frac{D(\ )}{Dt} = \frac{\partial(\ )}{\partial t} + \nabla \phi \cdot \nabla(\ ) \tag{11}$$

Using this transformation, the Bernoulli equation in the liquid becomes:

$$\frac{D\phi}{Dt} = \frac{1}{2}(\nabla \phi)^2 - P_g - \frac{\kappa}{We} \tag{12}$$

while an analagous treatment for the gas phase gives:

$$\epsilon \frac{D\phi_g}{Dt} = \epsilon \nabla \phi \cdot \nabla \phi_g - \frac{\epsilon}{2}(\nabla \phi_g)^2 - P_g \tag{13}$$

Time Integration Scheme

Mathematically, eqns 8, 12, and 13 provide a system of relations to describe the evolution of the surface shape (r, z or y, z) and velocity potentials for unsteady motion of the interface. These equations are integrated in time using a fourth-order Runge-Kutta scheme[1]. This scheme has the advantage of full fourth-order accuracy without the requirement of a knowledge of the "history" for a given nodal location; i.e. information at previous time levels is not required in the integration algorithm. This feature can be advantageous in calculations where a variable timestep is employed or where the number of nodes along the free surface is not constant (due to atomization events or surface regridding).

As mentioned previously, the main challenge in this problem is the development of a stable, consistent procedure to handle the coupled, nonlinear boundary conditions at the interface (eqns 12 and 13). More specifically, if we regard eqn 13 as an expression for P_g, than an approximation for the derivative $D\phi_g/Dt$ is required. We have found, that for a wide array of problems it is adequate to approximate this derivative using a first-order backward difference scheme.

$$\frac{D\phi_g}{Dt} = \frac{\phi_g^{i+1} - \phi_g^i}{\Delta t} \tag{14}$$

where "i" denotes time level.

In problems where the gas flows tangential to the liquid surface over most of the time-dependent process, the major term influencing the gas pressure in eqn 13 turns out to be the term involving $(\nabla \phi_g)^2$. In this case, highly accurate approximation of $D\phi_g/Dt$ is obviously not required. However, we have found the first-order backward difference (eqn 14) to be adequate even in problems where stagnation points are present. In this case, inspection of eqn 13 indicates that the $D\phi_g/Dt$ term is the major component leading to changes in gas pressure. In the examples which follow, we show that the simple approximation in eqn 14 is adequate for a wide variety of flows.

The following procedure is implemented for nodes on the free surface:

- At the start of a given time step, the value of ϕ is known. Using this value as a boundary condition on the interface, the liquid velocity q can be determined via solution of Laplace's equation (eqn 4).

- Since the gas nodes on the interface are fixed to move with the liquid nodes, this liquid velocity is used as the gas phase boundary condition ($q_g = -q$) to calculate the ϕ_g value on the gas side of the interface.

- This value of the gas phase velocity potential is then used in eqn 13 to determine the gas pressure at this new time step using the approximation for $D\phi_g/Dt$ given in eqn 14.

- The gas pressure at the new time is then used in eqn 12 to calculate the current $D\phi/Dt$ which is then integrated in time.

Since the nodes on the interface are allowed to move with their local velocity, over time they tend to group themselves in regions of high curvature. This phenomena leaves regions of lower curvature poorly defined. To alleviate this problem, the surface mesh is regridded using a series of cubic splines (for surface coordinates, ϕ, and ϕ_g) at each time step to keep the spacing between the nodes constant along the surface. The use of the Runge-Kutta integration scheme is well suited to this type of remeshing, since it does not require information on node positions at previous time levels to predict the subsequent motion of the surface. Also, we note that regridding the surface can be accomplished in this case since the approximation for $D\phi_g/Dt$ (eqn 14) involves only two time levels. If more accurate representations of this derivative are required, then regridding tends to destroy information about previous ϕ_g values on given nodal locations.

Finally, we note that the regridding process does provide a natural "smoothing" of the surface. Many previous authors[7,8,12,15] have been forced to implement smoothing procedures to alleviate "zig-zag" instabilities which develop on the surface after a large number of time steps. Because of the regridding procedure, we have not had to implement any formal smoothing of the surface (or any other functions associated with the surface). For these reasons, calculations using the methodology described above have very little numerical dissipation. In the following sections, we provide three examples to illustrate the results of the free surface treatment described above.

Example #1: Infinite Liquid Jet in Wind-Induced Flow Regime

The distortion and atomization of a liquid jet is one of the most frequently studied free surface problems due to its wide array of applications (atomizers, ink-jet printers, fire hoses, etc.). To date, most analyses have presumed a periodic solution exists, whereby the study focuses on a single wavelength of fluid. Such conditions can be experimentally simulated in the case of low speed jets by providing low amplitude acoustic or mechanical excitation of the orifice[22]. Until recently, the nonlinear analyses applied to this problem have ignored the presence of the gas phase. Using the formulation described in the previous sections, we have developed a fully nonlinear simulation of the jet in the presence of a gas (typically referred to as the wind-induced flow regime).

A schematic of the computational domain is shown in Fig. 1 in which liquid nodes are denoted "o", while the gas nodes are denoted "x". We presume that the coordinate system is attached to the liquid, so that U is the relative velocity between the two fluids at a location far from the interface. We place the upper boundary in the gas phase far enough away from the surface such that there is negligible flux of fluid through the interface. The assumed periodicity requires that on the vertical boundaries $q = 0$ in the liquid phase and $\partial \phi_g / \partial r = 0$ in the gas phase. No nodes are required along the centerline since both G and $\partial G / \partial n$ vanish for the axisymmetric geometry assumed.

The initial wave shape of the surface is assumed to be:

$$r = 1 + \eta \cos(kz) \tag{15}$$

where η is the initial surface deflection and k is the wave number of the forcing disturbance on the jet. For $\eta << 1$, results from a linear analysis[23] can be employed to give the initial gas-phase pressure and velocity potential along the interface:

$$P_g = -\epsilon \eta k \cos(kz) \frac{K_0(kr)}{K_1(k)} \tag{16}$$

$$\phi_g = z - \eta \sin(kz) \frac{K_0(kr)}{K_1(k)} \tag{17}$$

where K_0 and K_1 are modified Bessel functions of the second kind. In the liquid phase, we presume that the interface is initially at rest to provide a starting condition for the integration.

Typical calculations involve 60-100 nodes along the interface. Vertical surfaces in the gas phase employ exponential stretching to permit greater resolution near the interface. Near the interface, nodal spacings along vertical surfaces are kept at values near that of the interface itself. A dynamic time-step criteria is employed to insure that nodes move no more than 5% of the nodal spacing on a given time step. This criteria permits considerable acceleration of the code (as compared to the constant time step case) since the initial surface velocities are very small. Surface velocities grow to very large values as curvature increases dramatically near the pinching of the jet. Calculations are stopped when a node reaches a distance of 1% of the initial jet radius from the centerline. A typical calculation takes about 25,000 CPU seconds on an IBM RISC 6000 Model 580 machine.

Results from sample calculations are included in Figs 2 and 3. In Fig. 2, the evolution of the jet is shown for $We = 1$, $\epsilon = 0.00129$ which would correspond to a 1 mm water jet issuing at 7.7 m/s into ambient pressure air (multiple waves are shown here for clarity). A dimensionless wave number of $k = 1.027$ is selected, since linear theory[24] predicts this to be the most unstable value for this flow condition. This calculation employs 65 nodes along the interface and a total of 87 and 259 nodes in liquid and gaseous domains, respectively. Under these conditions, aerodynamic and surface tension forces are comparable and the simulation predicts that the jet will break at the centerline leading to the formation of a "main" and "satellite" drop from each wave along the surface. Jets atomizing in this fashion are said to lie in the *first wind-induced regime*. Predictions of the size of main and satellite drops agree well with experimental measurements[16] for low speed jets.

Figure 3 shows the influence of increased gas velocity for the case: $We = 5$, $\epsilon = 0.0013$, $k = 4.23$. In this case, the increased influence of the gas-phase leads to the pinching of an annular ring of fluid at the periphery of the jet (characteristic of the *second wind-induced regime*). The increased complexity of the surface in this case necessitated a more refined grid which employs 89 nodes along the interface. While viscous effects would tend to cause the annular ring to be swept downstream, aerodynamic ripples of this nature have been observed experimentally[25].

Spangler[16] has investigated the influence of ϵ on the performance of the code. The algorithm produces stable results for ϵ values approaching unity, but diverges rapidly for values near or above this threshold. As ϵ increases, the importance of the gas phase also increases. For $\epsilon > 1$ we presume it would be more logical to interchange the treatment of liquid and gas phases in the procedure described above. In addition, it is likely that more accurate and stable results would be obtained by tracking nodes along the "gas" phase velocity vector for these conditions. In practice, ϵ values less than 0.01 characterize nearly all gas/liquid flows; even at high pressure conditions present in a rocket combustion chamber.

Example #2: Liquid Column Subjected to Acoustic Perturbations

Nonlinear interactions of various atomization processes with acoustic waves have been implicated as a possible source of combustion instabilities in liquid rocket engines[26]. For this reason, a 2-D model was developed to assess the distortion of a liquid column subjected to a transverse acoustic wave. Here, we presume that the wavelength of the acoustic disturbance is much greater than the diameter of the column such that the acoustic wave can be modeled as an unsteady incompressible flow.

Under these assumptions, the computational domain for this analysis is shown in Fig. 4. Due to symmetry, only a 1/4 cylinder domain need be considered. In Fig. 4, liquid nodes are represented by "o" and gas nodes by "X". For this 2-D problem (flow is into the page), nodes are required along both symmetry axes. The boundary condition $q = q_g = 0$ is applied along the $y = 0$ symmetry plane. Along the $x = 0$ plane, we specify $q = 0$ and $\partial\phi_g/\partial y = 0$ for the gas phase. Once again, exponential stretching is applied to gas nodes along the symmetry axis in order to increase resolution near the stagnation point at the junction with the column.

The outer boundary in the gas domain is placed far enough (15 jet radii) from the liquid such that the velocity potential on this surface may be assumed to be a pure acoustic wave traveling in the horizontal direction:

$$\phi_g = x\cos(\omega_g t/2) \tag{18}$$

where ω_g is the frequency of the acoustic wave. The factor of 1/2 in the cosine wave results from the fact that the solution is insensitive to flow direction, i.e. a wave traveling to the right sets up the same pressure distribution as a wave traveling to the left. In this problem, we expect large column response when the frequency of the acoustic wave is near the natural frequency of the column. A linear analysis[26] shows that the dimensionless column natural frequency can be expressed:

$$\omega_n = \sqrt{\frac{6\epsilon}{(1+\epsilon)We}} \tag{19}$$

Here we have chosen the column radius, liquid density, and the peak velocity from the acoustic wave as dimensions.

A time step of 0.005 was used in all simulations. The model was validated using the analytic solution for flow over a cylinder. In addition, results compare very well with the steady-state solutions[27] for the case of a uniform flow over a liquid cylinder. Typical grids employ 25 nodes on the interface, 21 nodes on the outer gas boundary, 15 gas nodes along the symmetry planes, and 8 liquid nodes along symmetry planes. Typical run times are 4-16 hours on a Sun Sparcstation 1000 computer.

Sample results from the model are provided in Figs. 5-7. In Fig. 5, the motion of a node at the top of the column is shown for the case: $We = 0.1$, $\epsilon = 0.01$, $\omega_g = \omega_n$ which represents excitation of the column at its lowest-order natural frequency. Even though the energy input is unbounded, the column response is bounded. This phenomena is caused by a shift in the column natural frequency at larger deformations. At large amplitudes, the natural frequency is substantially lower than that predicted by the linear theory (eqn 19), which ultimately leads to a destructive interference from the constant frequency acoustic wave. Nonlinear frequency shifts have been characterized for both droplets[1] and columns[17] in the literature. The simulation fails at $t \approx 95$ due to the development of a sawtooth appearance along the interface. Such occurances are common in long time integrations of this nature (note that we have taken almost 20,000 time steps prior to failure of the simulation). As mentioned previously, numerical smoothing would be required to extend the simulation to longer times.

85

The shapes of the column at various stages in the process are shown in Fig. 6. In contrast to oscillations of droplets, the column is fairly insensitive to fourth-mode activity so that a second (primary) mode oscillation occurs at all gas frequencies[17]. The effects of gas density changes are assessed in Fig. 7 for the harmonic case ($\omega_g = \omega_n$) by comparing the maximum aspect ratio of the column ($AR(max)$) at various ϵ values. Since Weber number is fixed in these simulations, the effects of increasing ϵ can be thought of as a decreased liquid density (and hence liquid inertia). For this reason, we expect a greater column response at higher ϵ values. Figure 7 confirms this behavior, showing a greater sensitivity to ϵ as $\epsilon \to 0.1$. At $\epsilon > 0.01$, the treatment of the interface does not provide viable solutions and numerical zig-zag instabilities are generated early in the calculation.

It is interesting to note that these solutions break down at a much lower value of ϵ than those in the first example. While the breakdown point is clearly dependent on Weber number, another explanation for this behavior is the increased sensitivity of the solution to the approximation of $D\phi_g/Dt$ near the stagnation point at the base of the column. In fact, Rutz[17] has extended $We = 0.1$ solutions to higher ϵ values by removing the regrid procedure and implementing fourth-order time integrations of eq. 13.

Example #3: Liquid Jet Injected into Quiescent Gas

A final example providing unique boundary conditions for a fully-coupled gas/liquid flow is outlined in Fig.8. In this axisymmetric problem, a finite-length liquid jet is injected into a quiescent gas. Note that the orifice geometry can also be included in this simulation; a unique treatment as compared to most atomization models. The outer boundary in the gas domain is made large enough to encompass the entire liquid domain for the entire duration of the calculation. In addition, this boundary is placed far enough from the liquid so it can be assumed to be at constant pressure. Similarly, the hemispherical inflow boundary is placed far enough from the orifice entrance such that constant pressure can be assumed.

Combustion instabilities have been attributed to the "dynamic orifice flow" created by a time-varying discharge pressure. Using the domain in Fig. 8, we can assess liquid behavior for both constant and time-varying orifice pressure drops. Even though a stagnation point lies at the tip of the jet, we have found that the free-surface treatment described in Example # 1 is adequate for this problem. Nodes are added along the free surface as the jet issues from the orifice so as to maintain a roughly constant nodal spacing. Surface nodes are regrid at each time step by fitting surface coordinates and velocity potentials with cubic splines, as described in Example # 1.

The inflow and outer gas boundaries require a unique treatment in this example. On the inflow boundary, Bernoulli's equation can be written:

$$\frac{\partial \phi}{\partial t} = \frac{1}{2}(\nabla \phi)^2 - P_{lo} \tag{20}$$

where P_{lo} is the prescribed inflow pressure. On the outer gas boundary, Bernoulli's equation is:

$$\frac{\partial \phi_g}{\partial t} = \frac{1}{2}(\nabla \phi_g)^2 - P_{go} \tag{21}$$

where P_{go} is the prescribed gas pressure. Equations 20 and 21 require no Eulerian/Lagrangian transformation since nodes on these boundaries remain fixed.

In this example, we presume that all pressures are nondimensionalized using the liquid density and the ideal orifice exit velocity (assuming a discharge coefficient of unity). Under this assumption, P_{lo} and P_{go} must be related by:

$$P_{lo} - P_{go} = \frac{1}{2}(1 - \frac{1}{4R_{inlet}^2}) \tag{22}$$

where R_{inlet} is the radius of the hemispherical inlet at the entry to the orifice. If an oscillating P_{go} is specified, then the mean value is used in eqn 22 to find the appropriate P_{lo} to support the desired nondimensionalization. Using this approach, the problem is characterized by a Weber number, density ratio, and the frequency and amplitude of any pressure perturbation applied at the outer gas boundary.

On the liquid inflow boundary, we begin calculations by setting $q = -1/(2R_{inlet}^2)$ along the inflow boundary and assume a small column of liquid (with a hemispherical cap) is issuing from the orifice with constant axial velocity, $\phi = z$. We set $q = 0$ along solid boundaries representing walls of the orifice or of the chamber and solve Laplace's equation to provide initial values for ϕ along the inflow boundary. The outer

gas boundary is placed far enough from the small liquid jet such that a stagnant condition ($\phi_g = 0$) initially. With this information, we can begin the time-stepping procedure described in Example #1 to determine ϕ_g values and velocities along the interface. In this case, we integrate an additional two equations (eqn 20 and 21) to update ϕ on the inflow boundary and ϕ_g on the outer gas boundary. These expressions are integrated using the fourth-order Runge Kutta integration described previously.

Typical calculations employ a grid spacing approximately equal to 20% of the orifice radius, with a time step of 0.005. Run times can be quite substantial (1-2 weeks) due to the fact that the size of the gas/liquid interface increases with time. It is not uncommon to have grids with several hundred nodes in both liquid and gas phases.

Results of sample calculations using the model are presented in Figs. 9 and 10. Figure 9 summarizes a series of runs aimed at investigating the initial behavior of the jet for a variety of density ratios. As ϵ is increased, the momentum required to displace the gas also increases, thereby yielding the "mushroom" shaped jet tips shown in Fig. 9. In Fig. 10, the effect of unsteadiness in gas pressure is investigated. In this case, $We = 17.6$, and $\epsilon = 0.001$ for both simulations presented in Fig. 10. The evolution of a jet under steady back pressure (a) is compared with a simulation in which the orifice pressure drop is varied sinusoidally about the mean (eqn 22) at a frequency of $k = 2$ (b). The unsteady response is not dramatically different than the steady case even under the large amplitude (75%) perturbation in gas pressure. In this case, the orifice channel provides substantial attenuation of the imposed oscillation in the downstream pressure.

Conclusions

A stable, time-accurate, integration scheme has been developed for the coupled, nonlinear dynamics of a free surface in a two-fluid flow. The proceedure is illustrated through a series of axisymmetric and 2-D flow examples involving liquid jets subjected to significant pressure disturbances from a surrounding gas. While the accuracy of the time integration becomes more critical in cases where stagnation points are present on the free surface the technique is shown to work well even in flows where stagnation points are present. As the gas/liquid density ratio approaches unity, the stability and accuracy of the schemes degrade. However, the methods described herein have been applied to physically-meaningful gas/liquid flows which generally exhibit density ratios less than 0.01 even under high pressure conditions.

Acknowledgement

Nomenclature

a = orifice or column radius
G = free space Greens function
k = wave number
$K(p)$ = complete elliptic integral of the first kind
$K_{0,1}$ = modified Bessel functions (eqns 16 and 17)
n = coordinate normal to local surface
P = pressure
q = velocity normal to local boundary
r = radial coordinate (axisymmetric flow)
s = coordinate aligned with local surface
t = time
We = Weber number, $We = \rho_g U^2 a / \sigma$
x = axial coordinate (2-D flow)
y = transverse coordinate (2-D flow)
z = axial coordinate (axisymmetric flow)
α = boundary point singularity contribution
β = surface slope

ϵ = gas/liquid density ratio
Γ = domain boundary
κ = surface curvature
ϕ = velocity potential
ρ = density
σ = surface tension
ω = frequency

Subscript
$(\ )_g$ = gas phase

References

1. Hilbing, J. H., & Heister, S. D. A Boundary Element Method for Atomization of a Finite Liquid Jet, To Appear, *Atomization and Sprays*, 1995.

2. Hung, R. J., and Lee, C. C. Effect of a Baffle on Slosh Waves Excited by Gravity-Gradient Acceleration in Microgravity, *Journal of Spacecraft and Rockets*, 1994, **31**, 1107-14.

3. Class Project, A&AE 630, *Stability of Free Surfaces*, Purdue University School of Aeronautics and Astronautics, Professor Heister, 1994.

4. Foote, G. B. A Numerical Method for Studying Simple Drop Behavior: Simple Oscillation, *Journal of Computational Physics*, 1973, **11**, 507-30.

5. Dold, J. W., and Peregrine, D. H. Steep unsteady water waves, an efficient computational scheme, *Proc. 19th Coastal Engineering Conf., Vol. 1*, Houston, ASCE, 1984, pp. 955-967.

6. Liggett, J. A., and P. L.-F. Liu, *The Boundary Integral Equation Method for Porous Media Flow*, Allen and Unwin, London, 1983.

7. Longuet-Higgins, M. S., and Cokelet, E. D. The deformation of steep surface waves on water. I. A numerical method of computation, *Proc. R. Soc. Lond. A*, 1976, **350**, 1-26.

8. Lundgren, T. S. & Mansour, N. N. Oscillations of Drops in Zero Gravity with Weak Viscous Effects, *Journal of Fluid Mechanics*, 1988, **194**, 479-510.

9. Kelmanson, M. A. Boundary Integral Equation Solution of Viscous Flows with Free Surfaces, *Journal of Engineering Mathematics*, 1983, **17**, 329-43.

10. Tjahjadi, M., Stone, H. A. & Ottino, J. M. Satellite and Subsatellite Formation in Capillary Breakup, *Journal of Fluid Mechanics*, 1992, **243**, 297-317.

11. Newhouse, L. A. and Pozrikidis, C. The Capillary Instability of Annular Layers and Liquid Threads, *Journal of Fluid Mechanics*, 1992, **242**, 193-209.

12. Mansour, N. N. & Lundgren, T. S. Satellite Formation in Capillary Jet Break-Up, *Physics of Fluids A*, 1990, **2**, 1141-44.

13. Nakayama, T., and Washizu, K. The boundary element method applied to the analysis of two-dimensional nonlinear sloshing problems, *Int. J. Numer. Methods. Eng.*, 1982, **17**, 1631-46.

14. Liggett, J. A. Free-surface flow—exposing the hidden nonlinearity, *Commun. Appl. Numer. Methods*, 1988, **4**, 509-16.

15. Medina, D. E., Liggett, J. A., Birchwood, R. A., and Torrance, K. E. A Consistent Boundary Element Method for Free Surface Hydrodynamic Calculations, *International Journal for Numerical Methods in Fluids*, 1991, **12**, 835-57.

16. Spangler, C. A., *Modeling of Jet Atomization in the Wind-Induced Flow Regime*, Masters Thesis, Purdue University, 1994.

17. Rutz, M. W., *Boundary Element Model for the Semi-Infinite Liquid Jet*, Masters Thesis, Purdue University, 1995.

18. Spangler, C. A., Hilbing, J. H., & Heister, S. D. Nonlinear Modeling of Jet Atomization in the Wind-Induced Regime, *Physics of Fluids*, 1995, **7** 964-71.

19. Abramowitz, M. & Stegun, F. A. (eds.), *Handbook of Mathematical Functions*, Dover Publications, 9th Ed., 1970.

20. V. I. Smirnov, *A Course of Higher Mathematics, Volume II*, Pergamon Press, New York, 1964.

21. D. E. Medina, On Droplets and Boundary Elements, Cornell University, FDA-89-12, 1989.

22. Moses, M. P., Collicott, S. H., & Heister, S. D. Visualization of Liquid Jet Breakup and Droplet Formation, 7th International Symposium on Flow Visualization, Seattle, WA, 1995.

23. W. R. Sears, *Small Perturbation Theory*, Princeton University Press, 1960.

24. Sterling, A. M., & Sleicher, C. A. The Instability of Capillary Jets, *Journal of Fluid Mechanics*, 1975, **68**, 477-95.

25. Lefebvre, A. H., *Atomization and Sprays*, Hemisphere Publishing Company, 1989.

26. Heister, S. D., Rutz, M., & Hilbing, J. Effect of Acoustic Perturbations on Liquid Jet Atomization, AIAA 95-2425, 31st AIAA Joint Propulsion Conference, San Diego, CA, 1995.

27. Hoover, D. V., Ryan, H. M., Pal, S., Merkle, C. L., Jacobs, H. R., & Santoro, R. J. Pressure Oscillation Effects on Jet Breakup, *Heat and Mass Transfer in Spray Systems*, HTD-Vol. 187, ASME, 1991, 27-36.
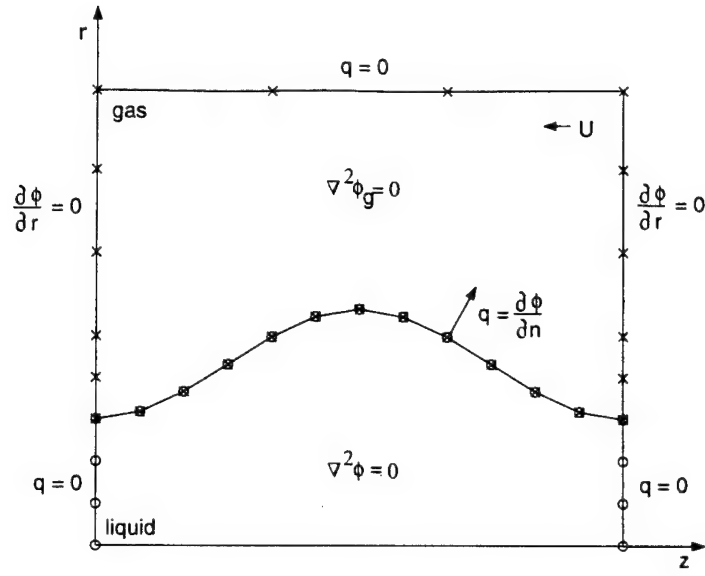
Figure 1. Schematic of Computational Domain for Liquid Jet in Wind-Induced Regime Denoting Boundary Conditions
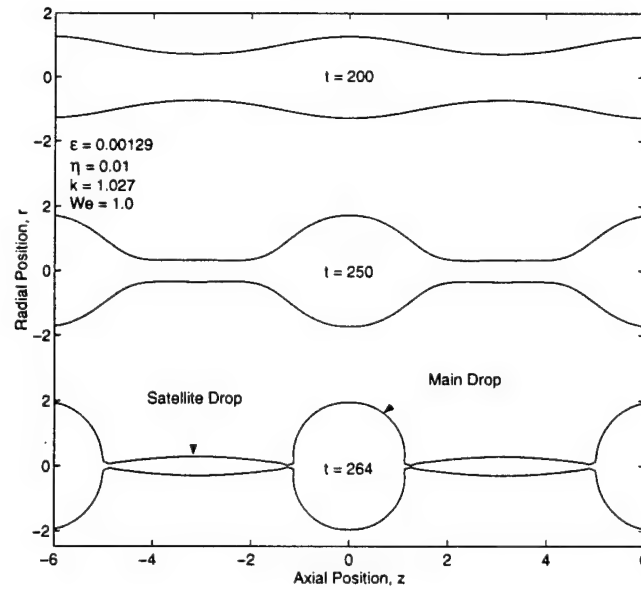
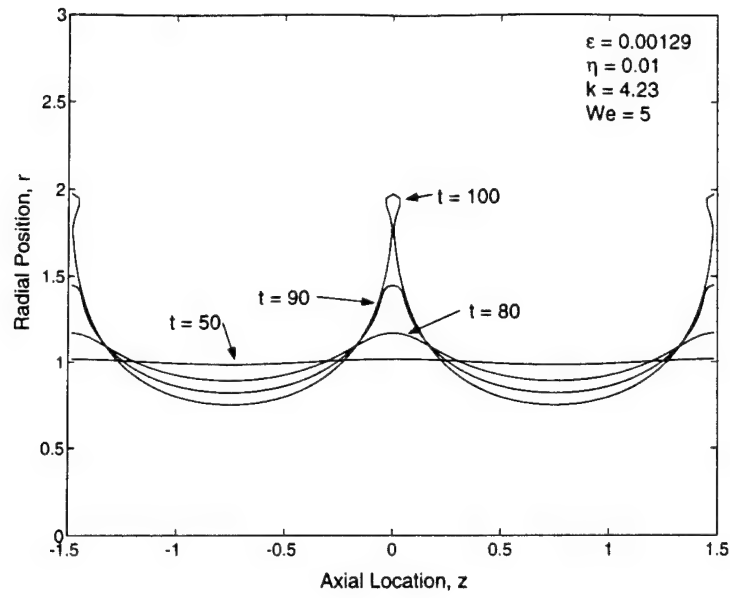Figure 2. Nonlinear Jet Evolution in First Wind-Induced Regime

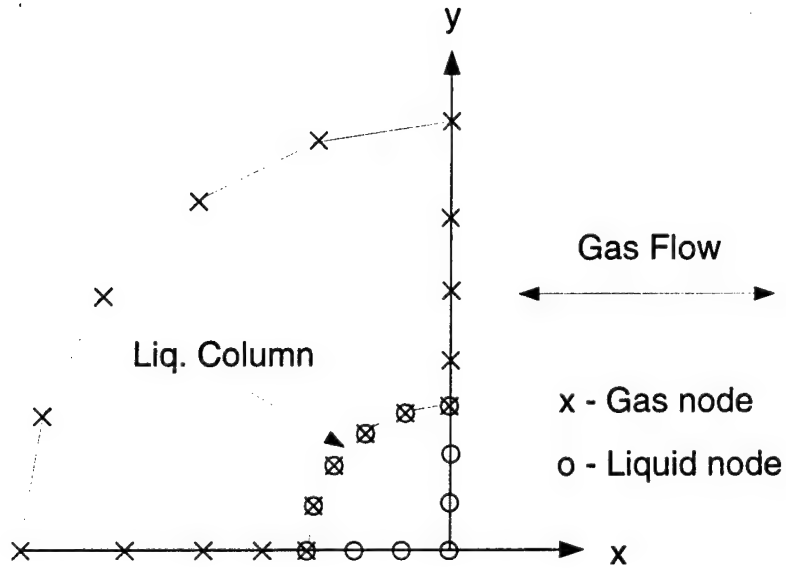Figure 3. Nonlinear Jet Evolution in the Second Wind-Induced Regime

Figure 4. Computational Domain and Boundary Conditions for Liquid Column Subjected to Acoustic Perturbations
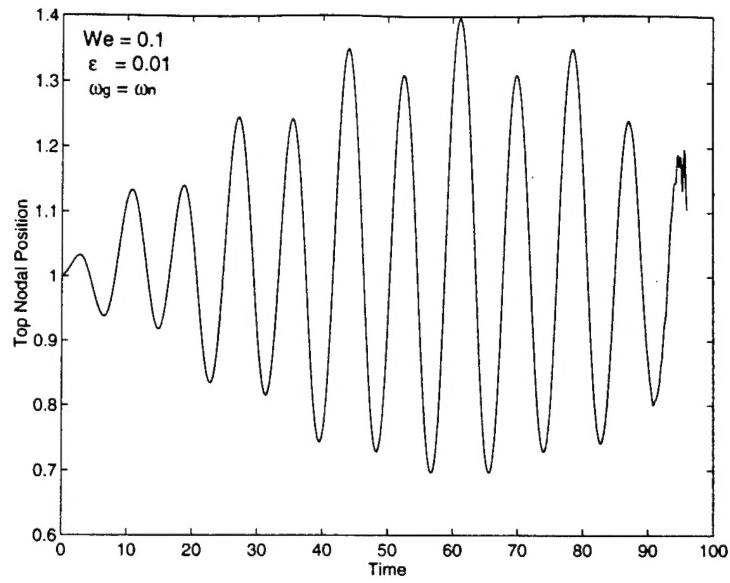
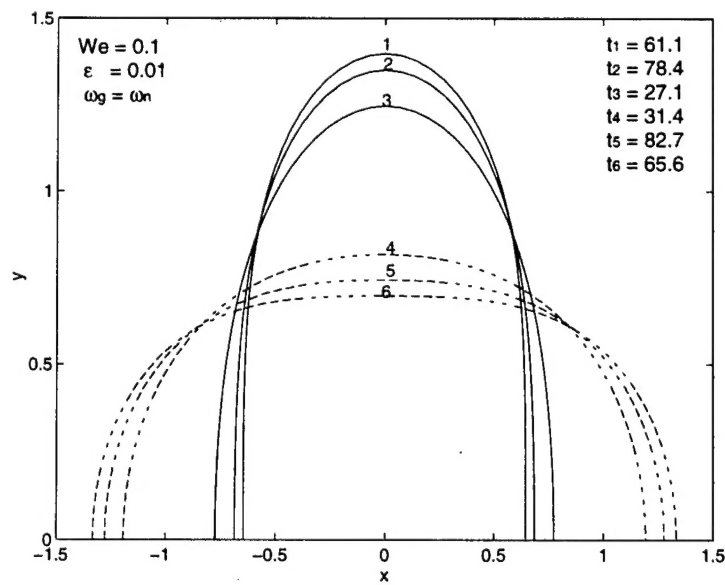Figure 5. Time History for Top Node Position; $We = 0.1$, $\epsilon = 0.01$, $\omega_g = \omega_n$

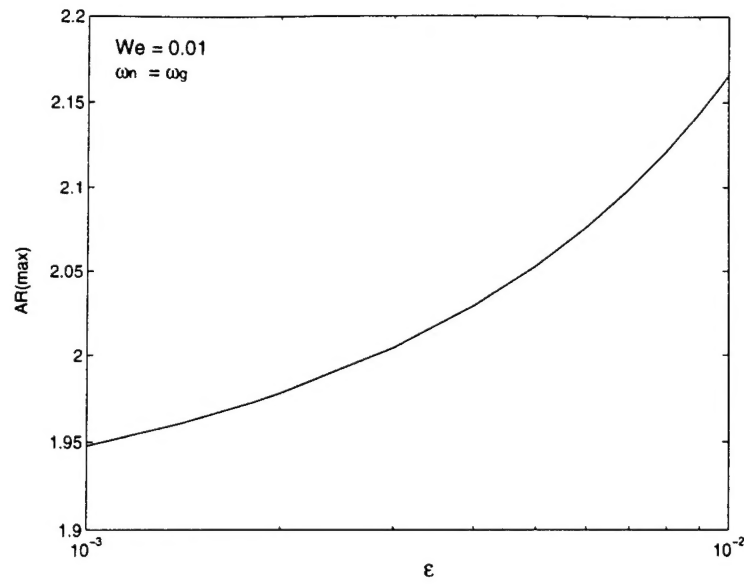Figure 6. Column Shape at Various Times During Excitation Process

Figure 7. Density Ratio Influence on Maximum Aspect Ratio of the Column

Figure 8. Schematic of Computational Domain for Liquid Jet Injected into Quiescent Gas

Figure 9. Effect of Gas Density on Initial Liquid Jet Behavior, $We = 17.6$

Figure 10. Effect of Unsteady Chamber Conditions on Jet Evolution, $We = 17.6$, $\epsilon = 0.001$, (a) - Steady Flow; (b) - 75% Pressure Oscillation About Mean Flow at $k = 2$

Figure 1: Schematic of Computational Domain for Liquid Jet in Wind-Induced Regime Denoting Boundary Conditions

Figure 2: Nonlinear Jet Evolution in First Wind-Induced Regime

Figure 3: Nonlinear Jet Evolution in the Second Wind-Induced Regime

Figure 4: Computational Domain and Boundary Conditions for Liquid Column Subjected to Acoustic Perturbations

92

Figure 5: Time History for Top Node Position; $We = 0.1$, $\epsilon = 0.01$, $\omega_g = \omega_n$

Figure 6: Column Shape at Various Times During Excitation Process

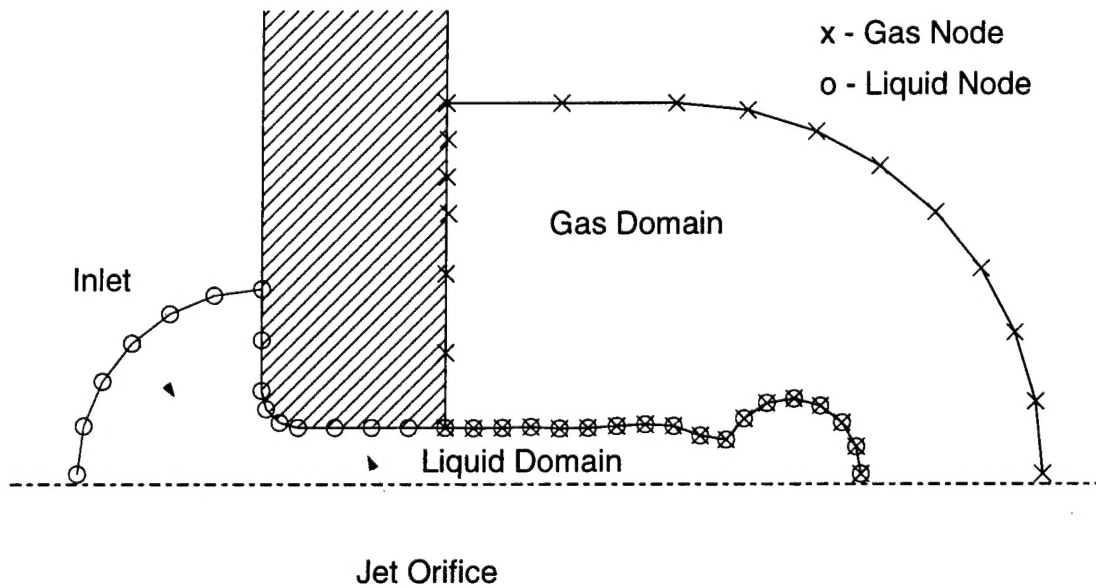Figure 7: Density Ratio Influence on Maximum Aspect Ratio of the Column

Figure 8: Schematic of Computational Domain for Liquid Jet Injected into Quiescent Gas
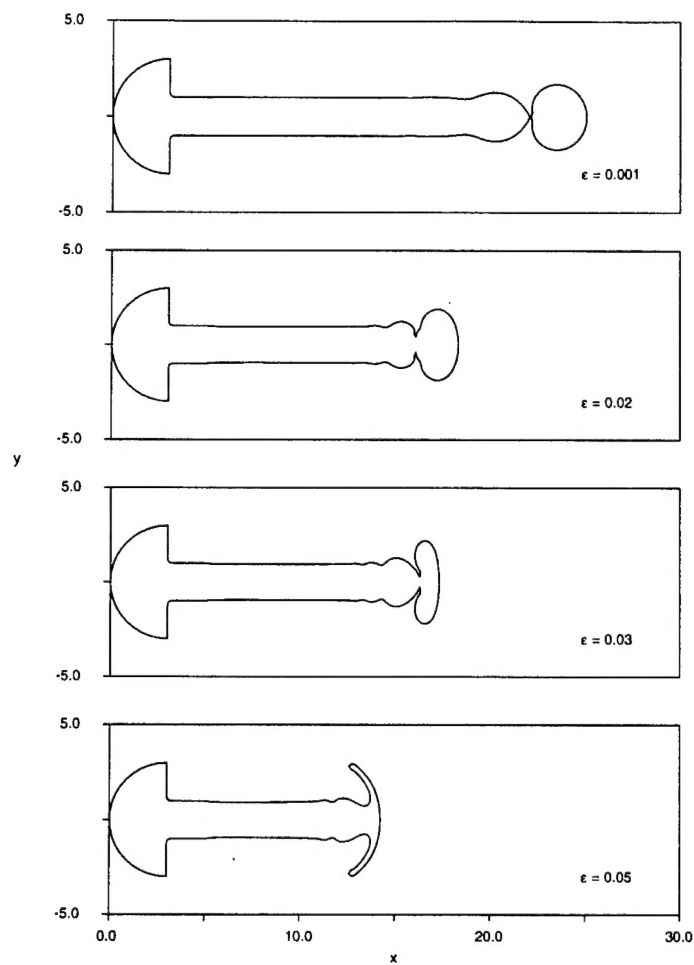
94

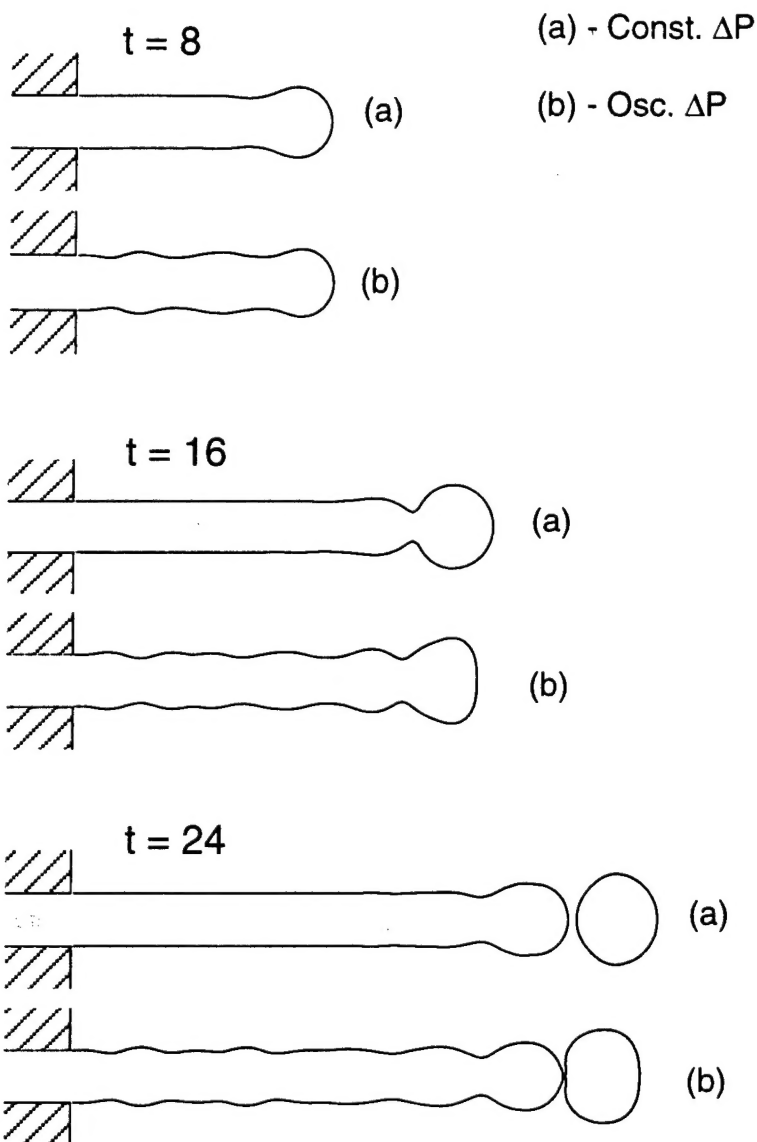Figure 9: Effect of Gas Density on Initial Liquid Jet Behavior, $We = 17.6$

Figure 10: Effect of Unsteady Chamber Conditions on Jet Evolution, $We = 17.6$, (a) - Steady Flow; (b) - 75% Pressure Oscillation About Mean Flow at $k = 2$